Modelling Soil-Residue-Machine Interactions Using the Discrete Element Method (DEM)

By

Peng Wu

A Thesis submitted to the Faculty of Graduate Studies of

The University of Manitoba

in partial fulfilment of the requirements of the degree of

DOCTOR OF PHILOSOPHY

Department of Biosystems Engineering

Price Faculty of Engineering

University of Manitoba

Winnipeg

General Abstract

A comprehensive understanding of the interactions between soil, crop residue, and tillage implements is critical for advancing the efficiency and sustainability of conservation agriculture. This study integrated laboratory and field experiments with discrete element method (DEM) simulations to investigate soil–residue–machine dynamics across two common tillage practices (disc tillage and subsoiling). A concave disc was used in a controlled soil bin experiment to examine the effects of corn residue length and disc operational angles on soil cutting forces and residue incorporation. Experimental findings showed that longer residue lengths increased both draft force and residue incorporation rate, with the developed DEM model predicting these responses with average relative errors of 9.0% for residue incorporation and 18.2% for draft force. Further, a DEM model simulating soil–cornstalk–disc interactions was established and validated, successfully predicting corn stalk cutting effectiveness and soil cutting forces with an overall relative error of 16.4%. Micro-dynamic analysis revealed that soil bulk density and disc type significantly influenced corn stalk sinkage and soil support forces. In addition to residue cutting studies, the effects of soil heterogeneity defined as vertical spatial variation in soil properties, were explored by developing layered DEM soil models. Simulations of subsoiler performance demonstrated that incorporating heterogeneity improved the prediction accuracy for disturbed soil area, while all models showed acceptable accuracy for predicting soil disturbance width. Finally, the dynamics of wheat residue management with a tandem disc harrow were studied, showing that tillage direction, disc angle, travelling speed, and working depth significantly influenced soil surface roughness, draft force, and soil cutting efficiency. Tillage direction perpendicular to the wheat stubble rows produced lower surface residue cover compared to the tillage direction parallel to the wheat stubble rows. Collectively, these studies contribute to a deeper understanding of soil-

residue-machine interactions, offering validated simulation approaches and insights to optimize tillage implement design and operation for enhanced conservation tillage.

Acknowledgements

First and foremost, I would like to express my deepest gratitude to my advisor, Dr. Ying Chen, for her patient guidance, unwavering support, and continuous encouragement throughout my PhD journey. Her insightful advice and constructive comments have been essential in shaping this research and helping me grow as a scholar. Besides, I would also like to express my heartfelt thanks to Dr. Ying Chen and Dr. Sylvio Tessier, for their kindness, warmth, and friendliness. They did not just offer me their support — they made me feel like family, and that is something I will cherish always.

I am also profoundly thankful to the members of my advisory committee, Dr. Zhiwei Zeng, Dr. Danny Mann, and external examiner Dr. Claude Laguë, for their time, expertise, and valuable suggestions that have greatly improved the quality of my work.

Special thanks go to my colleagues and friends (Kobby Acquah, Ernest Owusu-Sekyere, Hao Gong, Zhenyu Tang, Allison Alcock, Hunter Slobodian, Zach Yarechewski, and Hannah Mooney) in the Soil Dynamics and Machinery Laboratory, whose camaraderie, stimulating discussions, and collaborative spirit made this challenging journey more enjoyable and fulfilling. I deeply appreciate your support, both academically and personally. I would like to acknowledge the assistance of the teaching, administrative and technical staff of the Department of Biosystems Engineering, University of Manitoba, especially Minami Maeda and Daniel Benedet.

I would like to acknowledge the financial support from China scholarship Council, Natural Sciences and Engineering Research Council of Canada, and Hainan Province Foreign Experts Program, without which this research would not be completed.

My heartfelt appreciation extends to my family, especially my son (Jiayu Wu) and wife (Yunfang Chen), for their incredible companionship and unwavering support throughout my PhD journey. Their kindness, encouragement, and the sense of belonging they offered made all the difference during the challenging times. Having them by my side felt like a steady source of strength and comfort, helping me stay motivated and focused.

Table of Contents

List of Tables

List of Figures

Nomenclature

$\overline{k_n}$, $\overline{K_n}$	Bond normal stiffness (Pa m^{-1})
$\overline{k_n}$-soil	Soil bond normal stiffness (Pa m^{-1})
$\overline{k_s}$, $\overline{K_s}$	Bond shear stiffness (Pa m^{-1})
$\overline{k_s}$-soil	Soil bond shear stiffness (Pa m^{-1})
A	Elevated soil area (mm^2)
A_h	Soil disturbance area of disc harrow (mm^2)
A_D	Disturbed soil area below original soil surface (mm^2)
ANOVA	Analysis of variance
A_T	Total disturbed soil area (mm^2)
A_U	Undisturbed soil area (mm^2)
c, $c_{\text{-soil}}$	Bond cohesion (Pa)
d	Location of lateral cross-section relative to the shank of subsoiler (mm)
D	Harrow working depth (mm)
d_0	Width of trapezium (mm)
D_0, D_{60}, D_{120}, D_{180}, D_{240}, D_{300}, D_{360}.	Lateral distances of residue tracers relative to disc (mm)
D_1, D_2, D_3, D_4, D_5, D_6, D_7, D_8	Number of discs on the harrow in the model
DEM	Discrete element method
d_p	Particle diameter (mm)
E_p	Modulus of elasticity of particle (Pa)
E_{pb}	Modulus of elasticity of bond (Pa)
F	Soil surface flatness (mm)
F_D	Draft force (N)
F_L	Lateral force (N)

F_t	Total draft of harrow (N)
F_V	Vertical force (N)
HeS, SHeS, HoS	Heterogeneous soil, semi-heterogeneous soil, and homogeneous soil
h_i, h_0, h_n	Height of trapezium for *i*-th, first, and last division points (mm)
I	Force imbalance ratio (%)
k_n, $k_{n\text{-}soil}$	Particle normal stiffness (N m^{-1})
$k_{n\text{-}residue}$	Wheat residue normal stiffness (N m^{-1})
$k_{n\text{-}wall}$	Normal stiffness of soil box (N m^{-1})
k_p	Normal-to-shear stiffness ratio of particle
k_{pb}	Normal-to-shear stiffness ratio of bond
K_{rs}	Stiffness of soil-residue interface (N m^{-1})
k_s, K_s, $k_{s\text{-}soil}$	Particle shear stiffness (N m^{-1})
$k_{s\text{-}residue}$	Wheat residue shear stiffness (N m^{-1})
$k_{s\text{-}wall}$	Shear stiffness of soil box (N m^{-1})
L1, L2, L3, L4, L5, L6, L7	Soil layer with different depth (mm)
L200, L125, L75	200 mm, 125 mm, and 75 mm long of crop residue segments (mm)
L_C	Center-to-center distance of particles (m)
LM	Linear Model
L_s	Share length of subsoiler [mm]
M	Measured values
N	Number of evaluation indicators
N_p	Number of soil particle
Para-Direction	Disc harrow travelling parallel to the standing wheat stubble rows
PBM	Parallel Bond Model
Perp-Direction	Disc harrow travelling perpendicular to the standing wheat stubble rows
PFC^{3D}	Particle Flow Code in Three Dimensions

q	Soil bulkiness (%)
RE	Over relative error (%)
R_I	Residue incorporation rate (%)
S	Simulated values
S_h	Disc spacing of harrow (mm)
T_0, T_1, T_2, T_3, T_4, T_5, T_6, T_7	Numbers of stubble tracers in the model
T_S, T_M	Simulated and measured soil shear torque (N·m)
V	Harrow travelling speed (km h^{-1})
V_p, V_d	Volume of soil domain and volume of single soil particle (m^3)
w	Soil swelling ratio (%)
W	Soil disturbance width (mm)
W_h	Total working width of harrow (mm)
X	Dried weight of the crop residue within a unit surface area (lb $acre^{-1}$)
y	Soil disturbance coefficient (%)
α	Disc tilt angle (°)
α_b	Share rake angle of subsoiler (°)
β	Disc angle or disc gang angle (°)
β_n, β_s	Normal and shear critical damping ratio
γ	Residue cover (%)
η	Soil cutting efficiency (mm^3 J^{-1})
θ	Particle local damping ratio
λ, λ_{-soil}	Bond radius multiplier
μ, μ_{-soil}	Particle friction coefficient
μ_{-wall}	Friction coefficient of soil box
ρ, ρ_p, ρ_{-soil}	Particle density (kg m^{-3})

ρ_b	Soil bulk density (kg m^{-3})
σ, σ_i, σ_{-soil}	Bond tensile strength (Pa)
τ	Bond cohesion strength (Pa)

Chapter 1: General Introduction

1.1. Introduction

Soil tillage has been a cornerstone of agricultural practices for thousands of years, shaping the development of farming and food production. Tillage provides numerous benefits to crop production, such as managing crop residue (Aulakh et al., 2001), aerating soil (Awe et al., 2024), fertilizing soil (Büchi et al., 2018), controlling weeds (Mishra and Singh, 2012), breaking up soil hardpans (Raper et al., 2007), improving soil aggregation (Gupta Choudhury et al., 2014), preparing seedbed (Fanigliulo et al., 2021), regulating soil moisture (Wang et al., 2022), controlling pest and disease (Tamburini et al., 2016), and increasing soil temperature (Liu et al., 2013). Modern agriculture requires sustainable tillage practices to protect soil and environment. Conservation tillage, which has been developed for decades, is such a sustainable tillage practice.

Conservation tillage is a tillage practice that improves soil structure (Madejón et al., 2009), prevents soil erosion (Prasuhn, 2012), maintains the sustainability of crop yields (He et al., 2011), and reduces production cost (Teng et al., 2023). To achieve these benefits, conservation tillage involves minimizing soil disturbance and leaving a significant portion of the previous crop residue (such as stems, leaves, and stalks of plants) on the soil surface. Residue cover on soil surface not only can reduce soil erosion by wind and water, but also increase water infiltration and retention, improve soil organic matter and structure, and suppress weed growth.

However, conservation tillage practices also have drawbacks. For instance, the excessive crop residue results in clogging of seeders, leading uneven seed placement, poor

seed-to-soil contact, and uneven seed germination (Torbert et al., 2007). The excessive crop residue on the soil surface would decompose slowly (Lupwayi et al., 2006), which may negatively impact the seeding quality in more than one year. Conservation tillage can also cause soil surface compaction resulting from reducing soil disturbance and then limits plant growth and productivity (Sidhu and Duiker, 2006). Therefore, tillage operations should effectively incorporate a portion of crop residue into soil, while retaining some crop residue on the soil surface to improve the soil health.

Many types of tillage machines can be used in conservation tillage. Discs have been commonly used to manage crop residue, as they disturb the topsoil adequately, leaving an appropriate crop residue coverage. Meanwhile, subsoiling, another form of conservation tillage, was used to alleviate soil compaction in deeper soil layers without disturbing the surface residue and topsoil (He et al., 2007; Martinez et al., 2012; Deng et al., 2025). Although the interactions between these tillage machines, soil, and crop residues have been studied, the understanding of their dynamics has largely been limited to macro-level phenomena (the forces and displacements of bulk soil and residue). In contrast, the micro-level dynamics, involving the forces and displacements of individual soil and residue particles, remain poorly documented. This study aims to bridge that gap.

Traditionally, the interactions of soil, soil-engaging tools, and crop residue were investigated in laboratory and field experiments (Kushwaha et al., 1986). Later, modelling approach was used for examining the dynamic behaviours of soil and crop residue. Traditional models were developed using analytical methods, such as mathematical considerations (Magalhães et al., 2007), laws of classical mechanics (Ahmadi, 2018), and statistical regression techniques (Upadhyay and Raheman, 2019). These analytical methods

often rely on specific assumptions, which not fully capture the complexities of real-world. In recent years, numerical methods have gained popularity to model complex systems with interactions between multiple variables which are often difficult or impossible to solve analytically. An early numerical method for modelling soil-tool interaction is the finite element analysis (FEA) (Plouffe et al., 1999). A major limitation of FEA is its inability to accurately model materials undergoing large displacements, like the soil and residue movement during tillage operations. A more recent method, the discrete element method (DEM) has been developed by Cundall (1971). DEM considers the discrete nature of material particles (such as soil particles and crop residues) and their interactions with interfacing objects (such as a soil-engaging tool) (Aikins et al., 2023; Wood, 2004). Unlike FEA, DEM has no restrictions on particle displacements.

DEM models have been widely used in modelling soils and their interactions with soil-engaging tools. However, challenges remain in conservation tillage where large amount of crop residues present on the soil surface. Most existing models focus on the macro-dynamic behaviour of soil and often exclude crop residue. Little research has addressed the micro-dynamic behaviours of individual soil particles and crop residue particles. This study aims to provide a comprehensive understanding of the soil-residue-machine interaction at the microscopic level. The findings advance knowledge of soil dynamics, guide the development of high-performance tillage machines, and contribute to improved field efficiency in conservation tillage.

1.2. General Objectives

The general aim of this study was to develop, calibrate, and validate soil-residue-machine interactions using DEM model, and to apply the models to simulate the dynamics of soil and crop residue under varying soil, residue, and machine operational conditions. The specific objectives of this study were to:

- develop a residue-disc-soil interaction model using the DEM (Chapter 3)
- calibrate and validate the residue-disc-soil interaction model using soil bin testing data of residues with various lengths (Chapter 3)
- apply the validated residue-disc-soil interaction model to investigate the effects of tilt and disc angle on residue dynamic attributes (Chapter 3)
- develop a DEM model to simulate soil–cornstalk–disc interactions (Chapter 4)
- conduct experiments for soil–cornstalk–disc interaction model calibration and validation using measured data (Chapter 4)
- investigate the micro-dynamic behaviours of soil and corn stalks under two different concave discs and varying soil bulk densities (Chapter 4)
- develop a DEM model to simulate a disc harrow operated in two tillage directions: parallel and perpendicular to the standing wheat stubble rows (Chapter 5)
- validate the disc harrow model by comparing experimental data with simulated data (Chapter 5)
- simulate the dynamic behaviours of soil and wheat residue under different operational parameters of the harrow (Chapter 5)

- develop and calibrate a soil-subsoiler interaction model with a layered structure to mimic the soil heterogeneity along the depth profile (Chapter 6)
- use the model to investigate the micro-behaviours resulting from the subsoiling (Chapter 6)
- compare models with varying degrees of soil heterogeneity in the resultant soil disturbance characteristics (Chapter 6)

1.3. Thesis Structure

This thesis is structured in a collection of paper format (grouped manuscript style). It includes a general abstract, followed by a general introduction and general literature review in Chapters 1 and 2 respectively. Chapters 3 to 6 present four individual papers, each with its own abstract, introduction, methodology, results and discussions, conclusions, and references sections. These chapters involved four research topics, including crop residue incorporation (Chapter 3), crop residue cutting (Chapter 4), disc harrow tillage (Chapter 5), and subsoiling in layered soil structures (Chapter 6). They focused on tillage, soil and residue, from top soil in shallow tillage to subsoil in deep tillage. Chapter 7 provides a general conclusion and recommendations.

The four main chapters (Chapters 3 to 6) focused on distinct aspects of soil–residue–machine interactions. The central theme was to apply the Discrete Element Method (DEM) for modeling dynamic behaviours of soil and crop residue under various tillage conditions. The investigation by quantifying the effects of disc angle and tilt angle on residue incorporation was initiated in Chapter 3. The micro-scale interaction mechanisms between discs, soil particles, and corn stalks were revealed in Chapter 4. Chapter 5 advanced this

understanding by introducing tillage direction relative to crop stubble rows as a field-relevant variable influencing overall residue displacements. The studies of disc-soil-residue interaction were expanded from a single disc in Chapters 3 and 4 to multiple-disc implement in Chapter 5. Finally, the attention was shifted from surface soil (shallow discing) to deep soil (subsoiling), extending the DEM to analyze disturbance of deeper soil under layered soil conditions. In conclusion, this thesis formed a cohesive progression, from surface-level of surface to subsurface soil disturbance, both of which dealing with crop residue incorporations. This offers an integrated perspective to support tillage systems for soil and residue management.

Chapter 3 has been published as Wu and Chen (2024) in *Computer and Electronics in Agriculture*. Chapter 4 has also been published as Wu et al. (2025) in *Smart Agricultural Technology*. Chapter 5 was submitted to *Biosystems Engineering* for publication (status: under review). Chapter 6 was published in *Smart Agricultural Technology* as Wu et al. (2024). In these publications and manuscripts, the candidate is the first author, and his contributions include, not limited to, conceptualization, methodology, software, validation, formal analysis, investigation, data curation, visualization, and paper writing. The other coauthors' contributions include conceptualization, methodology, resources, review and editing, supervision, project administration, and funding acquisition.

1.4. References

Ahmadi, I., 2018. A draught force estimator for disc harrow using the laws of classical soil mechanics. Biosystems Engineering, 171, 52–62. https://doi.org/10.1016/j.biosystemseng.2018.04.008

Aikins, K. A., Ucgul, M., Barr, J. B., Awuah, E., Antille, D. L., Jensen, T. A., and Desbiolles, J. M. A., 2023. Review of discrete element method simulations of soil tillage and furrow opening. Agriculture (Switzerland), 13(3), e0541. https://doi.org/10.3390/agriculture13030541

Aulakh, M. S., Khera, T. S., Doran, J. W., and Bronson, K. F., 2001. Managing Crop Residue with Green Manure, Urea, and Tillage in a Rice–Wheat Rotation. Soil Science Society of America Journal, 65(3), 820–827. https://doi.org/10.2136/sssaj2001.653820x

Awe, G. O., Fontanela, E., and Reichert, J. M., 2024. Degree of compaction, aeration, and soil water retention indices of a sugarcane field without soil disturbance after initial tillage. Canadian Journal of Soil Science, 104(1), 91–107. https://doi.org/10.1139/cjss-2022-0066

Büchi, L., Wendling, M., Amossé, C., Necpalova, M., and Charles, R., 2018. Importance of cover crops in alleviating negative effects of reduced soil tillage and promoting soil fertility in a winter wheat cropping system. Agriculture, Ecosystems and Environment, 256, 92–104. https://doi.org/10.1016/j.agee.2018.01.005

Cundall, P. A., 1971. A computer model for simulating progressive, large-scale movements in blocky rock systems. Proceedings of symposium of International Society of Rock Mechanics. 2 (8).

Deng, Y., Zhang, W., Qi, B., Wang, Y., Ding, Y., and Zhang, H., 2025. Research progress and prospects of intelligent measurement and control technology for tillage depth

in subsoiling operations. Sensors (Switzerland), 25(12), e3821. https://doi.org/10.3390/s25123821

Fanigliulo, R., Pochi, D., and Servadio, P., 2021. Conventional and conservation seedbed preparation systems for wheat planting in silty-clay soil. Sustainability (Switzerland), 13(11), e6506. https://doi.org/10.3390/su13116506

Gupta Choudhury, S., Srivastava, S., Singh, R., Chaudhari, S. K., Sharma, D. K., Singh, S. K., and Sarkar, D., 2014. Tillage and residue management effects on soil aggregation, organic carbon dynamics and yield attribute in rice-wheat cropping system under reclaimed sodic soil. Soil and Tillage Research, 136, 76–83. https://doi.org/10.1016/j.still.2013.10.001

He, J., Li, H., Rasaily, R. G., Wang, Q., Cai, G., Su, Y., Qiao, X., and Liu, L., 2011. Soil properties and crop yields after 11 years of no tillage farming in wheat-maize cropping system in North China Plain. Soil and Tillage Research, 113(1), 48–54. https://doi.org/10.1016/j.still.2011.01.005

He, J., Li, H., Xiaoyan, W., McHugh, A. D., Wenying, L., Huanwen, G., and Kuhn, N. J., 2007. The adoption of annual subsoiling as conservation tillage in dryland maize and wheat cultivation in northern China. Soil and Tillage Research, 94(2), 493–502. https://doi.org/10.1016/j.still.2006.10.005

Krushwaha, R. L., Vaishnav, A. S., and Zoerb, G. C., 1986. Soil bin evaluation of disc coulters under no-till crop residue conditions. Transactions of the ASAE, 29(1), 40–44. https://doi.org/10.13031/2013.30098

Liu, S., Yang, J. Y., Zhang, X. Y., Drury, C. F., Reynolds, W. D., and Hoogenboom, G., 2013. Modelling crop yield, soil water content and soil temperature for a soybean-maize rotation under conventional and conservation tillage systems in Northeast China. Agricultural Water Management, 123, 32–44. https://doi.org/10.1016/j.agwat.2013.03.001

Lupwayi, N. Z., Clayton, G. W., O'donovan, J. T., Harker, K. N., Turkington, T. K., and Soon, Y. K., 2006. Potassium release during decomposition of crop residues under conventional and zero tillage. Canadian Journal of Soil Science, 86(3), 473–481. https://doi.org/10.4141/S05-049

Madejón, E., Murillo, J. M., Moreno, F., López, M. V., Arrue, J. L., Alvaro-Fuentes, J., and Cantero, C., 2009. Effect of long-term conservation tillage on soil biochemical properties in Mediterranean Spanish areas. Soil and Tillage Research, 105(1), 55–62. https://doi.org/10.1016/j.still.2009.05.007

Magalhães, P. S. G., Bianchini, A., and Braunbeck, O. A., 2007. Simulated and experimental analyses of a toothed rolling coulter for cutting crop residues. Biosystems Engineering, 96(2), 193–200. https://doi.org/10.1016/j.biosystemseng.2006.10.014

Martinez, I. G., Prat, C., Ovalle, C., del Pozo, A., Stolpe, N., and Zagal, E., 2012. Subsoiling improves conservation tillage in cereal production of severely degraded Alfisols under Mediterranean climate. Geoderma, 189–190, 10–17. https://doi.org/10.1016/j.geoderma.2012.03.025

Mishra, J. S., and Singh, V. P., 2012. Tillage and weed control effects on productivity of a dry seeded rice-wheat system on a Vertisol in Central India. Soil and Tillage Research, 123, 11–20. https://doi.org/10.1016/j.still.2012.02.003

Plouffe, C., Lague, C., Tessier, S., Richard, M., and McLaughlin, N., 1999. Moldboard plow performance in a clay soil: simulation and experiment. Transactions of the ASAE, 42(6), 1531–1539. https://doi.org/10.13031/2013.13317

Prasuhn, V., 2012. On-farm effects of tillage and crops on soil erosion measured over 10 years in Switzerland. Soil and Tillage Research, 120, 137–146. https://doi.org/10.1016/j.still.2012.01.002

Raper, R. L., Reeves, D. W., Shaw, J. N., van Santen, E., and Mask, P. L., 2007. Benefits of site-specific subsoiling for cotton production in Coastal Plain soils. Soil and Tillage Research, 96(1–2), 174–181. https://doi.org/10.1016/j.still.2007.05.004

Sidhu, D., and Duiker, S. W., 2006. Soil compaction in conservation tillage: Crop impacts. Agronomy Journal, 98(5), 1257–1264. https://doi.org/10.2134/agronj2006.0070

Tamburini, G., De Simone, S., Sigura, M., Boscutti, F., and Marini, L., 2016. Conservation tillage mitigates the negative effect of landscape simplification on biological control. Journal of Applied Ecology, 53(1), 233–241. https://doi.org/10.1111/1365-2664.12544

Teng, C., Lyu, K., Zhu, M., and Zhang, C., 2023. Impact of conservation tillage technology application on farmers' technical efficiency: Evidence from China.

Agriculture (Switzerland), 13(6), e1147. https://doi.org/10.3390/agriculture13061147

Torbert, H. A., Ingram, J. T., and Prior, S. A., 2007. Planter aid for heavy residue conservation tillage systems. Agronomy Journal, 99(2), 478–480. https://doi.org/10.2134/agronj2006.0114

Upadhyay, G., and Raheman, H., 2019. Specific draft estimation model for offset disc harrows. Soil and Tillage Research, 191, 75–84. https://doi.org/10.1016/j.still.2019.03.021

Wang, Z., Sun, J., Du, Y., and Niu, W., 2022. Conservation tillage improves the yield of summer maize by regulating soil water, photosynthesis and inferior kernel grain filling on the semiarid Loess Plateau, China. Journal of the Science of Food and Agriculture, 102(6), 2330–2341. https://doi.org/10.1002/jsfa.11571

Wood, D., 2004. Geotechnical modelling (1st ed.). Spon Press. https://doi.org/10.1201/9781315273556

Wu, P., and Chen, Y., 2024. Discrete element modelling of the effect of disc angle and tilt angle on residue incorporation resulting from a concave disc. Computers and Electronics in Agriculture, 224, e109222. https://doi.org/10.1016/j.compag.2024.109222

Wu, P., Zhang, X., and Chen, Y., 2025. Simulation of the micro-dynamics in soil–cornstalk–disc interactions using the discrete element method. Smart Agricultural Technology, 11, e100984. https://doi.org/10.1016/j.atech.2025.100984

Wu, P., Zhang, X., Zeng, Z., and Chen, Y., 2024. DEM simulation of subsoiling for soil disturbance as affected by soil layering and working speed. Smart Agricultural Technology, 7, e100385. https://doi.org/10.1016/j.atech.2023.100385

Chapter 2: General Literature Review

2.1. Tillage Implements

Tillage is a fundamental agronomic operation aimed at preparing the soil for planting (Baker et al., 1996), controlling weeds (Wiese, 1985), incorporating residues (Al-Kaisi and Guzman, 2013), and improving soil structure for optimal crop growth (Li et al., 2024). Broadly, tillage can be classified into primary and secondary tillage (Tiessen et al., 2007). Primary tillage is the first soil operation after harvest and involves deeper and more aggressive soil disturbance. Secondary tillage is lighter, focused on refining the seedbed and conserving soil moisture. The choice of tillage implements depends on the desired soil condition, crop requirements, and environmental considerations.

Modern tillage equipment is designed to balance soil loosening, mixing, and residue management while minimizing energy consumption and environmental degradation. Among the wide range of tillage tools, disc implements and subsoilers represent two distinct approaches. Discs are used for surface-level operations such as residue mixing and weed control (Chen et al., 2004), while subsoilers are used for deep tillage to break compacted layers and improve root penetration (Shahgoli et al., 2010).

2.1.1 Disc Tillage

Disc are rotary tools designed to be mounted on a frame (Figure 2.1) and are primarily used to cut soil and crop residue and incorporate residue into the soil. There are several types of discs implements for specific tillage needs. Disc plows are used for primary tillage to break clods and mix surface residues (Al-Janobi, 1998). Disc harrows are for secondary tillage. Disc harrows have different disc configurations. For instance, offset disc harrows

are ideal for uneven terrains, offering improved residue handling and deeper penetration (Upadhyay and Raheman, 2018), whereas tandem disc harrows feature both front and rear gangs for enhanced soil pulverization and surface levelling (Adam and Erbach, 1992).

Figure 2.1. Example of disc equipment that managing soil and crop residue (designed and manufactured by Versatile).

2.1.2 Subsoiling

Subsoilers are deep tillage implements designed to alleviate soil compaction by breaking up hardpan layers without significantly disturbing the topsoil structure (Hipps and Hodgson, 1987). Various types of subsoilers are used based on tillage requirements and soil conditions, which influence the width of disturbed soil and the required draft force. For example, straight shank subsoilers, such as rippers (Figure 2.2) offered minimal soil disturbance while effectively penetrating compacted layers (Duiker, 2020). Curved shank subsoilers were designed to fracture the soil, creating a broader disruption zone (Tong et al., 2020). Winged subsoilers, equipped with lateral extensions, enhance soil shattering at the same working depth, increasing tillage efficiency (Hang et al., 2017a). Subsoiling is

highly energy-intensive, with high draft forces, necessitating to optimize performance and reduce fuel consumption. `

Figure 2.1. A subsoiler with wavy coulters and rippers.

2.2. Residue Incorporation into Soil

2.2.1 Crop Residue in Conservation Tillage

In conservation tillage, tillage tools must deal with crop residues, which make the soil-tool interaction more complex. Inadequate residue management can lead to significant clogging of tillage and seeding equipment. The approaches for appropriate residue management through tillage are discussed below.

Residue cover, related to the quantity of crop residue per unit surface area, was calculated by the following equation (Karayel et al., 2024):

$$\gamma = (1 - e^{-0.000644X}) \times 100 \qquad (2.1)$$

where γ = residue cover (%), X = dried weight of the crop residue within a unit surface area (lb acre^{-1}). The percentage of residue cover (40%, 55%, 80%, and 90%) for conservation tillage had effects on seeding quality (Karayel et al., 2024). Experimental results demonstrated that a high residue cover reduced seeding depth of double-disc furrow

openers and seed germination rates, while delaying the plant emergence time. A proper density of crop residue on the soil surface could reduce diurnal fluctuations in soil temperature between day and night periods, which thus favoured the crop emergence and growth (Morris et al., 2009). Therefore, the surface cover of crop residue should be adjusted to an appropriate level for optimizing seeding depth, plant emergence speed, and crop establishment. Incorporating crop residue into the soil with tillage helps to mitigate the challenges associated with excessive crop residue. Tillage operations also have positive effects on soil conditions, such as aeration, ultimately resulting in an increase in crop yield.

Residue incorporation is affected by many factors, including tillage operational parameters and residue and soil conditions in fields. Field experiments showed that tillage depth and residue incorporation affect the soil properties and crop yield (Tian et al., 2020). Amounts and sizes of crop residue also affect residue incorporation, movement, and decomposition in soil. Liu et al. (2010) have investigated the effect of oat straw length ranging from 50 to 250 mm on tillage performance of a sweep. The forward displacement of oat straw increased by 20% when straw length increased from 50 to 250 mm. Long straws were less buried into soil by the sweep compared to short straws. Oat straws decayed faster when tilled into the soil than if left undisturbed (Vigil, 1995). Using tillage equipment, such as discs, crop residues can be cut into smaller pieces, which can speed up the residue decomposition.

In addition to residue incorporation, residue hairpinning is another problem associated with crop residue management. Hairpinning refers to a condition where crop residue (such as straw or stalks) is pushed into the seed furrow by seed openers (often disc openers), rather than being cleanly cut or moved aside (Chen et al., 2016). Instead of allowing seeds

to be placed directly into the soil, the opener bends and presses the residue into the furrow, forming a *"hairpin"* shape, and thus, the seed ends up sitting on top of or surrounded by residue rather than making firm contact with the soil. Hairpinned residue causes poor soil-seed contact, inconsistent seeding depth, and compromised moisture and nutrient access by the seedling. Hairpinning could be alleviated via operating tillage tools with appropriate working depths and cutting angles (Zeng et al., 2021), reducing the residue coverage to a balanced level (Torbert et al., 2007), and chopping crop residue into smaller size (Aikins et al., 2020).

2.2.2 Interactions of Soil and Soil-Engaging Tools

Understanding the dynamics between soil and soil-engaging tools is crucial for optimizing agricultural practices, improving tillage efficiency, and enhancing soil sustainability. Soil cutting force and soil disturbance are important dynamic attributes in tillage. Previous studies examined the soil cutting force of mouldboard plows (Makange et al., 2020; Ucgul and Saunders, 2020). The tool geometries were found to have significant influence on the soil cutting forces (Hoseinian et al., 2022). The influence of operational parameters, such as working speed and working depth, also influenced soil cutting forces (Onwualu and Watts, 1998) and soil disturbance characteristics (Zhao et al., 2020) of soil-engaging tools. In the design of soil-engaging tools, adequately considering the soil cutting forces and soil disturbance mechanisms (Tan et al., 2025) is crucial for improving working performance of the tools. In agricultural fields, stones present significant challenges during soil preparation, as they damage equipment and hinder efficient tillage. The soil-tool interactions of a seedbed clearing and shaping device was studied for efficiently removing stones from the seedbed and forming seeding furrows, resulting in a high-quality seedbed

(Li et al., 2022). In practice, compacting devices are sometimes used to prepare a uniform soil seedbed. Understanding the interaction of soil and a compacting device helps to improve the seedbed uniformity (Zhang et al., 2024a).

2.2.3 The Effect of Residue

Existence of crop residue can complicate achieving the desired depth and uniformity, resulting from increasing resistance to tool penetration and causing uneven interaction of tool with the soil. To address this, a toothed rolling coulter was developed to enhance the penetration ability to the soil with corn residue cover (Magalhães et al., 2007). Laboratory experiments comparing toothed coulters with notched and smooth coulters further confirmed that crop residue significantly affects the ability of penetration (Bianchini and Magalhães, 2008). The penetration depth of a disc coulter is different as the type of crop residue changes. For example, compared to fields with wheat and rice residues, the disc coulters penetrated deeper in fields with corn residue (Kumar et al., 2021).

2.3. Modelling Approaches

Agricultural soils are complex systems with a heterogeneous mixture of solid (sand, silt, clay, and organic matter), liquid (moisture), and gaseous components (oxygen, carbon dioxide, and other gases). This multiphase nature of soil creates significant challenges to modelling of soil. For instance, changes in moisture content affect soil mechanical properties (compaction and strength) (Zheng et al., 2021). Moreover, the soil structure (porosity and aggregation) might be different under tillage practice and weather (Boizard et al., 2013). As a result, accurately modelling the behaviours of soils under various agricultural conditions should consider the movement nonlinearity, spatial variability, and

coupled processes from different perspectives. This complexity makes soil modelling both scientifically challenging and computationally demanding, often simultaneously requiring model accuracy and practical feasibility.

Modelling approaches are effective for studying tillage dynamics by offering insights into how different variables interact, guiding machinery design, soil management, and residue management. There have been numerous studies in tillage research utilizing various modelling approaches, including empirical, analytical, and numerical methods.

2.3.1 Empirical and Analytical Models

Empirical models are based on observed data and make predictions without requiring an in-depth understanding of the underlying complex processes. For example, field data of soil penetrometer resistance and soil conditions (e.g. bulk density and water content) were collected for developing an empirical model that predicted soil penetrometer resistance at different soil conditions (Wang et al., 2021). An empirical model was developed for predicting the increase in bulk density of topsoil as the soil was deformed under the traffic compaction (Schjønning, 2023).

Analytical models help streamline soil tillage research by providing a controlled, cost-effective and predictive framework for studying the effects of different tillage practices (Liu et al., 2021). Early analytical models were represented by the Universal Earth Moving Equations for simple soil-engaging tools, such as blades (McKyes, 1985). Later, analytical models were developed for soil-engaging tools with more complex geometries. Using analytical models, soil cutting forces were typically predicted for different soil-engaging

tools, such as convex-type wide cutting blade (Gupta et al., 1989), sweeps (Liu et al., 2010), and curved subsoiler (Jiang et al., 2020).

However, analytical models have several limitations. Analytical models often require simplifying assumptions. For example, in the Universal Earth Moving Equations, soil failure was assumed to be passive, and the failure line is fixed within a soil body (McKyes, 1985). This assumption works only for problems with simple shapes (e.g. a blade soil-engaging tool) and well-defined boundary conditions (e.g. flat soil surface). Complex geometries or loading scenarios are difficult to solve analytically. Also, analytical solutions are not easily adaptable to changes in soil properties, boundary conditions, or system configurations. Soil is non-homogeneous with nonlinear behaviour (such as large deformations and frictional contact) and is very difficult to handle analytically. Soil-residue-machine systems involving discrete particles (like soil particles and crop residue particles) are typically beyond the reach of analytical models.

2.3.2 Numerical Models

Numerical models offer several advantages over analytical models, particularly when dealing with complex and real-world problems. Unlike analytical models, which often require simplifying assumptions and are limited to simple geometries and linear behaviour, numerical models can handle complex shapes, heterogeneous soil, and nonlinear dynamics with high precision. They are especially useful for simulating large deformations, time-dependent phenomena, and interactions between discrete elements, such as soil particles or crop residues. Common numerical approaches are the finite element analysis (FEA) and discrete element method (DEM). Both methods provide flexibility to model a wide range of physical conditions and boundary scenarios that would be impractical or impossible to

solve analytically. As a result, numerical methods are more powerful tools for gaining deeper insights into dynamic systems, such as soil-residue-machine interaction systems.

2.3.2.1 Finite Element Models

In modelling soil-tool interactions using the FEA, soil is treated as a continuous medium. Soil body is divided into smaller elements that are connected at specific points (nodes). Soil is typically assumed as elastic-plastic material. To simulate the mechanical behaviours of soil, different model descriptions were applied in the literatures. An arbitrary Lagrangian-Eulerian description was introduced to solve soil deformations resulting from the cutting action of soil-engaging tools (Zhang et al., 2018). The Drucker-Prager constitutive law was also adopted with the flow properties of soil, therefore being applied in the finite element simulations (Armin et al., 2014; Mouazen and Neményi, 1999). The working performance of the tool was evaluated using the model by simulating soil deformation and draft forces for various tools, such as mouldboard plow (Bentaher et al., 2013), disc plow (Abu-Hamdeh and Reeder, 2003), and simple blades (Abo-Elnor et al., 2004; Armin et al., 2014).

In reality, soil consists of discrete particles. The discrete nature is difficult to be captured by a finite element model. Especially in loose and non-cohesive soils, such as sandy loam soil, the granular interactions between individual soil particles are not naturally accounted by the FEA. A finer meshing (to capture the soil-tool interaction in sufficient detail) is required in the finite element model for simulating the localized soil heterogeneity (Mouazen and Neményi, 1999), resulting in computational challenge. In addition, the contact forces, sliding, rolling, and rotation between soil particles are important for soil tillage research, but cannot be fully captured in a finite element model. Thus, the FEA

excels for studying macroscopic dynamic behaviours of continuum (soil), rather than evaluating the microscopic dynamic behaviours of discrete soil particles.

2.3.2.2 Discrete Element Models

Discrete Element Method (DEM), a numerical simulation technique (Cundall, 1971), has been widely used for modelling the behaviours of discrete particles, such as soil and crop residue. Newton's laws of motion and mathematical relation of force-displacement are the principles followed by particle movement and interaction. A DEM model simulates how particles move, collide, and displace in response to external loads or forces. Under an applied external load, particle behaviours in the simulation are monitored, including displacement, contact force, and velocity. The DEM allows for the consideration of different particles, such as soil particles and crop residue particles. The method allows for easily monitoring the forces and displacements of individual soil and residue particles. Thus, the DEM was used for modelling soil-residue-machine interactions in this study.

DEM has been successfully applied to soil mechanics and dynamics, enabling researchers to simulate soil behaviours under various environments. Existing studies have explored how DEM can model soil deformation and soil failure under the action of soil-engaging tools, including soil compaction (Acquah and Chen, 2021), shear (Liu et al., 2023), and flow properties (Qi et al., 2019). DEM allows for simulating the characterization of soil particles and their responses to external forces, which is crucial for understanding how soil-engaging tools interact with soil in tillage operations.

Soil body can be modelled as a dis-continuum in DEM. The model provides detailed dynamic attributes of individual particles as they interact with machines. These attributes

include the non-linear behaviours of soil, such as plastic deformation (Cheng et al., 2004), irregular soil stress-strain curves (De Pue et al., 2019; Zhang et al., 2019), and heterogeneous properties of field soils (Zeng et al., 2017). Such microscopic-level behaviours may not be captured by continuum-based methods like FEA.

Two commonly used DEM commercial software are EDEM (Altair Engineering Inc., USA) and Particle Flow Codes in Three-Dimensions (PFC^{3D}) (Itasca Consulting Group, Inc., USA). The basic elements of DEM are spherical particles. For simplicities, spheres are commonly used to replicate agricultural soil particles in DEM. The forces on normal and tangential direction between two particles were generated in accordance with different particle contact models (Liu, 2021). In PFC^{3D}, the common contact models for mimicking soil particle contact are parallel bond contact model, linear cohesion model, Hertz-Mindin with bonding model. The hysteretic spring contact model in software EDEM has also been used in soil tillage research. Different soil textures and conditions were modelled with different particle contact models, but the standards regarding which contact models fit which soil textures have not been established. The contact model for sandy loam soil was represented by the linear cohesion model (Ucgul et al., 2018a), hysteretic spring contact model (Barr et al., 2018), and parallel bond contact model (Li et al., 2016). Hertz-Mindin with bonding model was used for mimicking loamy soil (Wang et al., 2019a). The properties of agricultural sandy soil were mimicked by the parallel bond contact model (Tamás et al., 2013). These suggest that soil condition (such as cohesion and friction), rather than soil texture, is a dominant factor in determining which particle contact model to be used.

DEM has been widely used to study the soil behaviours as influenced by soil-engaging tools (disc plows, subsoilers, sweeps, mouldboard plows, and rotary tiller blades). Results help optimize tool design, reduce energy consumption, and improve the performance of tillage operations. For instance, the traditional rotary tiller was designed and tested in the discrete element models (Du et al., 2022; Ucgul et al., 2018b; Zhang et al., 2022b). The soil-subsoiler interactions were modelled for analysing the soil behaviours (Hang et al., 2017b; Wang et al., 2019b), optimizing the structural parameters (Wang et al., 2019a; Wang et al., 2020; Zhang et al., 2022a), and reducing tillage resistance (Li et al., 2014; Sun et al., 2018). DEM models were developed to study the soil dynamic behaviours resulting from sweeps (Nagy et al., 2024; Tamás, 2018; Tamás et al., 2013). Tillage force of mouldboard plows was also predicted in several DEM models, for improving its working performance (Makange et al., 2020; Saunders et al., 2021; Ucgul et al., 2017). A new disc furrow opener was biomimetically designed and tested with the help of a DEM model (Wang et al., 2019c). Also, soil displacements and soil cutting forces of the disc plow were monitored using DEM models (Murray and Chen, 2018; Sadek et al., 2021).

Additionally, the characteristics of soil itself were studied using a DEM model. This method is valuable for predicting how soil behaves under shear stresses, such as in shear box tests, plate sinkage tests, and confined compression tests, where it helps understand soil friction, shear strength, and yield behaviour (Bahrami et al., 2020; 2022; Ucgul et al., 2015). The interaction and displacement of soil particles under load pressure were revealed using DEM models (Acquah and Chen, 2021; 2023).

2.4. DEM Modelling and Simulation

Crop residue is a critical factor that influenced the DEM modelling for conservation tillage systems. The presence of crop residue can alter dynamics of soil-tool interaction by exerting additional impact to soil and soil-engaging tools. Therefore, including crop residue in DEM models is essential for model accuracies.

2.4.1 Applications of Soil-Residue-Machine Interaction Models

Crop residue has been considered as an essential component in a DEM model that optimizes the structural and operational parameters of tillage tools. Considering the performance in crop stubble cutting and clearing, a disc was optimized and analysed using a DEM model (Li et al., 2025). The structural and operational parameters of a potato stubble pulling device were optimized in a DEM model developed by Wang et al. (2025). A DEM model of maize stubble was developed for investigating the interaction between a tool and maize stubbles to optimize the tool design (Liu et al., 2024). Optimal tilt angles and disc angles for different disc coulters were determined using a DEM model for improving residue managing efficiency (Zhang et al., 2024b). A DEM model with three blades interacted with soil and maize residue was developed to simulate the residue-cutting efficiency (Zhang et al., 2025).

DEM models were also used to analyse the mechanism of crop residue mixing with soil. The parameters of the soil-residue interference were determined and recommended for future research (Xie et al., 2024). Residue movements were simulated in DEM models for understanding dynamic behaviours of residue resulting from soil-engaging tools, including

the residue trajectories, residue burial mechanism, and residue displacement (Lin et al., 2024; Zeng et al., 2020; Zeng and Chen, 2019).

2.4.2 Gaps in Soil-Residue-Machine Interaction Modelling

Soil is heterogeneous and has different properties along the depth profile, such as soil bulk density, saturated hydraulic conductivity, and moisture content (Yang et al., 2021). These differences are likely influenced by factors such as tillage practices, levels of machinery compaction, and methods of managing crop residue (Hu et al., 2024; Jabro et al., 2016; Li et al., 2024). Modelling heterogeneous soils is difficult because of the variability of soil properties across the depth profile. Existing studies have modelled agricultural soil by dividing the deep soil profile into multiple layers, each characterized by distinct properties. For example, existing DEM soil models feature a one-layer structure (Makange et al., 2021), a three-layer structure (Hang et al., 2018; Hang et al., 2017b), or a four-layer structure (Tong et al., 2023; Wang et al., 2022; Zhao et al., 2023). These studies were carried out under different soil conditions and machines. Also, they were based on varying assumptions about the soil-layer structure in the DEM models. This makes it difficult to choose the appropriate model, in terms of the number of soil layers in the model. Therefore, this study investigated the impact of soil layers on model prediction accuracies for the same soil-engaging tool under the same soil and field conditions.

Concave discs are commonly used to incorporate crop residue into the soil. It is assumed that a large concave design enhances the mixing process, affecting residue incorporation rate. In practice, disc and tilt angles are often set along with the aggressiveness of the disc blade's curvature. Angle configurations affect the amount of crop residue incorporated into the soil (Malasli and Çelik, 2023) and the soil and residue movement. Additionally, the

length of the crop residue significantly impacted the residue displacements (Liu et al., 2010). However, there is a lack of DEM modelling and simulation studies that examine the micro-dynamic behaviours of crop residue displacement under various disc configurations and residue lengths.

Concave discs are utilized in conservation tillage to cut and incorporate crop residue. The aggressiveness of the disc's cutting action varies depending on several factors. As reported by Zhang et al. (2024b) who developed a soil-disc-maize residue interaction DEM model, a larger disc angle resulted in a higher residue management efficiency. A DEM model that included the disc, soil, and straw was developed by Li et al. (2025) for investigating the effects on the straw cutting and clearing process. However, the dynamic behaviours of crop residue and soil during disc cutting remain poorly understood. In particular, soil properties have been found to influence the effectiveness of crop residue cutting (Aikins et al., 2020). Therefore, this study developed a DEM model to examine the dynamic behaviours of soil and residue under varying soil bulk densities.

Modelling a single disc tool in a tillage implement makes it easier to isolate and understand the behaviour of individual components, such as the effect of tool geometries, speeds, or angles on soil disturbance and residue movement. Researchers often used single-disc models to develop and validate basic assumptions or to compare different operational settings (Murray and Chen, 2018; Sadek et al., 2021; Wang et al., 2019c). However, modelling a single disc does not fully capture the collective behaviour and interactions that occur in actual multi-disc tillage implements. In real field conditions, multiple discs operate simultaneously, often influencing each other's performance through soil displacement, and overlapping working widths. These interactions can affect draft forces, soil disturbance,

residue incorporation and displacement. As such, modelling a disc harrow with multiple discs provides a more realistic and comprehensive simulation of field performance.

Major performance indicators of disc harrow include soil resistance, soil and residue cutting, and residue incorporation. Existing studies suggested that the soil resistance was affected by disc angles, working depths, and working speeds (Ahmadi, 2018; Kogut et al., 2016; Upadhyay and Raheman, 2019). Those operational parameters also had influence on tillage quality (Damanauskas et al., 2019). But the effects of tillage directions relative to residue stubble rows on these dynamic attributes have not been well documented. Also, there was little research on DEM modelling of an entire disc harrow. This study fills in this gap by developing a soil-residue-harrow model to simulate the dynamic behaviours of soil and residue resulting from the tillage action of multiple discs.

2.5. Summary

This research presented a comprehensive investigation into the interactions among disc-type tillage implements, soil, and crop residue through both experimental and numerical approaches. The performance of disc implements depended on key structural parameters such as disc geometry, gang angle, and tilt angle. All of which influenced soil cutting, residue and soil displacement, and power requirements. Operational parameters, such as working depth and forward speed also significantly affected tillage quality, residue incorporation, and energy consumption. Additionally, soil properties (such as soil bulk density) and residue characteristics (such as residue length) directly impacted the implement's performance.

Although numerous previous studies have focused on soil-tool interactions, the role of crop residue has often been underrepresented. This study addressed this gap by systematically studying dynamic behaviours of different crop residue under shallow and deep tillage. Residue cutting, incorporation, and displacements were examined under both laboratory and field conditions. To complement the experiments, Discrete Element Models (DEM) were developed to simulate the interactions among soil, residue, and tillage tools. These models were incorporated with layered soil structures, variable bulk densities, realistic residue properties, and multiple-disc interactions. The models provided accurate predictions of tillage processes under various field conditions.

2.6. References

Abo-Elnor, M., Hamilton, R., and Boyle, J. T., 2004. Simulation of soil-blade interaction for sandy soil using advanced 3D finite element analysis. Soil and Tillage Research, 75(1), 61–73. https://doi.org/10.1016/S0167-1987(03)00156-9

Abu-Hamdeh, N. H., and Reeder, R. C., 2003. A nonlinear 3D finite element analysis of the soil forces acting on a disk plow. Soil and Tillage Research, 74(2), 115–124. https://doi.org/10.1016/S0167-1987(03)00152-1

Acquah, K., and Chen, Y., 2021. Discrete element modelling of soil compaction of a Press-Wheel. AgriEngineering, 3(2), 278–293. https://doi.org/10.3390/agriengineering3020019

Acquah, K., and Chen, Y., 2023. Discrete element modelling of soil pressure under varying number of tire passes. Journal of Terramechanics, 107, 23–33. https://doi.org/10.1016/j.jterra.2023.02.003

Adam, K. M. and Erbach, D. C., 1992. Secondary tillage tool effect on soil aggregation. Transactions of the ASAE, 35(6), 1771–1776. https://doi.org/10.13031/2013.28796

Ahmadi, I., 2018. A draught force estimator for disc harrow using the laws of classical soil mechanics. Biosystems Engineering, 171, 52–62. https://doi.org/10.1016/j.biosystemseng.2018.04.008

Aikins, K. A., Barr, J. B., Ucgul, M., Jensen, T. A., Antille, D. L., and Desbiolles, J. M. A., 2020. No-tillage furrow opener performance: A review of tool geometry, settings and interactions with soil and crop residue. Soil Research (Collingwood, Vic.), 58(7), 603–621. https://doi.org/10.1071/SR19153

Altair Engineering Inc., 2019. Altair® EDEM™ [Computer software]. https://www.altair.com/edem/

Al-Janobi, A. A., 1998. Draft of primary tillage implements in sandy loam soil. Applied Engineering in Agriculture, 14(4), 343–348. https://doi.org/10.13031/2013.19392

Al-Kaisi, M. M. and Guzman, J. G., 2013. Effects of tillage and nitrogen rate on decomposition of transgenic Bt and near-isogenic non-Bt maize residue. Soil and tillage research, 129, 32–39. https://doi:10.1016/j.still.2013.01.004.

Armin, A., Fotouhi, R., and Szyszkowski, W., 2014. On the FE modeling of soil-blade interaction in tillage operations. Finite Elements in Analysis and Design, 92, 1–11. https://doi.org/10.1016/j.finel.2014.07.004

Bahrami, M., Naderi-Boldaji, M., Ghanbarian, D., and Keller, T., 2022. Simulation of soil stress under plate sinkage loading: A comparison of finite element and discrete

element methods. Soil and Tillage Research, 223, e105463. https://doi.org/10.1016/j.still.2022.105463

Bahrami, M., Naderi-Boldaji, M., Ghanbarian, D., Ucgul, M., and Keller, T., 2020. DEM simulation of plate sinkage in soil: Calibration and experimental validation. Soil and Tillage Research, 203, e104700. https://doi.org/10.1016/j.still.2020.104700

Baker, C. J, Keith E Saxton, W. R Ritchie, and C.A.B., 1996. International. No-Tillage Seeding: Science and Practice. Wallingford: CAB International.

Barr, J. B., Ucgul, M., Desbiolles, J. M. A., and Fielke, J. M., 2018. Simulating the effect of rake angle on narrow opener performance with the discrete element method. Biosystems Engineering, 171, 1–15. https://doi.org/10.1016/j.biosystemseng.2018.04.013

Bentaher, H., Ibrahmi, A., Hamza, E., Hbaieb, M., Kantchev, G., Maalej, A., and Arnold, W., 2013. Finite element simulation of moldboard-soil interaction. Soil and Tillage Research, 134, 11–16. https://doi.org/10.1016/j.still.2013.07.002

Bianchini, A., and Magalhães, P. S. G., 2008. Evaluation of coulters for cutting sugar cane residue in a soil bin. Biosystems Engineering, 100(3), 370–375. https://doi.org/10.1016/j.biosystemseng.2008.04.012

Boizard, H., Yoon, S. W., Leonard, J., Lheureux, S., Cousin, I., Roger-Estrade, J., and Richard, G., 2013. Using a morphological approach to evaluate the effect of traffic and weather conditions on the structure of a loamy soil in reduced tillage. Soil and Tillage Research, 127(SI), 34–44. https://doi.org/10.1016/j.still.2012.04.007

Chen, Y., Damphousse, S., Li, H., 2016. Vertical tillage and vertical seeding. Paper No. CSBE16-090. In: CSBE/SCGAB 2016 Annual Conference. Halifax, NS, Canada. July 3–6.

Chen, Y., Monero, F. V., Lobb, D., Tessier, S., and Cavers, C., 2004. Effects of six tillage methods on residue incorporation and crop performance in a heavy clay soil. Transactions of the ASAE, *47*(4), 1003–1010. https://doi.org/10.13031/2013.16570

Cheng, Y. P., Bolton, M. D., and Nakata, Y., 2004. Crushing and plastic deformation of soils simulated using DEM. Géotechnique, 54(2), 131–141. https://doi.org/10.1680/geot.2004.54.2.131

Cundall, P., 1971. A computer model for simulating progressive, large-scale movements in blocky rock systems. https://ci.nii.ac.jp/naid/10003194568

Damanauskas, V., Velykis, A., and Satkus, A., 2019. Efficiency of disc harrow adjustment for stubble tillage quality and fuel consumption. Soil and Tillage Research, 194, e104311. https://doi.org/10.1016/j.still.2019.104311

De Pue, J., Di Emidio, G., Verastegui Flores, R. D., Bezuijen, A., and Cornelis, W. M., 2019. Calibration of DEM material parameters to simulate stress-strain behaviour of unsaturated soils during uniaxial compression. Soil and Tillage Research, 194, e104303. https://doi.org/10.1016/j.still.2019.104303

Du, J., Heng, Y., Zheng, K., Luo, C., Zhu, Y., Zhang, J., and Xia, J., 2022. Investigation of the burial and mixing performance of a rotary tiller using discrete element

method. Soil and Tillage Research, 220, e105349. https://doi.org/10.1016/j.still.2022.105349

Duiker, S. W., 2020. In-row subsoiling benefits maize yield on soil with a shallow fragipan. Crop, Forage and Turfgrass Management, 6(1), e20008. https://doi.org/10.1002/cft2.20008

Gupta, P. D., Gupta, C. P., and Pandey, K. P., 1989. An analytical model for predicting draft forces on convex-type wide cutting blades. Soil and Tillage Research, 14(2), 131–144. https://doi.org/10.1016/0167-1987(89)90027-5

Hang, C., Gao, X., Yuan, M., Huang, Y., and Zhu, R., 2018. Discrete element simulations and experiments of soil disturbance as affected by the tine spacing of subsoiler. Biosystems Engineering, 168, 73–82. https://doi.org/10.1016/j.biosystemseng.2017.03.008

Hang, C., Huang, Y., and Zhu, R., 2017a. Analysis of the movement behaviour of soil between subsoilers based on the discrete element method. Journal of Terramechanics, 74, 35–43. https://doi.org/10.1016/j.jterra.2017.10.002

Hang, C., Gao, X., Wang, B., Yuan, M., Huang, Y., and Zhu, R., 2017b. Optimization of the wing parameters for a winged subsoiler. Applied Engineering in Agriculture, 33(3), 313–319. https://doi.org/10.13031/aea.12068

Hipps, N. A., and Hodgson, D. R., 1987. The effect of a slant-legged subsoiler on soil compaction and the growth of direct-drilled winter wheat. The Journal of Agricultural Science, 109(1), 79–85. https://doi.org/10.1017/S0021859600081028

Hoseinian, S. H., Hemmat, A., Esehaghbeygi, A., Shahgoli, G., & Baghbanan, A., 2022. Development of a dual sideway-share subsurface tillage implement: Part 2. Effect of tool geometry on tillage forces and soil disturbance characteristics. Soil and Tillage Research, 215, e105200. https://doi.org/10.1016/j.still.2021.105200

Hu, R., Zheng, B., Liu, Y., Peng, S., Gong, J., Li, J., Qin, T., Liang, J., Xiong, K., Shao, L., Zheng, Z., Yi, Z., Zhou, Q., and Li, J., 2024. Deep tillage enhances the spatial homogenization of bacterial communities by reducing deep soil compaction. Soil and Tillage Research, 239, e106062. https://doi.org/10.1016/j.still.2024.106062

Itasca Consulting Group Inc., 2019. Particle Flow Code in Three Dimensions (PFC3D), Version 6: Theory and background. Minneapolis, MN: Itasca Consulting Group Inc. https://www.itascacg.com/software/pfc

Jabro, J. D., Iversen, W. M., Stevens, W. B., Evans, R. G., Mikha, M. M., and Allen, B. L., 2016. Physical and hydraulic properties of a sandy loam soil under zero, shallow and deep tillage practices. Soil and Tillage Research, 159, 67–72. https://doi.org/10.1016/j.still.2016.02.002

Jiang, X., Tong, J., Ma, Y., and Sun, J., 2020. Development and verification of a mathematical model for the specific resistance of a curved subsoiler. Biosystems Engineering, 190, 107–119. https://doi.org/10.1016/j.biosystemseng.2019.12.004

Karayel, D., Jotautienė, E., and Šarauskis, E., 2024. The effect of furrow opener and disc coulter configurations on seeding performance under different residue cover densities. AgriEngineering, 6(2), 1277–1288. https://doi.org/10.3390/agriengineering6020073

Kogut, Z., Sergiel, L., and Żurek, G., 2016. The effect of the disc setup angles and working depth on disc harrow working resistance. Biosystems Engineering, 151, 328–337. https://doi.org/10.1016/j.biosystemseng.2016.10.004

Kumar, N., Sawant, C. P., Sharma, R. K., Chhokar, R. S., Tiwari, P. S., Singh, D., Roul, A. K., Tripathi, S. C., Gill, S. C., and Singh, G. P., 2021. Combined effect of disc coulters and operational speeds on soil disturbance and crop residue cutting under no-tillage system in soil bin. Journal of Scientific and Industrial Research (New Delhi, India: 1963), 80(9), 739–749. https://doi.org/10.56042/jsir.v80i09.40333

Li, B., Chen, Y., and Chen, J., 2016. Modeling of soil-claw interaction using the discrete element method (DEM). Soil and Tillage Research, 158, 177–185. https://doi.org/10.1016/j.still.2015.12.010

Li, B., Liu, F., Mu, J., Chen, J., and Han, W., 2014. Distinct element method analysis and field experiment of soil resistance applied on the subsoiler. International Journal of Agricultural and Biological Engineering, 7(1), 54–59. https://doi.org/10.3965/j.ijabe.20140701.006

Li, H., Fang, L., Yuan, P., Lu, W., and Yang, W., 2022. A seedbed clearing and shaping device for dry direct-seeded rice. Agriculture (Switzerland), 12(10), e1740. https://doi.org/10.3390/agriculture12101740

Li, J., Chen, L., Zhang, C., Ma, D., Zhou, G., Ning, Q., and Zhang, J., 2024. Combining rotary and deep tillage increases crop yields by improving the soil physical structure and accumulating organic carbon of subsoil. Soil and Tillage Research, 244, e106252. https://doi.org/10.1016/j.still.2024.106252

Li, S., Diao, P., Li, X., Zhao, Y., and Zhao, H., 2025. Design and optimization for straw treatment device using discrete element method (DEM). Agriculture (Switzerland), 15(2), e0152. https://doi.org/10.3390/agriculture15020152

Lin, J., Liao, Q., Wang, X., Kang, Y., Du, W., and Zhang, Q., 2024. Exploring straw movement through the simulation of shovel-type seedbed preparation machine-straw-soil interaction using the DEM-MBD coupling method. Computers and Electronics in Agriculture, 226, e109465. https://doi.org/10.1016/j.compag.2024.109465

Liu, C., 2021. Matrix discrete element analysis of geological and geotechnical engineering (1st ed. 2021.). Springer. https://doi.org/10.1007/978-981-33-4524-9

Liu, G., Xia, J., Zheng, K., Cheng, J., Du, J., and Li, D., 2021. Effects of moisture content and tillage methods on creep properties of paddy soil. PLoS ONE, 16(6), e0253623. https://doi.org/10.1371/journal.pone.0253623

Liu, J., Chen, Y., and Kushwaha, R. L., 2010. Effect of tillage speed and straw length on soil and straw movement by a sweep. Soil and Tillage Research, 109(1), 9–17. https://doi.org/10.1016/j.still.2010.03.014

Liu, X., Qi, H., Wang, S., Xu, Z., Gao, P., Fu, D., and Ma, Y., 2024. The design and experimentation of a wing-shaped stubble-breaking device for maize stubbles. Agriculture (Switzerland), 14(12), e2108. https://doi.org/10.3390/agriculture14122108

Liu, X., Zhou, A., Sun, K., and Shen, S. L., 2023. Discrete element modelling of the macro/micro-mechanical behaviour of unsaturated soil in direct shear tests

including wetting process. Powder Technology, 415, e118125. https://doi.org/10.1016/j.powtec.2022.118125

Magalhães, P. S. G., Bianchini, A., and Braunbeck, O. A., 2007. Simulated and experimental analyses of a toothed rolling coulter for cutting crop residues. Biosystems Engineering, 96(2), 193–200. https://doi.org/10.1016/j.biosystemseng.2006.10.014

Makange, N. R., Ji, C., Nyalala, I., Sunusi, I. I., and Opiyo, S., 2021. Prediction of precise subsoiling based on analytical method, discrete element simulation and experimental data from soil bin. Scientific Reports, 11(1), e11082. https://doi.org/10.1038/s41598-021-90682-w

Makange, N. R., Ji, C., and Torotwa, I., 2020. Prediction of cutting forces and soil behavior with discrete element simulation. Computers and Electronics in Agriculture, 179, e105848. https://doi.org/10.1016/j.compag.2020.105848

Malasli, M. Z., and Çelik, A., 2023. Effects of the disc and tilt angle of a single disc-type furrow opener of a no-till seeder on residue distribution and the furrow profile. Turkish Journal of Agriculture and Forestry, 47(6), 1025–1042. https://doi.org/10.55730/1300-011X.3146

McKyes, E., 1985. Soil cutting and tillage. Elsevier.

Morris, N. L., Miller, P. C. H., Orson, J. H., and Froud-Williams, R. J., 2009. The effect of wheat straw residue on the emergence and early growth of sugar beet (Beta vulgaris) and oilseed rape (Brassica napus). European Journal of Agronomy, 30(3), 151–162. https://doi.org/10.1016/j.eja.2008.09.002

Mouazen, A. M., and Neményi, M., 1999. Finite element analysis of subsoiler cutting in non-homogeneous sandy loam soil. Soil and Tillage Research, 51(1), 1–15. https://doi.org/10.1016/S0167-1987(99)00015-X

Murray, S. E., and Chen, Y., 2018. Soil bin tests and discrete element modeling of a disc opener. Canadian Biosystems Engineering / Le Genie Des Biosystems Au Canada, 60, 21–210. https://doi.org/10.7451/CBE.2018.60.2.1

Nagy, D., Pásthy, L., and Tamás, K., 2024. Development of a GPU-based DEM solver for parameter optimization in the simulations of soil-sweep tool interactions. Computers and Electronics in Agriculture, 227, e109482. https://doi.org/10.1016/j.compag.2024.109482

Onwualu, A. P., and Watts, K. C., 1998. Draught and vertical forces obtained from dynamic soil cutting by plane tillage tools. Soil and Tillage Research, 48(4), 239–253. https://doi.org/10.1016/S0167-1987(98)00127-5

Qi, L., Chen, Y., and Sadek, M., 2019. Simulations of soil flow properties using the discrete element method (DEM). Computers and Electronics in Agriculture, 157, 254–260. https://doi.org/10.1016/j.compag.2018.12.052

Sadek, M. A., Chen, Y., and Zeng, Z., 2021. Draft force prediction for a high-speed disc implement using discrete element modelling. Biosystems Engineering, 202, 133–141. https://doi.org/10.1016/j.biosystemseng.2020.12.009

Saunders, C., Ucgul, M., and Godwin, R. J., 2021. Discrete element method (DEM) simulation to improve performance of a mouldboard skimmer. Soil and Tillage Research, 205, e104764. https://doi.org/10.1016/j.still.2020.104764

Schjønning, P., 2023. An empirical model for prediction of topsoil deformation in field traffic. Soil and Tillage Research, 227, e105589. https://doi.org/10.1016/j.still.2022.105589

Shahgoli, G., Fielke, J., Saunders, C., and Desbiolles, J., 2010. Simulation of the dynamic behaviour of a tractor-oscillating subsoiler system. Biosystems Engineering, 106(2), 147–155. https://doi.org/10.1016/j.biosystemseng.2010.03.002

Sun, J., Wang, Y., Ma, Y., Tong, J., and Zhang, Z., 2018. DEM simulation of bionic subsoilers (tillage depth >40 cm) with drag reduction and lower soil disturbance characteristics. Advances in Engineering Software, 119, 30–37. https://doi.org/10.1016/j.advengsoft.2018.02.001

Tamás, K., 2018. The role of bond and damping in the discrete element model of soil-sweep interaction. Biosystems Engineering, 169, 57–70. https://doi.org/10.1016/j.biosystemseng.2018.02.001

Tamás, K., Jóri, I. J., and Mouazen, A. M., 2013. Modelling soil-sweep interaction with discrete element method. Soil and Tillage Research, 134, 223–231. https://doi.org/10.1016/j.still.2013.09.001

Tan, H., Shen, C., Ma, J., Wu, C., Xu, L., and Ma, S., 2025. The reduction of energy consumption and soil disturbance mechanisms in trenching using biomimetic blades. Computers and Electronics in Agriculture, 230, e109887. https://doi.org/10.1016/j.compag.2024.109887

Tian, P., Lian, H., Wang, Z., Jiang, Y., Li, C., Sui, P., and Qi, H., 2020. Effects of deep and shallow tillage with straw incorporation on soil organic carbon, total nitrogen

and enzyme activities in Northeast China. Sustainability (Switzerland), 12(20), 1–15. https://doi.org/10.3390/su12208679

Tiessen, K. H. D., Lobb, D. A., Mehuys, G. R., and Rees, H. W., 2007. Tillage erosion within potato production in Atlantic Canada: II. Erosivity of primary and secondary tillage operations. Soil and Tillage Research, 95(1–2), 320–331. https://doi.org/10.1016/j.still.2007.02.009

Tong, J., Jiang, X. H., Wang, Y. M., Ma, Y. H., Li, J. W., and Sun, J. Y., 2020. Tillage force and disturbance characteristics of different geometric-shaped subsoilers via DEM. Advances in Manufacturing, 8(3), 392–404. https://doi.org/10.1007/s40436-020-00318-x

Tong, Z., Li, H., He, J., Wang, Q., Lu, C., Wang, C., Zhong, G., Cui, D., and Li, D., 2023. Design and experiment of in situ soil-lifting shovel for direct-injection straw deep-burial machine. Agriculture (Switzerland), 13(9), e1650. https://doi.org/10.3390/agriculture13091650

Torbert, H. A., Ingram, J. T., and Prior, S. A., 2007. Planter aid for heavy residue conservation tillage systems. Agronomy Journal, 99(2), 478–480. https://doi.org/10.2134/agronj2006.0114

Ucgul, M., Fielke, J. M., and Saunders, C., 2015. Three-dimensional discrete element modelling (DEM) of tillage: Accounting for soil cohesion and adhesion. Biosystems Engineering, 129, 298–306. https://doi.org/10.1016/j.biosystemseng.2014.11.006

Ucgul, M., and Saunders, C., 2020. Simulation of tillage forces and furrow profile during soil-mouldboard plough interaction using discrete element modelling. Biosystems Engineering, 190, 58–70. https://doi.org/10.1016/j.biosystemseng.2019.11.022

Ucgul, M., Saunders, C., and Fielke, J. M., 2017. Discrete element modelling of tillage forces and soil movement of a one-third scale mouldboard plough. Biosystems Engineering, 155, 44–54. https://doi.org/10.1016/j.biosystemseng.2016.12.002

Ucgul, M., Saunders, C., and Fielke, J. M., 2018a. Comparison of the discrete element and finite element methods to model the interaction of soil and tool cutting edge. Biosystems Engineering, 169, 199–208. https://doi.org/10.1016/j.biosystemseng.2018.03.003

Ucgul, M., Saunders, C., Li, P., and Lee, S. H., 2018b. Analyzing the mixing performance of a rotary spader using digital image processing and discrete element modelling (DEM). Computers and Electronics in Agriculture, 151, 1–10. https://doi.org/10.1016/j.compag.2018.05.028

Upadhyay, G., and Raheman, H., 2019. Specific draft estimation model for offset disc harrows. Soil and Tillage Research, 191, 75–84. https://doi.org/10.1016/j.still.2019.03.021

Upadhyay, G., and Raheman, H., 2018. Performance of combined offset disc harrow (front active and rear passive set configuration) in soil bin. Journal of Terramechanics, 78, 27–37. https://doi.org/10.1016/j.jterra.2018.04.002

Vigil, M. F., 1995 (Merle F., United States. Agricultural Research Service., and United States. Central Great Plains Research Station. Factors affecting the rate of crop residue decomposition under field conditions. USDA-ARS.

Wang, H., Wang, L., Huang, X., Gao, W., and Ren, T., 2021. An empirical model for estimating soil penetrometer resistance from relative bulk density, matric potential, and depth. Soil and Tillage Research, 208, e104904. https://doi.org/10.1016/j.still.2020.104904

Wang, X., Gao, P., Yue, B., Shen, H., Fu, Z., Zheng, Z., Zhu, R., and Huang, Y., 2019a. Optimisation of installation parameters of subsoiler' wing using the discrete element method. Computers and Electronics in Agriculture, 162, 523–530. https://doi.org/10.1016/j.compag.2019.04.044

Wang, X., Zhang, S., Pan, H., Zheng, Z., Huang, Y., and Zhu, R., 2019b. Effect of soil particle size on soil-subsoiler interactions using the discrete element method simulations. Biosystems Engineering, 182, 138–150. https://doi.org/10.1016/j.biosystemseng.2019.04.005

Wang, X., Zhou, H., and Ji, J., 2022. Effect of mounting angle on bending subsoiling tool–soil interactions using DEM simulations. Agriculture (Switzerland), 12(11), e1830. https://doi.org/10.3390/agriculture12111830

Wang, Y., Wei, Z., Su, G., Zhang, X., Wang, X., Cheng, X., Wang, F., Li, X., Zhou, H., Yang, Z., and Jin, C., 2025. Design and study of anti-blocking type potato stubble disc clamping and pulling device based on MBD-DEM coupled simulation.

Computers and Electronics in Agriculture, 229, e109733. https://doi.org/10.1016/j.compag.2024.109733

Wang, Y., Xue, W., Ma, Y., Tong, J., Liu, X., and Sun, J., 2019c. DEM and soil bin study on a biomimetic disc furrow opener. Computers and Electronics in Agriculture, 156, 209–216. https://doi.org/10.1016/j.compag.2018.11.023

Wang, Y., Zhang, D., Yang, L., Cui, T., Jing, H., and Zhong, X., 2020. Modeling the interaction of soil and a vibrating subsoiler using the discrete element method. Computers and Electronics in Agriculture, 174, e105518. https://doi.org/10.1016/j.compag.2020.105518

Wiese, Allen F., 1985. Weed Control in Limited-Tillage Systems. Champaign, IL: Weed Science Society of America.

Xie, D., He, J., Liu, T., Liu, C., Zhao, G., and Chen, L., 2024. Establishment and validation the DEM-MBD coupling model of flexible straw-Shajiang black soil-walking mechanism interactions. Computers and Electronics in Agriculture, 224, e109203. https://doi.org/10.1016/j.compag.2024.109203

Yang, Y., Wu, J., Zhao, S., Mao, Y., Zhang, J., Pan, X., He, F., and Van Der Ploeg, M., 2021. Impact of long-term sub-soiling tillage on soil porosity and soil physical properties in the soil profile. Land Degradation and Development, 32(10), 2892–2905. https://doi.org/10.1002/ldr.3874

Zeng, Z., and Chen, Y., 2019. Simulation of straw movement by discrete element modelling of straw-sweep-soil interaction. Biosystems Engineering, 180, 25–35. https://doi.org/10.1016/j.biosystemseng.2019.01.009

Zeng, Z., Chen, Y., and Zhang, X., 2017. Modelling the interaction of a deep tillage tool with heterogeneous soil. Computers and Electronics in Agriculture, 143, 130–138. https://doi.org/10.1016/j.compag.2017.10.005

Zeng, Z., Ma, X., Chen, Y., and Qi, L., 2020. Modelling residue incorporation of selected chisel ploughing tools using the discrete element method (DEM). Soil and Tillage Research, 197, e104505. https://doi.org/10.1016/j.still.2019.104505

Zeng, Z., Thoms, D., Chen, Y., and Ma, X., 2021. Comparison of soil and corn residue cutting performance of different discs used for vertical tillage. Scientific Reports, 11(1), e2537. https://doi.org/10.1038/s41598-021-82270-9

Zhang, C., Wang, X., Guo, M., Zhao, J., and Li, M., 2024a. A compacting device of rice dry direct-seeding planter based on DEM-MFBD coupling simulation significantly improves the seedbed uniformity and seedling emergence rate. Biosystems Engineering, 246, 26–40. https://doi.org/10.1016/j.biosystemseng.2024.07.018

Zhang, F., Li, M., Peng, M., Chen, C., and Zhang, L., 2019. Three-dimensional DEM modeling of the stress–strain behavior for the gap-graded soils subjected to internal erosion. Acta Geotechnica, 14(2), 487–503. https://doi.org/10.1007/s11440-018-0655-4

Zhang, L. B., Cai, Z. X., and Liu, H. F., 2018. A novel approach for simulation of soil-tool interaction based on an arbitrary Lagrangian–Eulerian description. Soil and Tillage Research, 178, 41–49. https://doi.org/10.1016/j.still.2017.12.011

Zhang, L., Zhai, Y., Chen, J., Zhang, Z., and Huang, S., 2022a. Optimization design and performance study of a subsoiler underlying the tea garden subsoiling mechanism based on bionics and EDEM. Soil and Tillage Research, 220, e105375. https://doi.org/10.1016/j.still.2022.105375

Zhang, S., Huang, Y., Gao, X., Bi, Y., Dong, J., Zhao, H., Zhao, P., and Jia, X., 2025. Evaluating the influence of straight-plain types of rotary tiller blades with various edge curves on maize residue using DEM. Biosystems Engineering, 250, 49–61. https://doi.org/10.1016/j.biosystemseng.2024.11.016

Zhang, S., Jia, X., Dong, J., Wang, X., Zhao, H., Chen, X., Zhang, Z., Huang, Y., and Shi, J., 2024b. Optimization of operating angles of disc coulters for maize residue management using discrete element method. Computers and Electronics in Agriculture, 218, e108691. https://doi.org/10.1016/j.compag.2024.108691

Zhang, X., Zhang, L., Hu, X., Wang, H., Shi, X., and Ma, X., 2022b. Simulation of soil cutting and power consumption optimization of a typical rotary tillage soil blade. Applied Sciences (Switzerland), 12(16), e8177. https://doi.org/10.3390/app12168177

Zhao, H., Li, H., Ma, S., He, J., Wang, Q., Lu, C., Zheng, Z., and Zhang, chao., 2020. The effect of various edge-curve types of plain-straight blades for strip tillage seeding on torque and soil disturbance using DEM. Soil and Tillage Research, 202, e104674. https://doi.org/10.1016/j.still.2020.104674

Zhao, J., Lu, Y., Wang, X., Zhuang, J., and Han, Z., 2023. A bionic profiling-energy storage device based on MBD-DEM coupled simulation optimization reducing

the energy consumption of deep loosening. Soil and Tillage Research, 234. e105824. https://doi.org/10.1016/j.still.2023.105824

Zheng, K., Cheng, J., Xia, J., Liu, G., and Xu, L., 2021. Effects of soil bulk density and moisture content on the physico-mechanical properties of paddy soil in plough layer. Water (Switzerland), 13(16), e2290. https://doi.org/10.3390/w13162290

Chapter 3: Discrete Element Modelling of the Effect of Disc Angle and Tilt Angle on Residue Incorporation Resulting from a Concave Disc *

*Published in *Computer and Electronics in Agriculture* 224, e109222

3.1. Abstract

Understanding crop residue behaviour during tillage is critical for improving performance of tillage tools for conservation agriculture. A laboratory experiment was conducted using a concave disc to incorporate corn residue into sandy loam soil. Dynamic attributes, including soil cutting forces and residue incorporation, were measured under different lengths (75, 125, and 200 mm) of corn residue at constant disc and tilt angles. A residue-disc-soil interaction model was developed using discrete element method (DEM). Model parameters were calibrated and validated using experimental data. The validated model was used to predict the dynamic attributes at different disc and tilt angles. Experimental results demonstrated a general increasing trend in draft force (F_D) and residue incorporation rate (R_I), as the corn residue length increased. The two calibrated model parameters, stiffness of soil particle and stiffness of soil-residue interface were 1.15×10^6 and 13.5 N m^{-1} respectively. The validated model had an average relative error of 9.0% and 18.2% for predicting R_I and F_D respectively, as compared with the measurements. Within the angle range of 10° to 30°, the F_D and R_I decreased as the tilt angle (α) increased, whereas increased as the disc angle (β) increased. The effects of β were more pronounced than those of α. The optimal angles were $\alpha = 20°$, $\beta = 25°$ which resulted in a minimum F_D and a maximum R_I. The results provided

new insight into residue-disc-soil dynamics and could be used to guide the selection of disc operating parameters.

Keywords: Residue length; DEM; Disc; Displacement; Corn

3.2. Introduction

Crop residue management is one of the themes for conservation agriculture systems. Leaving crop residue on the soil surface can reduce soil erosion and runoff. However, excessive residue remaining in fields hinders the early crop growth, resulting in losses of the crop yield (Li et al., 2022). Therefore, understanding the effectiveness of residue displacement and incorporation is important for tillage tools (Hobbs et al., 2008; Lal et al., 2007). Some traditional tillage implements, such as mouldboard ploughs (Arvidsson and Hillerström, 2010), rotary tillers (Zhou et al., 2020; Zhu et al., 2023), and power harrow (Celik and Altikat, 2022), were designed to incorporate residue into soil. Other tools were designed to displace only the portion of crop residue (Li et al., 2024; Chen et al., 2024). But those tools aggressively disturb soil and leave little residue on the soil surface, therefore increasing the risk of soil erosion and runoff. Concave discs are designed to partially incorporate crop residue into soil meanwhile keeping some residue on the soil surface for soil conservation and environment protection.

Existing studies on discs mainly concerned the effects on tillage forces, soil disturbance, and residue cutting performance of discs. For example, a study was conducted to evaluate the draft requirement and straw cutting performance of different disc openers (Ahmad et al., 2015). The effects of different disc coulters and operational speeds on soil disturbance and residue cutting were investigated in Kumar et al. (2021). A biomimetic disc was evaluated in comparison with several traditional discs in terms of tillage forces, residue cutting efficiency, and soil disturbance

(Torotwa et al., 2021). As the disc advanced in the field, crop residue was displaced and mixed with soil. Research into this process could lead to a better understanding of the mechanisms of residue incorporating. However, residue incorporation and displacements caused by a concave disc have not been well documented yet.

In practice, disc plow was tilted at an angle and placed at a disc angle. Therefore, the tilt angle and disc angle were considered to be critical indicators affecting the working effect of the disc. For instance, the increase in tilt angle of plain disc from 0° to 20° resulted in higher soil displacement (Murray and Chen, 2018). For notched concave disc harrow, an increase of disc angle from 12° to 21° and tilt angle from 7° to 15° caused an increase in draft force while a decrease in vertical force (Kogut et al., 2016). But the draft force of concave plain disc was positively affected by disc angle while negatively affected by tilt angle (Sadek et al., 2021). It is foreseeable that the effects of tilt angle and disc angle were complex and due to the difference in residue conditions, soil textures, disc physical parameters, etc. However, most of existing literature was limited to evaluate soil displacements and tillage forces. There was a lack of deep understanding of the difference in residue behaviours caused by adjusting disc angle and tilt angle.

Regardless of the types of tillage tool, residue length prior to tillage operation affects residue incorporation and displacement. For instance, the effects of rice straw length were investigated by Xu et al. (2022a; 2022b), indicating that less rice residue was incorporated into soil by a rotary tiller when the residue length increased from 30 to 150 mm. A soil bin experiment was conducted to study the influence of residue length on residue movement and incorporation by tillage with a sweep. The results showed that less cereal residue was incorporated into soil as the residue length increased (Liu et al., 2010). Moreover, no particular trend of wheat residue displacement was found with the increasing of residue lengths from 130 to 230 mm in a rotary blade test (Fang et al., 2016).

These existing studies focused on cereal residue. Little research was done on effects of residue length for corn.

To better understand residue incorporation and displacement resulting from discs, the prerequisite is to understand the interaction of residue-disc-soil that is a complex system. A numerical modelling method, discrete element method (DEM) has become an effective approach in modelling dynamic behaviours of soil and tillage tools (Tekeste et al., 2019; Zhao et al., 2021). This method has been applied to study soil dynamic attributes resulting from different tillage tools, such as subsoilers (Zeng et al., 2017), mouldboard plows (Saunders et al., 2021), and sweeps (Zeng et al., 2020; Zeng and Chen, 2019). DEM has also been applied to discs. For example, inspired by digging animals, Wang et al. (2019) designed biomimetic discs and analysed their resistance-reduction performance using the DEM. The effects of disc operating parameters on draft forces were examined using DEM (Sadek et al., 2021). The tillage forces affected by disc angles were predicted in DEM model (Murray and Chen, 2018; Khosravani et al., 2023). Different types of discs were evaluated in terms of the draft force using DEM simulation (Ahmad et al., 2020). Soil movement analysis was conducted using the DEM simulation of soil-disc plough interaction (Ucgul, 2023). As for the interaction between soil, residue, and disc, some studies using DEM models aimed at the residue cutting behaviours of disc openers (Liu et al., 2023; Zhong et al., 2023), or optimized the operating angles of disc coulters (Zhang et al., 2024). However, disc plows, the leading tillage tools in conservation tillage system, have not been well documented, in terms of DEM modelling of corn residue dynamic behaviours under a concave disc.

In summary, there was the shortage of current research on concave disc for managing soil and residue. Specifically, soil and residue dynamic behaviours as concave disc advanced, such as tillage forces, residue displacements, residue incorporation, residue trajectories, and velocity

distribution of soil and residue have not been well documented. There was also lacking investigation of the effects of corn residue length and angle setup of disc (disc angle and tilt angle) on soil and residue dynamic behaviours. Therefore, DEM model was used to fill up the current shortage of concave disc research. The specific objectives of this study were to (1) develop a residue-disc-soil interaction model using the DEM, (2) calibrate and validate the model using soil bin testing data of residues with various lengths, and (3) apply the validated model to investigate the effects of tilt and disc angle on residue dynamic attributes.

3.3. Methodology

3.3.1 Description of the Disc

A shallow concave plain disc (Figure 3.1a) was studied. The disc was a commercial disc, and it was designed for primary tillage. The disc was 508 mm in diameter, 38 mm in concavity, and 6.5 mm in thickness. The radius of the concave arc was 760 mm. The centre of the disc was a circular plane with a diameter of 130 mm. The disc was tested in a laboratory condition and its interaction with soil and corn residue was modelled, as described in the following sections.

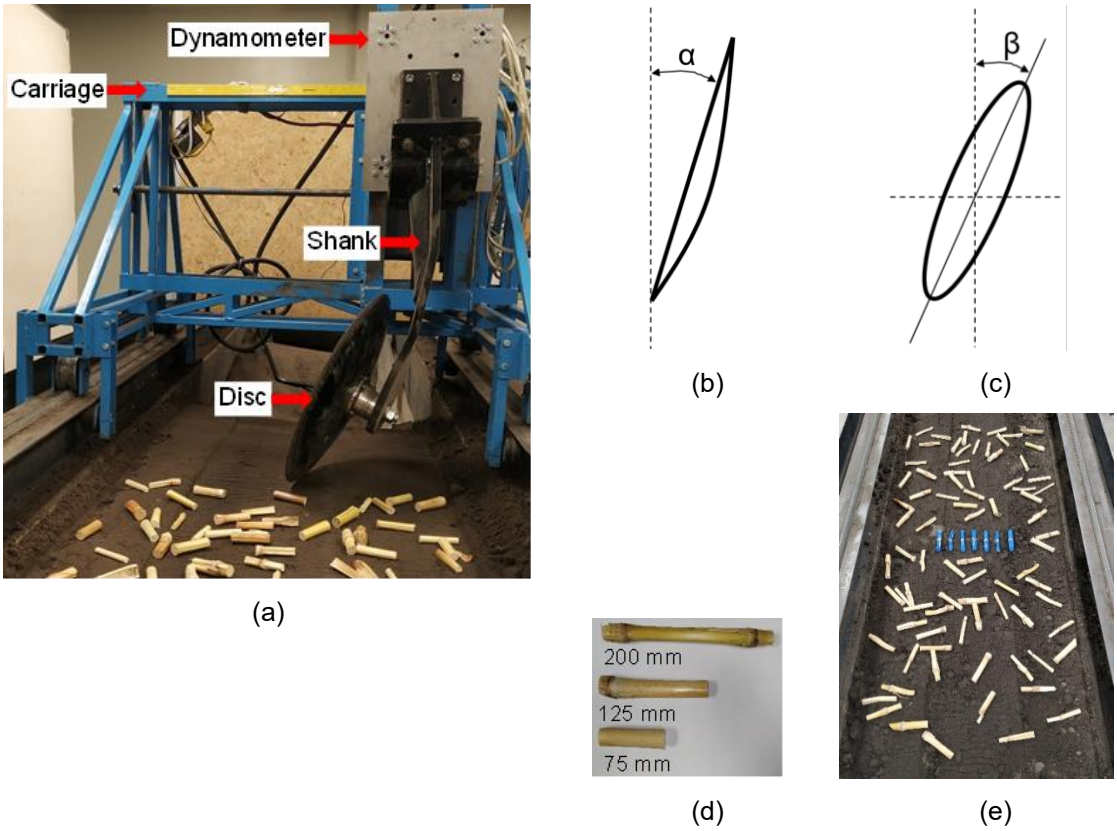

(a) (b) (c) (d) (e)

Figure 3.1. Soil bin setup: (a) disc and shank mounted on the carriage via a plate dynamometer; (b) tilt angle, *α*; (c) disc angle, *β*; (d) three different lengths of corn residue; and (e) corn residue randomly spread on the soil surface prior to tillage and residue tracers (blue colour) for measuring residue displacement.

3.3.2 Experiment

3.3.2.1 Soil Bin Test Setup

The disc was tested in an indoor soil bin at the Soil Dynamics and Machinery Lab, University of Manitoba, Canada. The disc was mounted on the original twisted rigid shank that was attached to the soil bin carriage. A plate dynamometer was located in between disc shank and soil bin carriage to measure soil cutting forces exerted on the disc in perspective directions (Figure 3.1a). The soil bin was 10 m in length, 0.9 m in width, and 0.6 m in depth and filled with sandy loam soil (70% sand, 16% silt, and 14% clay). A standardized procedure of tilling by a cultivator, levelling by a plate, and compacting by a roller was used for soil preparation prior to each test to ensure a

consistent soil physical condition. Before tests, a core sampler (50 mm in diameter and 100 mm in height) was used to take soil samples randomly from eight locations in the soil bin. The average moisture content and dry bulk density of soil were 19.7% (d.b.) and 1209.9 kg m^{-3} respectively measured using the oven-drying method (ASABE Standards, 2020; ASTM Standards, 2016).

3.3.2.2 Experimental Design

The experiment was a completely randomized design with three lengths of corn residue segments as treatments, i.e., 200, 125, and 75 mm (namely *L200*, *L125*, and *L75*). These lengths represented three major ranges of distribution of residue length in the field (Hanajima, 2020). Tests were done with one residue length at a time, i.e. the length of all corn residues in each test was consistent. For each test, a total of 500 g of corn residue segments was spread on the soil surface, regardless of residue length. This amount of residue was an equivalent reported residue cover (Shinners and Binversie, 2007). Each treatment was replicated four times, giving a total of 12 test runs. For all treatments, the disc was operated at a depth of 80 mm, a common working depth in conservation tillage system (Wang et al., 2018). Limited by the soil bin testing facilities, a travelling speed of 8 km h^{-1} was used. The disc was set at a tilt angle of 20° (α, the angle between the circumferential plane of disc and the vertical plane, as shown in Figure 3.1b) and a disc angle of 17° (β, the angle between the circumferential plane of disc and the direction of disc travelling, as shown in Figure 3.1c), as they were commonly used in conservation tillage research (Zeng et al., 2021). The definitions of α and β were referred to Sadek et al. (2021). These operational parameters were kept constants for all treatments.

Corn stovers were collected in a field at the end of growing season. The stalk part accounts for over 60% of total residue biomass of corn stover (Shinners and Binversie, 2007), and the stalk part of stover has a regular shape than any other parts of stover. Thus, to reduce experimental errors,

corn stovers were stripped of leaves, ears, husks, and upper one third of height. The rest of the stalk was cut into segments to be used in the experiment (Figure 3.1d). The corn residue segments were weighed and oven-dried at 55 °C for 72 h and then re-weighed to determine the moisture content, giving an average moisture content of 4.3% (w.b.). Such a low moisture content was the result of the corn stalk being stored in the laboratory for two weeks before the experiment. For a test, corn residue segments were randomly spread over a 2 m by 0.9 m soil surface area in the soil bin (Figure 3.1e).

3.3.2.3 Measurements

Corn residue tracers were used to measure the displacements of corn residue resulting from the disc operation. Residue tracers had the length corresponding to the length of corn residue segments of the current test run, and they were coloured by blue dye. Seven tracers were placed across the soil bin, as shown in Figure 3.1e. To determine the positions of tracers relative to the disc, the disc was inserted into soil at the target depth, disc angle, and tilt angle, then a contact contour (*A*-*B*) of soil surface intersects with the disc was formed (Figure 3.2a). The first tracer was positioned on the front point of the contact contour (point *A*), which represented a zero distance (D_0) of residue relative to disc. The rest of the six tracers represented distances of 60 (D_{60}), 120 (D_{120}), 180 (D_{180}), 240 (D_{240}), 300 (D_{300}), and 360 mm (D_{360}). The forward and lateral displacements of tracers were recorded using two rulers laid perpendicular to each other (Figure 3.2b). The vertical displacements of tracers were measured using a horizontal pole, extended from a burette stand relative to the soil surface (Figure 3.2c). The difference between the measurement in vertical direction before and after tillage was defined as the residue vertical displacement.

Residue incorporation rate (R_I) was indirectly measured by image analysis. An image of the soil surface with residue was taken before the tillage operation. Then, an image was taken after the

tillage operation (Figure 3.2d). In MATLAB, a thresholding method was implemented to binarize the image (Figure 3.2e) as black-and-white with white pixels representing residue and black pixels representing soil. The difference in the number of white pixels before and after tillage was determined. The R_I was defined as ratio of the difference to the total number of pixels.

The soil cutting forces exerted on the disc in three perspective directions, namely draft (F_D), vertical (F_V), and lateral forces (F_L) were measured by the plate dynamometer aforementioned. The force signals of the dynamometer were recorded using a datalogger and a computer at 65 Hz.

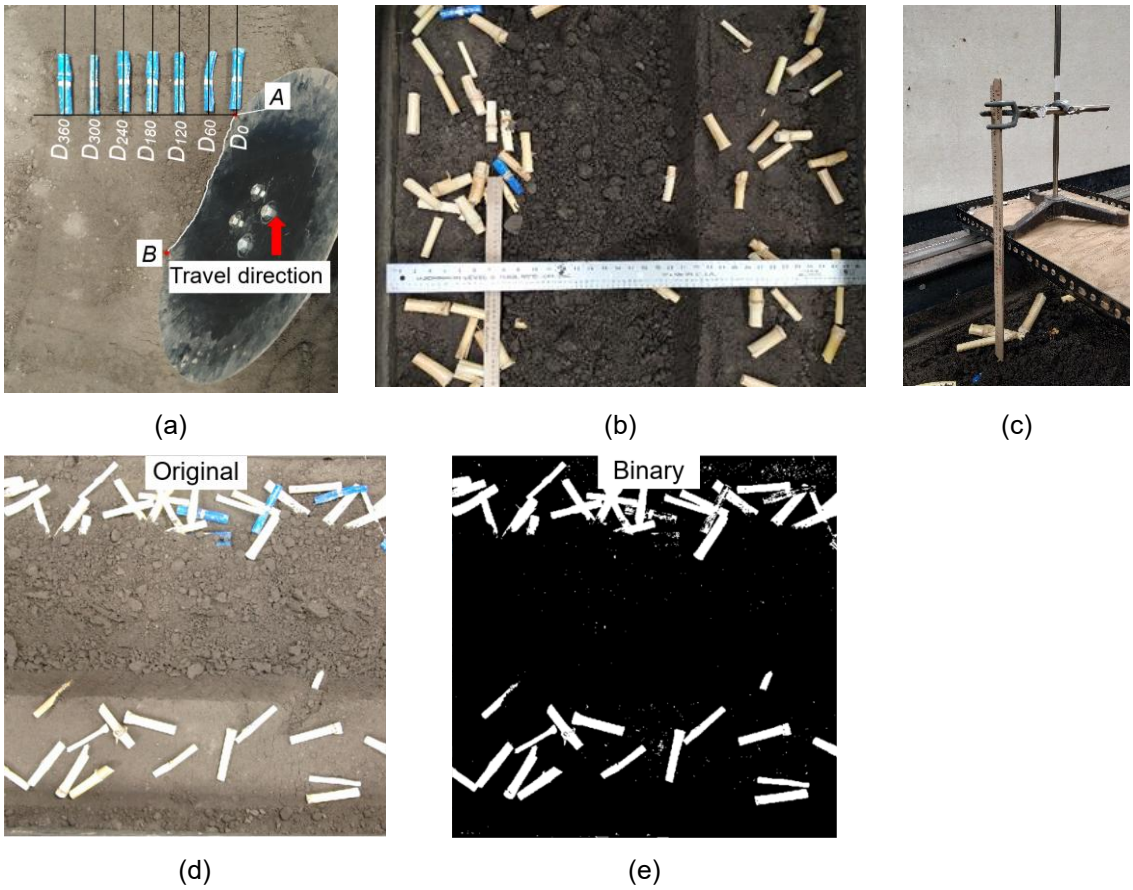

Figure 3.2. Measurements during the experiment: (a) the layout of residue tracers, where curve A-B is the contact contour between soil surface and disc, D_0 to D_{360} represent the residue tracer distances relative to the disc, from 0 to 360 mm with an interval of 60 mm; (b) measurements of forward and lateral residue displacements; (c) measurements of vertical residue displacement; (d) original images after tillage operation; and (e) binarized images using MATLAB processing.

3.3.2.4 Data Analysis

Analysis of variance (ANOVA) of test results was performed using statistical software (R studio). This analysis was used to determine if the residue length had a significant effect on measured variables and to examine the variation of residue displacement at different distances relative to the disc. The means of each measurement were compared with Duncan's multiple range test at the significance level of 0.05.

3.3.3 Residue-Disc-Soil Interaction Model

3.3.3.1 Model Development and Monitoring of Soil and Residue Dynamics

A residue-disc-soil numerical model was developed using DEM software, Particle Flow Code in Three Dimensions (PFC^{3D}). In the model, soil was represented by an assembly of spherical particles. In the literature, several studies showed that soil disturbance and tillage forces were not significantly affected by the particle size when the particle diameter was less than 18 mm (Wang et al., 2021). In addition, many studies have used uniform particle size for DEM soil-tool-residue interaction models (Chen et al., 2024; Zhu et al., 2023; Zeng et al., 2020). Therefore, the particle diameter in this study was 10 mm for maintaining computation time to be practical, meanwhile not significantly affecting the model results. The interaction between soil particles was described by a PFC^{3D} built-in contact model, parallel bond model (PBM) (Potyondy and Cundall, 2004). The PBM features bonds between particles, which reflects the cohesion of agricultural soils. Soil particles were generated in a virtual soil bin of 1700 mm in length and 1100 mm in width (Figure 3.3a). After soil particles were stabilized (reached an equilibrium state), extra soil particles were deleted to form a flat soil surface. The final soil assembly in the virtual soil bin had a total of 314,286 particles and a depth of 160 mm.

A corn residue segment was modelled as a cylinder (Figure 3.3a) using a rigid block (named RBlock in PFC^{3D}). The model corn residue segment was not breakable. To be consistent with the soil bin test, the model residue segment also had three lengths (200, 125, and 75 mm). The diameter of the model residue segment was 17.7 mm, determined by the measured average diameter of the residue samples used in soil bin test. The density of model residue segment was 178.3 kg m^{-3}, determined by the average values of dimensions and mass (assuming that the residue segment is an isotropic cylinder). A total of 520 g of model residue segments were randomly spread over the

1.7 m by 1.1 m soil surface area, representing the same residue cover as in the soil bin test (Figure 3.3a). Given the dimensions and density of each length of model residue and total mass of residue, the numbers of model residue segments were determined, and there were 54, 85, and 158 segments for the treatments of *L200*, *L125*, and *L75* respectively. The PFC^{3D} built-in linear contact model (LM) was used to imitate the interaction between residue and soil.

A model disc was created using a 3D computer-aided design software and then imported into PFC^{3D}. Before running the model, the disc was set at a desired disc angle and tilt angle, and it was positioned at one end of the soil bin at a desired working depth. Then, the model disc was assigned a desired travelling speed (linear speed). Its rotation speed was derived from the linear speed, assuming the rotational radius of the disc being equal to the radius of the disc (Murray and Chen, 2018). As the disc travels through the soil and residue, the disc interacted with soil particles and residue, resulting in displacements of soil and residue, as shown in Figure 3.3b.

The model outputs monitored included draft force (F_D), lateral force (F_L), vertical force (F_V), residue trajectory, residue displacements, and residue incorporation rate (R_I). The F_D, F_L, and F_V of disc were obtained by recording contact forces between disc and soil and residue in perspective directions, as the disc travelled. Seven residue tracers were placed on the soil surface (Figure 3.3a) with the same orientation, positions, and spacing as in the soil bin test. The trajectory of each residue tracer was traced as the disc advanced. After the disc ran through the soil, the position of the tracer was recorded to determine the residue displacements. Images of the soil surface before and after disc tillage were taken and then processed in MATLAB using the thresholding method to evaluate the R_I.

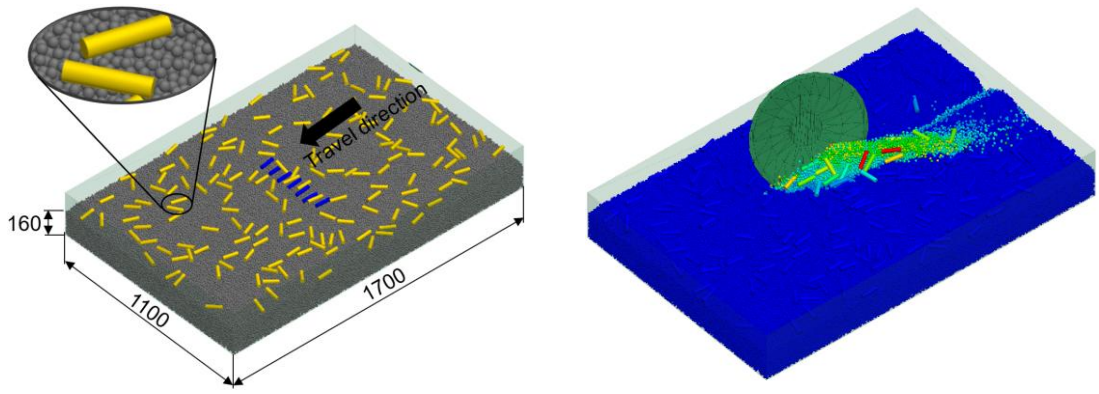

(a) (b)

Figure 3.3. The residue-disc-soil interaction model: (a) the soil particle assembly and corn residue segments on the soil surface; (b) the disc running through soil. The dimensions are in mm.

3.3.3.2 Calibration and Validation of the Model

Parameters in PFC^{3D} were required to be assigned to model elements: soil particles, residue segments, disc, and the contacts between them. Among the required parameters, soil particle stiffness (K_s) and stiffness of soil-residue interface (K_{rs}) were found having significant influences on the interaction between soil and residue (Adajar et al., 2021; Sadek and Chen, 2015). Therefore, two parameters (K_s and K_{rs}) were calibrated. All other parameters were adopted from the studies by Zeng et al. (2020) and Adajar et al. (2021) who modelled the interaction of corn residue with soil that was the same as that used in this study. All parameters are summarized in Table 3.1. The other parameters required for the model were the stiffness and friction of disc and soil bin, and the corresponding values were assumed to be 1×10^8 N m^{-1} and 0.5 respectively, which were common values (Zeng et al., 2017).

Table 3.1. Model parameters of soil, residue, and their contacts.

Parameters	Value	Source
Soil particle normal stiffness (N m^{-1})	To be calibrated	
Soil particle shear stiffness (N m^{-1})	= soil particle normal stiffness	
Soil particle friction coefficient	0.36	(Zeng et al., 2020)
Soil particle density (kg m^{-3})	2650	(Zeng et al., 2020)
Soil particle local damping ratio	0.1	(Zeng et al., 2020)
Soil normal critical damping coefficient	0.0	(Zeng et al., 2020)
Soil shear critical damping coefficient	0.0	(Zeng et al., 2020)
Soil bond radius multiplier	0.5	(Zeng et al., 2020)
Soil bond normal stiffness (Pa m^{-1})	4.95e7	(Zeng et al., 2020)
Soil bond shear stiffness (Pa m^{-1})	4.95e7	(Zeng et al., 2020)
Soil bond tensile strength (Pa)	3.82e4	(Zeng et al., 2020)
Soil bond cohesion (Pa)	1.39e4	(Zeng et al., 2020)
Residue local damping ratio	0.5	(Zeng et al., 2020)
Residue – residue normal stiffness (N m^{-1})	5e4	(Adajar et al., 2021)
Residue – residue shear stiffness (N m^{-1})	5e4	(Adajar et al., 2021)
Residue – residue friction	0.05	(Adajar et al., 2021)
Residue – soil normal stiffness (N m^{-1})	To be calibrated	
Residue – soil shear stiffness (N m^{-1})	= half of residue-soil normal stiffness	
Residue – soil friction	0.05	(Adajar et al., 2021)
Residue density (kg m^{-3})	178.3	Determined

The residue-disc-soil model was run for model calibration and validation with the following disc operational parameters: tilt angle (α) of 20°, disc angle (β) of 17°, working depth of 80 mm, and travelling speed of 8 km h^{-1} which were the same as those in the soil bin test. The time of each simulation was approximately 20 hours using a Dell Workstation with 192 GB RAM, a 2.10 GHz

Intel (R), and Xeon (R) Silver 4110 CPU (2 processors). The default timestep (approximately 2e-6 s) that was automatically calculated was used throughout simulations.

For model calibration, experimental data of the medium residue segment length (*L125*) was used. The model outputs of draft force (F_D) and residue incorporation rate (R_I) were compared with experiment results. The values of K_s and K_{rs} were adjusted until the simulation results matched the experiment results. For model validation, experimental data of the short and long residue segment lengths (*L75* and *L200*) were used. The model outputs, including F_D, F_L, F_V, R_I, and residue displacements were compared with the corresponding experiment results. The discrepancies between the simulations and the measurements were evaluated as follows:

$$RE = \frac{1}{N}\sum_{i=1}^{N}\left(\frac{|M_i - S_i|}{M_i}\right) \times 100\% \qquad (3.1)$$

where RE = relative error between the measured and simulated values, M = measured values, S = simulated values, N = number of evaluation indicators, and i = i-th of the indicator.

3.3.3.3 Model Application

The validated model was applied to investigate the effects of disc angle and tilt angle on soil and residue dynamic attributes. The short residue segment length (*L75*) was used in this application. To examine effects of α, the value of α was varied while the β remained constant. Similarly, the α remained constant to examine the effects of β. Soil cutting forces and residue incorporation rates were monitored in these simulations.

The model was also applied to investigate the combined effects of α and β, and to determine the optimal combination of α and β that resulted in the minimum F_D for improving the energy-efficiency and maximum R_I for enhancing residue decomposition in soil. For this application, five

values of α and β from 5° to 25° at an interval of 5° were chosen as control factors (Table 3.2). The orthogonal design of simulation was used to select the value groups of two angles.

Table 3.2*. Factors and levels of orthogonal design.

Level code	Control factors of disc parameters	
	α (°)	β (°)
-1	5	5
-0.5	10	10
0	15	15
0.5	20	20
1	25	25

* α = tilt angle and β = disc angle.

3.4. Results and Discussion

3.4.1 Experimental Results

3.4.1.1 Measured Residue Incorporation Rate and Soil Cutting Forces

The residue incorporation rate (R_I) resulting from the disc increased with the length of the residue segment. The R_I of the *L200* treatment was 19.9% and 34.3% larger than those of *L125* and *L75* respectively, but no statistical differences were detected due to the high variation of the data (Figure 3.4a). As for the soil cutting forces, the *L200* had draft force (F_D) of 181.3 N, which was significantly higher than that of *L75* (Figure 3.4b). The reason for the increasing trend in F_D was considered to be the blockage effect of residue on the tillage path of the disc; the longer the residue, the more blocking action the residue had. A similar increasing trend was found for the vertical force (F_V) (Figure 3.4c). The F_V of the *L200* was 43.3% and 28.1% larger than that of *L75*

and *L125*. However, the trend was not statistically significant. There were no significant differences in F_L between three residue lengths (Figure 3.4d).

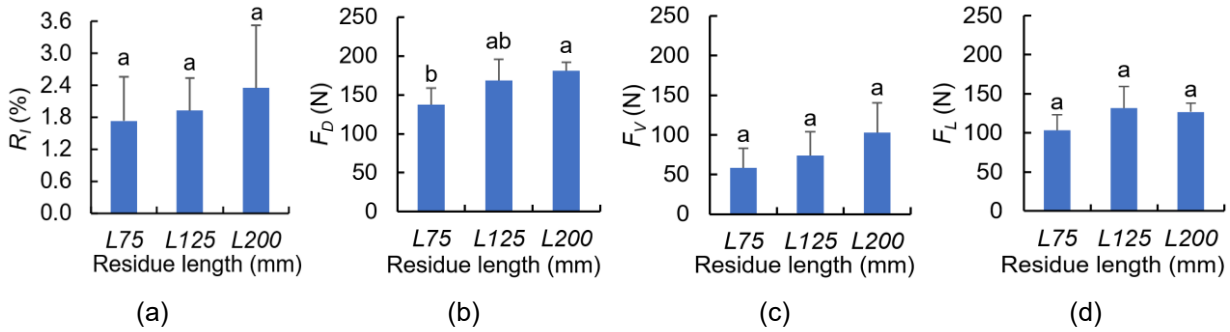

Figure 3.4. Experiment results at different residue lengths (*L75* = 75 mm, *L125* = 125 mm, *L200* = 200 mm) for: (a) residue incorporation rate (R_I); (b) draft force (F_D); (c) vertical force (F_V); and (d) lateral force (F_L); means followed by different letters represent significantly different among different residue lengths, according to Duncan's multiple range test at the significance level of 0.05; error bars are standard deviations.

3.4.1.2 Measured Residue Displacements

The residue displacements in three directions had both differences and similarities. Here the effects of residue length and distance relative to the disc were demonstrated in the same graphs. For all forward, lateral, and vertical directions, much larger displacements were observed at 0 to 120 mm away from the disc as compared with the distances further away from the disc (180 – 360 mm) (Figure 3.5). As for the effect of residue length, the forward displacement of residue appeared to be smaller for the *L125* treatment than the *L75* and *L200* within the distance of 0 to 120 mm (Figure 3.5a). In contrary, the lateral displacement appeared to be larger for the *L125* treatment than the *L75* and *L200* treatments within the distance of 0 to 240 mm (Figure 3.5b). Whereas no particular trend was found in this regard for the vertical displacement (Figure 3.5c). However, in all cases, residue length at a given distance from the disc did not significantly affect the residue displacement in any direction.

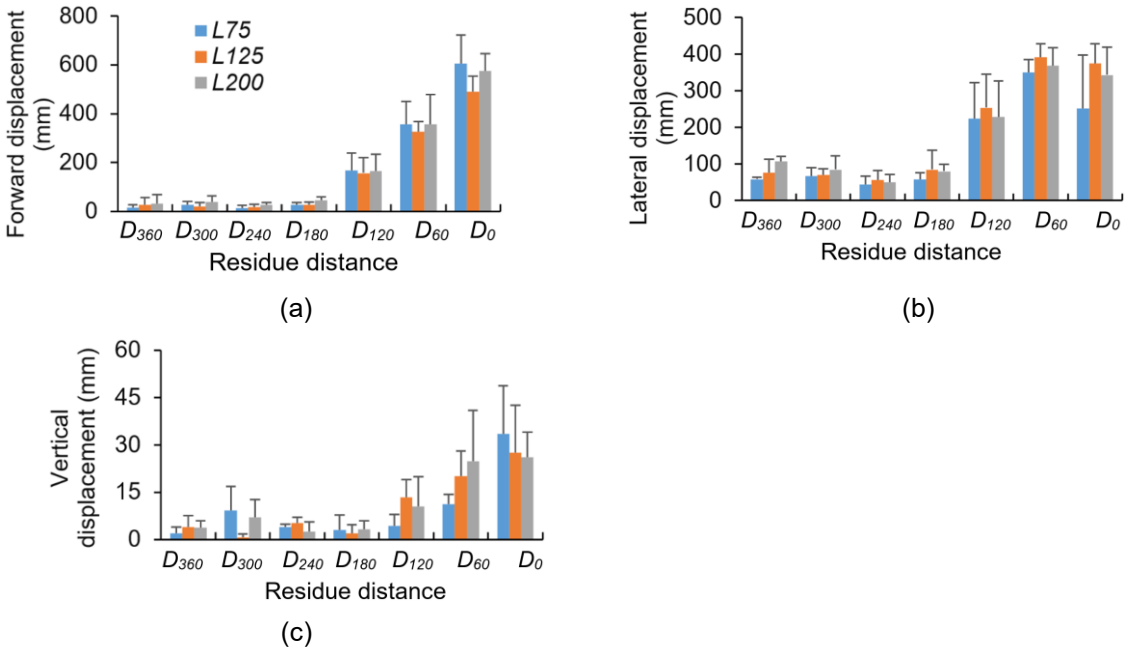

Figure 3.5. Experiment results: (a) forward; (b) lateral; and (c) vertical displacement of three residue lengths (*L75* = 75 mm, *L125* = 125 mm, *L200* = 200 mm) at various distances relative to the disc (D_0 = 0 mm, D_{60} = 60 mm, D_{120} = 120 mm, D_{180} = 180 mm, D_{240} = 240 mm, D_{300} = 300 mm, and D_{360} = 360 mm); error bars are standard deviations.

3.4.2 Calibrated Model Parameters

A total of 25 simulation runs were performed in the calibration. Five values of soil particle stiffness (K_s) for model inputs were 1e4, 5e4, 1e5, 5e5, and 1e6 N m^{-1}, and each of them was combined with five values (9.7e0, 9.7e1, 9.7e2, 9.7e3, and 9.7e4 N m^{-1}) of the stiffness of residue-soil interface (K_{rs}). The draft force (F_D) and residue incorporation rate (R_I) were monitored. Results of response surface showed that F_D increased as the K_s increased, but no noticeable change was found as the K_{rs} increased (Figure 3.6a). The R_I was kept steady as the K_s increased, while decreased at an increased K_{rs} (Figure 3.6b). The response surfaces of F_D and R_I can be described by the following polynomial functions:

$$F_D = 79.0574 - 29.6589(lgK_s) - 4.7940(lgK_{rs}) + 0.6003(lgK_s)(lgK_{rs}) + 7.3426(lgK_s)^2 + 0.3907(lgK_{rs})^2 \quad (3.2)$$

$$R_I = -8.3828 + 8.7312(lgK_s) - 4.5713(lgK_{rs}) + 0.0938(lgK_s)(lgK_{rs}) - 1.8534(lgK_s)^2 + 1.3777(lgK_{rs})^2 - 0.0068(lgK_s)^2(lgK_{rs}) - 0.0124(lgK_s)(lgK_{rs})^2 + 0.1294(lgK_s)^3 - 0.1291(lgK_{rs})^3 \quad (3.3)$$

where F_D = draft force (N), R_I = residue incorporation rate (%), K_s = soil particle stiffness (N m^{-1}), and K_{rs} = stiffness of residue-soil interface (N m^{-1}).

The coefficients of determination (R^2) were 0.99 and 0.97 for Eqs. (3.2) and (3.3) respectively, indicating that a high degree of fitting of the regression models. The regression models were used to predict the K_s and K_{rs}. The F_D in Eq. (3.2) was substituted by the value (168.4 N) measured from the experiment under the same residue length and disc operational parameters. Similarly, the R_I in Eq. (3.3) was substituted by the measured value (1.93%). There were multiple solutions that satisfied the regression models. After removing non-realistic solutions, the predicted K_s and K_{rs} were 1.15e6 and 13.5 N m^{-1} respectively. The predicted K_s and K_{rs} were assigned to the calibration model to verify the prediction accuracy of the regression models (Eqs. 3.2 and 3.3). The overall relative error of F_D and R_I that yielded by the predicted K_s and K_{rs} was 2.5%. This set of parameters (K_s = 1.15e6 N m^{-1}, K_{rs} = 13.5 N m^{-1}) were therefore used throughout the following simulations.

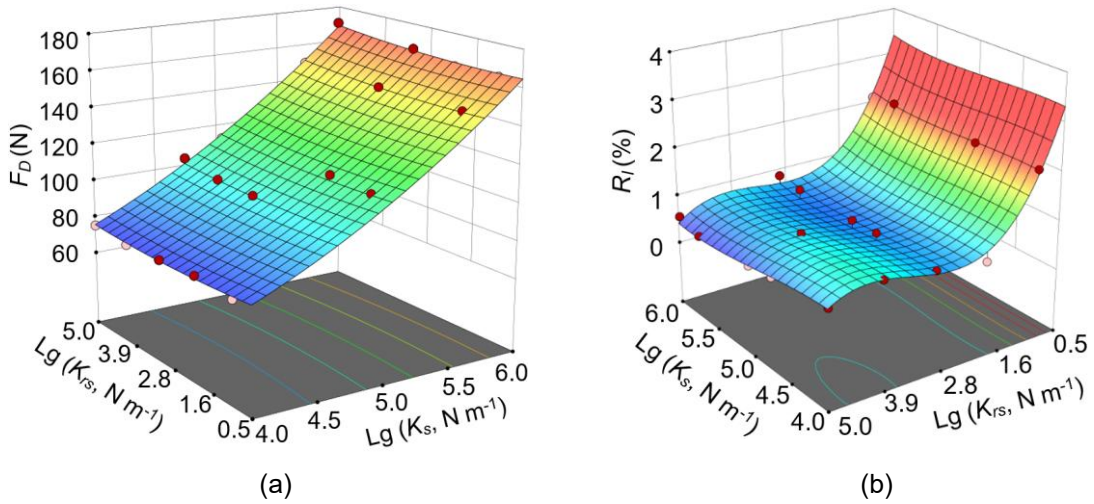

(a) (b)

Figure 3.6. Response surface: (a) draft force (F_D); (b) residue incorporation rate (R_I) with respect to soil particle stiffness (K_s) and stiffness of soil-residue interface (K_{rs}) on a base 10 logarithm scale. Residue length = 125 mm; disc operational parameters: tilt angle (α) = 20°, disc angle (β) = 17°, working depth = 80 mm, travelling speed = 8 km h^{-1}.

3.4.3 Model Validation Results

Using the calibrated parameters, the model prediction accuracy was evaluated against the experimental values for treatments of *L75* and *L200* (Table 3.3). The results showed that this residue-disc-soil interaction model had average *RE* of 9.0% and 18.2% as compared with the experimental measurements of the R_I and F_D respectively. This model was therefore reasonably accurate to predict the R_I and F_D. For F_L and F_V, the model had an average *RE* of 82.1% and 37.5% respectively. Thus, the model had less accuracy in predicting F_L and F_V.

Table 3.3*. Summary of the relative errors (%) between the experiment and simulation; disc operational parameters: tilt angle (α) = 20°, disc angle (β) = 17°, working depth = 80 mm, travelling speed = 8 km h^{-1}.

Treatment	*RE* (%)			
	R_I	F_D	F_L	F_V
L75	2.3	7.4	100.9	21.5
L200	15.7	28.9	63.2	53.4
Average	9.0	18.2	82.1	37.5

* R_I = residue incorporation rate, F_D = draft force, F_L = lateral force, F_V = vertical force, *RE* = relative errors, *L75* = residue length of 75 mm, and *L200* = residue length of 200 mm.

The relative errors of the predicted residue displacements varied, depending on the distance of the residue relative to disc. Overall, the model underpredicted the residue displacements. However, there were similarities in the trends between simulation and experiment results. In both experiment and model simulation, the displacement was continuously decreasing within the distance of 0 to 180 mm (from D_0 to D_{180}), and the displacement was kept generally constant from 180 to 360 mm (from D_{180} to D_{360}) (Figure 3.7). The trends of forward displacement (Figure 3.7a) and those of lateral displacement (Figure 3.7b) could be described with an exponential function with high coefficients of determination (R^2). A similar exponential trend but lower R^2 was found for the predicted vertical displacements, but the predicted exponential curve was close to the experiment curve (Figure 3.7c).

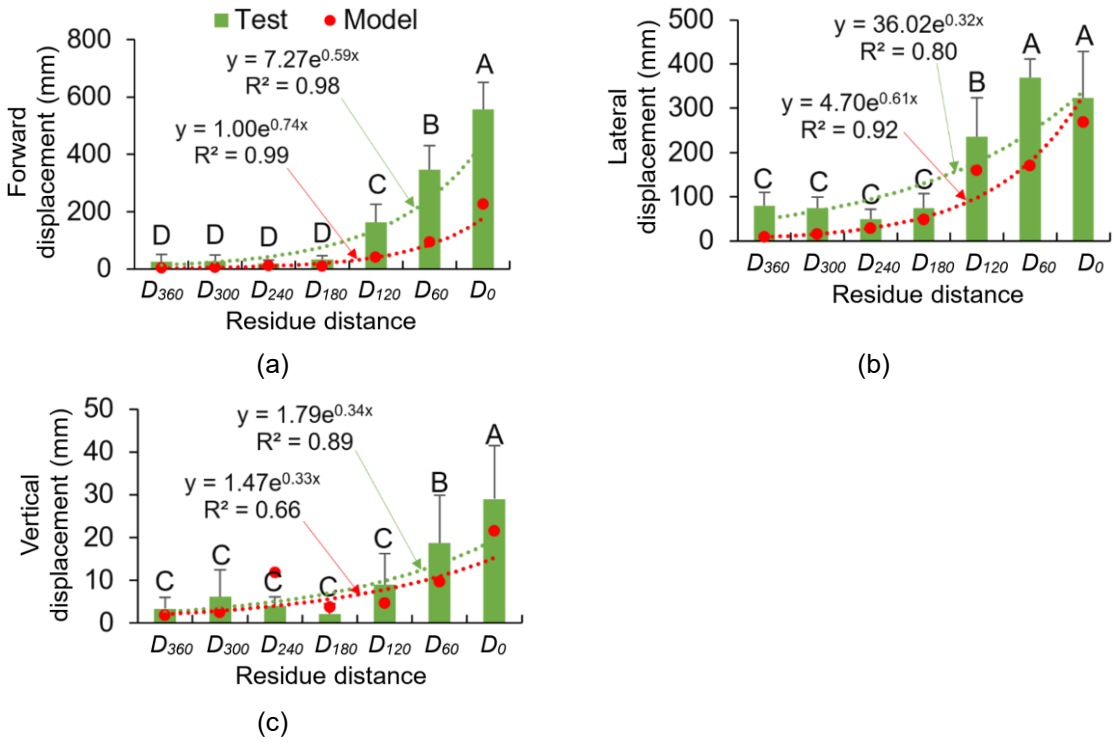

Figure 3.7. Measurements and simulations of average values of two treatments (i.e., residue lengths of 200 and 75 mm): (a) forward; (b) lateral; and (c) vertical displacement at various distances relative to disc (D_0 = 0 mm, D_{60} = 60 mm, D_{120} = 120 mm, D_{180} = 180 mm, D_{240} = 240 mm, D_{300} = 300 mm, and D_{360} = 360 mm); means followed by different letters represent significantly different among various distances, according to Duncan's multiple range test at the significance level of 0.05; error bars are standard deviations.

3.4.4 Simulated Soil and Residue Dynamics at Various Angles of Disc

3.4.4.1 Effects of Tilt and Disc Angles on the Draft Force and Residue Incorporation Rate

With the increasing of tilt angle (α) from 10° to 30°, the F_D had a decreasing linear trend (Figure 3.8a). However, the F_D showed an increasing exponential trend with the increasing of disc angle (β) from 10° to 30° (Figure 3.8b). The coefficients of determination (R^2) were all over 0.99. The experimental results in existing literatures (Damanauskas et al., 2019; Kogut et al., 2016; Malasli and Celik, 2019) also found this similar trend, proving the reliability of DEM simulation. The

simulations in Sadek et al. (2021) did not involve residues, but they obtained similar conclusions, implying that the presence of residue may not significantly change the effect of α and β on F_D.

The R_I decreased linearly from 1.96% to 1.33% as the α increased from 10° to 30° (Figure 3.8c). The reason for this observation was that the F_D decreased as the α increased, resulting in fewer soil particles being pushed and thereby less soil particles being mixed into residue. However, the R_I increased as the β increased, which followed a logarithmic trend (Figure 3.8d). The possible reason was that a higher β caused a larger F_D, and then, more soil particles were rolled up and mixed with residue.

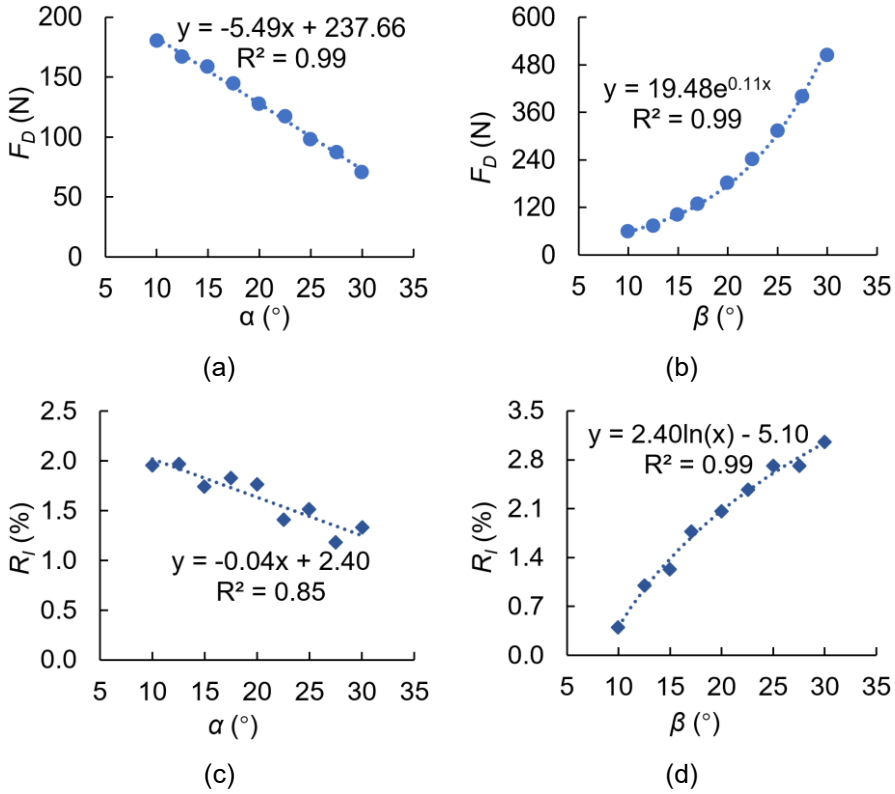

Figure 3.8. Model results on the effects of angles (α = tilt angle, β = disc angle) on response indicators (F_D = draft force, R_I = residue incorporation rate): (a) F_D vs. α; (b) F_D vs. β; (c) R_I vs. α; and (d) R_I vs. β; disc operational parameters: working depth = 80 mm, travelling speed = 8 km h^{-1}; residue length = 75 mm.

3.4.4.2 Optimization of Tilt and Disc Angle

Results from the simulation run groups based on orthogonal design are shown in Table 3.4. The combined effect of α and β on response indicators (F_D and R_I) was fitted to polynomial regression analysis equations, which are shown as:

$$F_D = 48.22 + 3.76\alpha - 3.91\beta - 0.41\alpha\beta - 0.09\alpha^2 + 0.85\beta^2 \quad (3.4)$$

$$R_I = -0.19 - 0.02\alpha + 0.12\beta \quad (3.5)$$

where F_D = draft force (N), R_I = residue incorporation rate (%), α = tilt angle (°), and β = disc angle (°).

Table 3.4*. Orthogonal design and results of simulations; disc operational parameters: working depth = 80 mm, travelling speed = 8 km h^{-1}, residue length = 75 mm.

No.	α (°)	β (°)	F_D (N)	R_I (%)
1	20	20	181.2	2.07
2	20	10	58.8	0.40
3	10	25	412.6	2.62
4	5	10	94.7	0.72
5	25	25	261.3	2.30
6	15	5	50.8	0.16
7	10	5	57.8	0.22
8	25	5	32.7	0.07
9	5	15	162.9	1.82
10	15	15	123.2	1.36
11	10	20	253.1	2.18

* R_I = residue incorporation rate, F_D = draft force, α = tilt angle, and β = disc angle.

The results obtained from the variance analysis of simulation results are listed in Table 3.5, which concludes the combined effect of the α and β. It can be seen that α, β, $\alpha\beta$, and β^2 had a significant influence on F_D, meaning that the factors affected F_D were disc angle, tilt angle, and the interaction of disc and tilt angles. The P value of β^2 was smaller than that of α^2, indicating that disc angle had more significant influence on F_D than tilt angle. For R_I, the interaction of disc and tilt angles had no significant influence, due to the P value of $\alpha\beta$ being larger than 0.05. Compared with the tilt angle, the disc angle had a larger impact on R_I.

In applications of tillage, minimum draft force is desired for a reduced tractor power requirement. As for corn residue incorporation by discs, higher incorporation rate is considered better to avoid the interference of corn residue with the subsequent seeding operation. Therefore, maximum residue incorporation rate was desired in this study. For the optimization, the dependent variables were F_D and R_I, and the objectives and constraint range (CR) of the angles are shown as:

$$\begin{cases} min(F_D) \\ max(R_I) \\ CR. \\ 5 \le \alpha \le 25, \\ 5 \le \beta \le 25 \end{cases} \quad (3.6)$$

where F_D = draft force (N), R_I = residue incorporation rate (%), α = tilt angle (°), and β = disc angle (°).

The Eqs. (3.4) and (3.5) were the objective functions, and they were imported into MATLAB to optimize the α and β under the constraint. The results showed the optimal values for α and β were 20° and 25° respectively, which gave a minimum F_D of 136.7 N and a maximum R_I of 1.72% simultaneously within the angle range of 5° to 25°.

Table 3.5*. Simulation results and ANOVA of regression equations.

Sources of variance	F_D (N)		R_I (%)	
	df	*P* value	*df*	*P* value
Model	5	<0.0001	2	<0.0001
α	1	<0.0001	1	0.04
β	1	<0.0001	1	<0.0001
$\alpha\beta$	1	<0.0001		0.45
α^2	1	0.0906		
β^2	1	<0.0001		
Residual	5		8	
Sum	10		10	

* F_D = draft force, R_I = residue incorporation rate, *df* = degree of freedom, α = tilt angle, β = disc angle, and $P < 0.05$ (significant).

3.4.5 Simulated Residue and Soil Particle Behaviours

3.4.5.1 Trajectories and Disturbed Condition of Residue

The simulated residue trajectories of the treatments of *L75* and *L200* had similar behaviours. Therefore, the average trajectory of two treatments was used to analyse the instantaneous dynamic attributes. The simulated trajectory of each of the seven residue tracers were plotted against the disc travelling distance from the original location of tracers (Figure 3.9).

As the disc travelled closer to the residues, the residue at D_0 was moved first. Residue at seven distances relative to disc had different trajectories in all three directions. The forward and lateral trajectories showed that each of the residue continuously moved away from the original position as the disc travelled (Figure 3.9a and 3.9b). The trajectories could be described as exponential plateau curves. The vertical trajectories had totally different trends (Figure 3.9c). Residues moved

in bell-shaped curves in the vertical direction, where 22.2, 15.3, and 1.2 mm respectively above original soil surface. This indicated that the residues dropped on a new soil surface lifted by disc. The steady-states of D_{180} and D_{240} were below the original soil surface, implying that residue were buried into the soil. The D_{300} and D_{360} experienced almost no vertical disturbance by the disc (Figure 3.9c).

The steady-state of tracer trajectories demonstrated three distinct residue disturbed zones, namely “tossed zone”, “buried zone”, and “perturbed zone”, corresponding to the distances of 0 – 120 mm, 120 – 240 mm, and 240 – 360 mm relative to the disc respectively (Figure 3.9d). In the “tossed zone”, corn residue was pushed away by the disc and eventually drop back to the soil surface in the “buried zone” or further. Therefore, there was almost no residue. The residue in the “buried zone” was covered by the soil thrown up by disc, causing the negative steady-state of tracer vertical movement in this zone. The soil particles thrown up by the disc were scattered to the “perturbed zone”, forcing the residue to move slightly. In practice, multiple discs were assembled to form a disc harrow. Based on the phenomenon of three distinct residue disturbed zones, the lateral adjacent disc should be positioned within the buried zone (i.e., disc spacing of 120 to 240 mm), to ensure uniform crop residue disturbance across the harrow width.

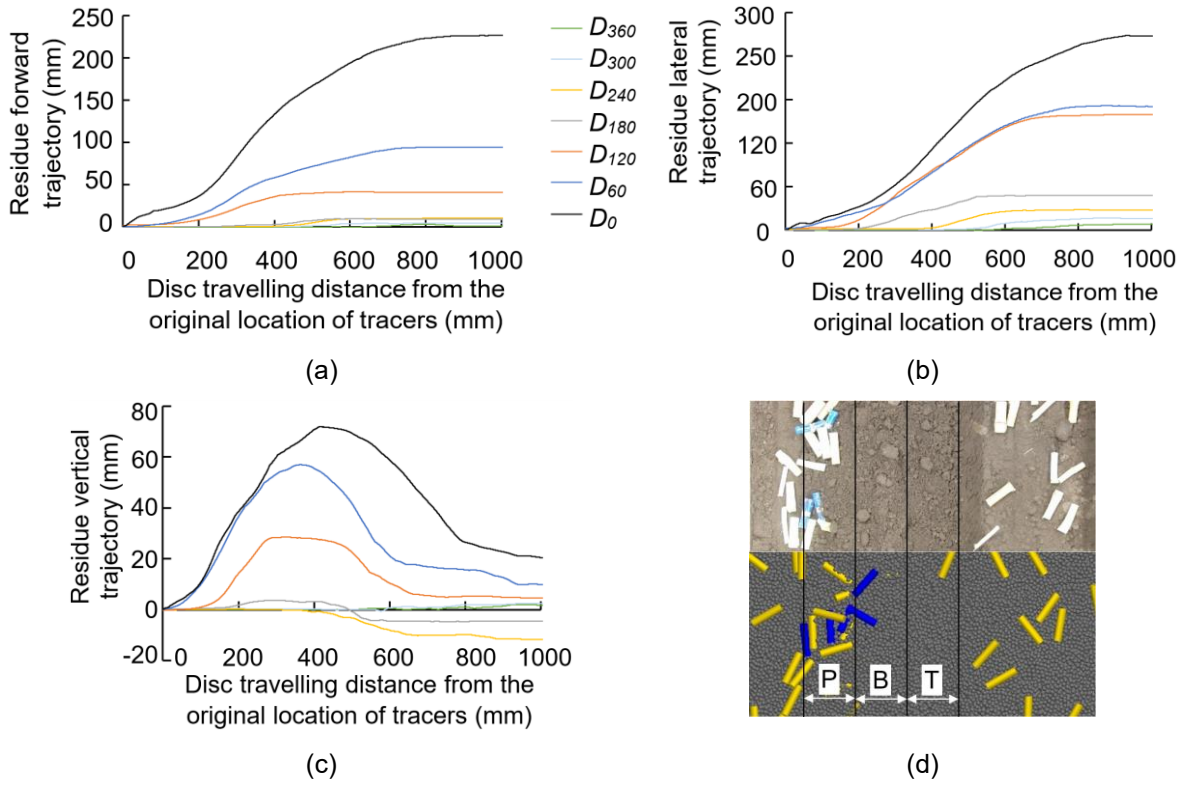

Figure 3.9. Residue displacement: (a) forward trajectories; (b) lateral trajectories; and (c) vertical trajectories of seven distances of residue (D_0, D_{60}, D_{120}, D_{180}, D_{240}, D_{300}, and D_{360} represent the distance of 0, 60, 120, 180, 240, 300, and 360 mm relative to the disc respectively) as the disc travelled far away from the original location of residue tracers; and (d) residue disturbed conditions in different zones (*T* = "tossed zone", *B* = "buried zone", *P* = "perturbed zone"). Disc operational parameters: tilt angle (α) = 20°, disc angle (β) = 17°, working depth = 80 mm, travelling speed = 8 km h^{-1}. Each data point was the average of *L75* and *L200* treatments.

3.4.5.2 Velocity Flow Distribution of Soil and Residue Particles

Velocity distribution of soil and residue particles were observed visually. The velocity of residue was represented by an arrow beam, and soil particles were merely coloured to indicate the magnitude of velocity (Figure 3.10). The particles of soil and residue affected by the disc were observed to move in a peculiar manner in the residue-disc-soil interaction model. This peculiar flow behaviour could be characterized by two distinct regions: lifting and side throwing regions.

The particles in “lifting region” flowed upwards at low velocities. This was possible due to the contact force generated by the raised outer edge of disc, pushing the particles of soil and residue upward. The phenomenon of lifting corresponds to the linear vertical stress distribution assumed by Ahmadi (2018). As the disc continued to move, the lifted particles were thrown sideways by the tilted disc to form the “side throwing region”. In this region, particles moved towards the normal direction of disc surface. The velocity of both residue and soil particles reached a maximum value. The disc functioned similarly to a mouldboard plow in this region, where some of the side thrown soil was inverted, burying the residue (Ucgul et al., 2017).

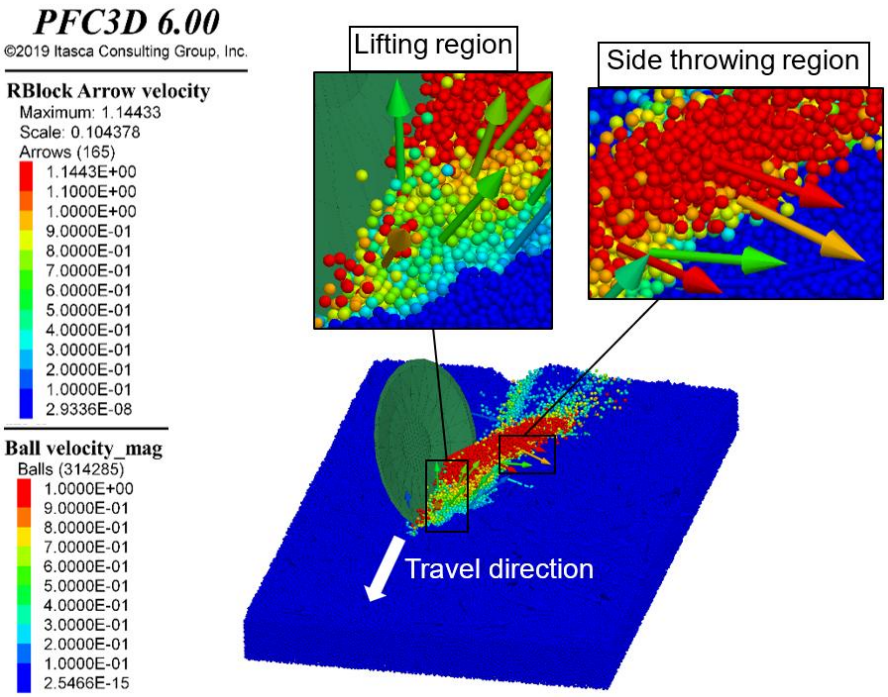

Figure 3.10. Velocity (unit: m s^{-1}) flow distribution of soil (Ball) and residue (RBlock Arrow) particles during the passage of disc. Residue length = 125 mm; disc operational parameters: tilt angle (α) = 20°, disc angle (β) = 17°, working depth = 80 mm, travelling speed = 8 km h^{-1}.

3.5. Conclusions

A DEM model was developed to simulate dynamic attributes of corn residue and soil resulting from a disc. The model was calibrated and validated using measurements from a laboratory experiment. The following conclusions were drawn. Model parameters calibrated were 1.15×10^6 N m^{-1} for stiffness of soil particle and 13.5 N m^{-1} for stiffness of soil-residue interface. The calibrated model had an average relative error of 9.0% for predicting residue incorporation rate and 18.2% for predicting draft force, as compared with the experimental measurements. The simulation results showed that:

1. The model was less accurate in predicting residue displacements.

2. The models allowed for varying disc parameters, such as tilt and disc angles. The simulated disc draft force and residue incorporation rate decreased linearly as the tilt angle increased, whereas increased non-linearly as the disc angle increased. The changes in draft force and residue incorporation were more sensitive to the change in disc angle than that in tilt angle. The optimal tilt and disc angle were 20° and 25° respectively for a minimum draft force and a maximum residue incorporation rate.

3. The model made it possible for tracing the trajectories of residue as the disc was traveling in soil. The traced trajectories of residue featured exponential plateau curves in the forward and lateral directions, and bell-shaped curves in the vertical direction. Results from this study have advanced the understanding of corn residue-disc-soil dynamics and effects of operation parameters of disc on its working performance.

The limitations of this study include the use of only stalk part of corn residue and the certain orientation of residue tracers for residue displacement measurements. Caution should be taken

when extending the results, particularly to other types of crop residue. Other limitations are the assumption of soil particles as uniform 10 mm spheres and corn residue segments as unbreakable rigid blocks in the model. Further research on model development is needed to better represent the real-life characteristics of soil and residue.

3.6. Acknowledgements

This work was financially supported by China Scholarship Council (grant number: 202007565032) and Natural Sciences and Engineering Research Council of Canada (grant number: RGPIN-2019-05861).

3.7. References

Adajar, J. B., Alfaro, M., Chen, Y., and Zeng, Z., 2021. Calibration of discrete element parameters of crop residues and their interfaces with soil. Computers and Electronics in Agriculture, 188, e106349. https://doi.org/10.1016/j.compag.2021.106349

Ahmad, F., Weimin, D., Qishuo, D., Hussain, M., and Jabran, K., 2015. Forces and straw cutting performance of double disc furrow opener in no-till paddy soil. PLoS ONE, 10(3), e0119648. https://doi.org/10.1371/journal.pone.0119648

Ahmad, F., Qiu, B., Ding, Q., Ding, W., Zahid, M.K., Muhammad, S., Farman, A.C., Abdur, R., and Abdul, K., 2020. Discrete element method simulation of disc type furrow openers in paddy soil. International journal of agricultural and biological engineering, 13(4), 103–110. https://doi.org/10.25165/j.ijabe.20201304.4800

Ahmadi, I., 2018. A draught force estimator for disc harrow using the laws of classical soil mechanics. Biosystems Engineering, 171, 52–62. https://doi.org/10.1016/j.biosystemseng.2018.04.008

Arvidsson, J., and Hillerström, O., 2010. Specific draught, soil fragmentation and straw incorporation for different tine and share types. Soil and Tillage Research, 110(1), 154–160. https://doi.org/10.1016/j.still.2010.07.003

ASABE Standards, 2020. ASABE Standard S633: Testing protocol for landscape irrigation soil moisture-based control technologies. American Society of Agricultural and Biological Engineers, St. Joseph, MI.

ASTM Standards, 2016. D4959 Standard test method for determination of water content of soil by direct heating. ASTM International, West Conshohocken, PA. https://doi.org/10.1520/D4959-16

Celik, A., and Altikat, S., 2022. The effect of power harrow on the wheat residue cover and residue incorporation into the tilled soil layer. Soil and Tillage Research, 215, e105202. https://doi.org/10.1016/j.still.2021.105202

Chen, G., Wang, Q., Li, H., He, J., Wang, X., Zhang, X., and He, D., 2024. Experimental research on vertical straw cleaning and soil tillage device based on Soil-Straw composite model. Computers and Electronics in Agriculture, 216, e108510. https://doi.org/10.1016/j.compag.2023.108510

Damanauskas, V., Velykis, A., and Satkus, A., 2019. Efficiency of disc harrow adjustment for stubble tillage quality and fuel consumption. Soil and Tillage Research, 194, e104311. https://doi.org/10.1016/j.still.2019.104311

Fang, H., Zhang, Q., Chandio, F. A., Guo, J., Sattar, A., Arslan, C., and Ji, C., 2016. Effect of straw length and rotavator kinematic parameter on soil and straw movement by a rotary blade. Engineering in Agriculture, Environment and Food, 9(3), 235–241. https://doi.org/10.1016/j.eaef.2016.01.001

Hanajima, D., 2020. Collection of ear corn residue and its utilization as a bulking agent for cow manure composting. Animal Science Journal, 91(1), e13323. https://doi.org/10.1111/asj.13323

Hobbs, P. R., Sayre, K., and Gupta, R., 2008. The role of conservation agriculture in sustainable agriculture. Philosophical Transactions of the Royal Society of London. Series B. Biological Sciences, 363(1491), 543–555. https://doi.org/10.1098/rstb.2007.2169

Khosravani, A., Desbiolles, J. M. A., Saunders, C., Ucgul, M., and Fielke, J. M., 2023. Prediction of single disc seeding system forces, using a semi-analytical and discrete element method (DEM) considering rotation effects. Agriculture (Switzerland), 13(1), e0202. https://doi.org/10.3390/agriculture13010202

Kogut, Z., Sergiel, L., and Żurek, G., 2016. The effect of the disc setup angles and working depth on disc harrow working resistance. Biosystems Engineering, 151, 328–337. https://doi.org/10.1016/j.biosystemseng.2016.10.004

Kumar, N., Sawant, C. P., Sharma, R. K., Chhokar, R. S., Tiwari, P. S., Singh, D., Roul, A. K., Tripathi, S. C., Gill, S. C., and Singh, G. P., 2021. Combined effect of disc coulters and operational speeds on soil disturbance and crop residue cutting under no-tillage system in soil bin. Journal of Scientific and Industrial Research (New Delhi, India: 1963), 80(9), 739–749. https://doi.org/10.56042/jsir.v80i09.40333

Lal, R., Reicosky, D. C., and Hanson, J. D., 2007. Evolution of the plow over 10,000 years and the rationale for no-till farming. Soil and Tillage Research, 93(1), 1–12. https://doi.org/10.1016/j.still.2006.11.004

Li, W., Zhang, F., Luo, Z., Zheng, E., Pan, D., Qian, J., Yao, H., and Wang, X., 2024. Straw movement and flow field in a crushing device based on CFD-DEM coupling with flexible hollow straw model. Biosystems Engineering, 242, 140–153. https://doi.org/10.1016/j.biosystemseng.2024.04.018

Li, R., Zheng, J., Xie, R., Ming, B., Peng, X., Luo, Y., Zheng, H., Sui, P., Wang, K., Hou, P., Hou, L., Zhang, G., Bai, S., Wang, H., Liu, W., and Li, S., 2022. Potential mechanisms of maize yield reduction under short-term no-tillage combined with residue coverage in the semi-humid region of Northeast China. Soil and Tillage Research, 217, e105289. https://doi.org/10.1016/j.still.2021.105289

Liu, J., Chen, Y., and Kushwaha, R. L., 2010. Effect of tillage speed and straw length on soil and straw movement by a sweep. Soil and Tillage Research, 109(1), 9–17. https://doi.org/10.1016/j.still.2010.03.014

Liu, L., Wang, X., Zhang, X., Cheng, X., Wei, Z., Zhou, H., and Zhao, K., 2023. The impact of ‘T’-shaped furrow opener of no-tillage seeder on straw and soil based on discrete element method. Computers and Electronics in Agriculture, 213, e108278. https://doi.org/10.1016/j.compag.2023.108278

Malasli, M. Z., and Celik, A., 2019. Disc angle and tilt angle effects on forces acting on a single-disc type no-till seeder opener. Soil and Tillage Research, 194, e104304. https://doi.org/10.1016/j.still.2019.104304

Murray, S. E., and Chen, Y., 2018. Soil bin tests and discrete element modeling of a disc opener. Canadian Biosystems Engineering, 60(1), 2.1–2.10. https://doi.org/10.7451/CBE.2018.60.2.1

Potyondy, D. O., and Cundall, P. A., 2004. A bonded-particle model for rock. International Journal of Rock Mechanics and Mining Sciences (Oxford, England: 1997), 41(8), 1329–1364. https://doi.org/10.1016/j.ijrmms.2004.09.011

Sadek, M. A., and Chen, Y., 2015. Feasibility of using PFC3D to simulate soil flow resulting from a simple soil-engaging tool. Transactions of the ASABE, 58(4), 987–996. https://doi.org/10.13031/trans.58.10900

Sadek, M. A., Chen, Y., and Zeng, Z., 2021. Draft force prediction for a high-speed disc implement using discrete element modelling. Biosystems Engineering, 202, 133–141. https://doi.org/10.1016/j.biosystemseng.2020.12.009

Saunders, C., Ucgul, M., and Godwin, R. J., 2021. Discrete element method (DEM) simulation to improve performance of a mouldboard skimmer. Soil and Tillage Research, 205, e104764. https://doi.org/10.1016/j.still.2020.104764

Shinners, K. J., and Binversie, B. N., 2007. Fractional yield and moisture of corn stover biomass produced in the Northern US Corn Belt. Biomass and Bioenergy, 31(8), 576–584. https://doi.org/10.1016/j.biombioe.2007.02.002

Tekeste, M. Z., Balvanz, L. R., Hatfield, J. L., and Ghorbani, S., 2019. Discrete element modeling of cultivator sweep-to-soil interaction: Worn and hardened edges effects on soil-tool forces and soil flow. Journal of Terramechanics, 82, 1–11. https://doi.org/10.1016/j.jterra.2018.11.001

Torotwa, I., Ding, Q., Makange, N. R., Liang, L., and He, R., 2021. Performance evaluation of a biomimetically designed disc for dense-straw mulched conservation tillage. Soil and Tillage Research, 212, e105068. https://doi.org/10.1016/j.still.2021.105068

Ucgul, M., 2023. Simulating soil–disc plough interaction using discrete element method–multi-body dynamic coupling. Agriculture (Switzerland), 13(2), e0305. https://doi.org/10.3390/agriculture13020305

Ucgul, M., Saunders, C., and Fielke, J. M., 2017. Discrete element modelling of topsoil burial using a full scale mouldboard plough under field conditions. Biosystems Engineering, 160, 140–153. https://doi.org/10.1016/j.biosystemseng.2017.06.008

Wang, Q., Zhu, L., Li, M., Huang, D., and Jia, H., 2018. Conservation agriculture using coulters: Effects of crop residue on working performance. Sustainability (Switzerland), 10(11), e4099. https://doi.org/10.3390/su10114099

Wang, X., Wei, W., He, J., and Huang, Y., 2021. Effect of soil particle-size distribution (PSD) on soil-subsoiler interactions in the discrete element model. Spanish Journal of Agricultural Research: SJAR, 19(1), e0205. https://doi.org/10.5424/sjar/2021191-16584

Wang, Y., Xue, W., Ma, Y., Tong, J., Liu, X., and Sun, J., 2019. DEM and soil bin study on a biomimetic disc furrow opener. Computers and Electronics in Agriculture, 156, 209–216. https://doi.org/10.1016/j.compag.2018.11.023

Xu, G., Xie, Y., Liang, L., Ding, Q., Xie, H., and Wang, J., 2022a. Straw-soil-rotary blade interaction: Interactive effects of multiple operation parameters on the straw movement. Agronomy (Switzerland), 12(4), e0847. https://doi.org/10.3390/agronomy12040847

Xu, G., Xie, Y., Matin, M.A., He, R., and Ding, Q., 2022b. Effect of straw length, stubble height and rotary speed on residue incorporation by rotary tillage in intensive rice–wheat rotation system. Agriculture (Switzerland), 12(2), e0222. https://doi.org/10.3390/agriculture12020222

Zeng, Z., and Chen, Y., 2019. Simulation of straw movement by discrete element modelling of straw-sweep-soil interaction. Biosystems Engineering, 180, 25–35. https://doi.org/10.1016/j.biosystemseng.2019.01.009

Zeng, Z., Chen, Y., and Zhang, X., 2017. Modelling the interaction of a deep tillage tool with heterogeneous soil. Computers and Electronics in Agriculture, 143, 130–138. https://doi.org/10.1016/j.compag.2017.10.005

Zeng, Z., Ma, X., Chen, Y., and Qi, L., 2020. Modelling residue incorporation of selected chisel ploughing tools using the discrete element method (DEM). Soil and Tillage Research, 197, e104505. https://doi.org/10.1016/j.still.2019.104505

Zeng, Z., Thoms, D., Chen, Y., and Ma, X., 2021. Comparison of soil and corn residue cutting performance of different discs used for vertical tillage. Scientific Reports, 11(1), 2537–2537. https://doi.org/10.1038/s41598-021-82270-9

Zhao, H., Huang, Y., Liu, Z., Liu, W., and Zheng, Z., 2021. Applications of discrete element method in the research of agricultural machinery: A review. Agriculture (Switzerland), 11(5), e0425. https://doi.org/10.3390/agriculture11050425

Zhang, S., Jia, X., Dong, J., Wang, X., Zhao, H., Chen, X., Zhang, Z., Huang, Y., and Shi, J., 2024. Optimization of operating angles of disc coulters for maize residue management

using discrete element method. Computers and Electronics in Agriculture, 218, e108691. https://doi.org/10.1016/j.compag.2024.108691

Zhong, G., Li, H., He, J., Wang, Q., Lu, C., Wang, C., Tong, Z., Cui, D., and He, D., 2023. Design and test of single-disc opener for no-till planter based on support cutting. Agriculture (Switzerland), 13(8), e1635. https://doi.org/10.3390/agriculture13081635

Zhou, H., Zhang, C., Zhang, W., Yang, Q., Li, D., Liu, Z., and Xia, J., 2020. Evaluation of straw spatial distribution after straw incorporation into soil for different tillage tools. Soil and Tillage Research, 196, e104440. https://doi.org/10.1016/j.still.2019.104440

Zhu, D., Shi, M., Yu, C., Yu, Z., Kuang, F., Xiong, W., and Xue, K., 2023. Tool-straw-paddy soil coupling model of mechanical rotary-tillage process based on DEM-FEM. Computers and Electronics in Agriculture, 215, e108410. https://doi.org/10.1016/j.compag.2023.108410

Chapter 4: Simulation of the Micro-Dynamics in Soil–Cornstalk–Disc Interactions Using the Discrete Element Method *

*Published in *Smart Agricultural Technology* 11, e100984.

4.1. Abstract

Understanding the interactions between soil, crop residue, and tillage tools is essential for improving tillage quality in conservation agriculture. This study developed a discrete element model to simulate soil–cornstalk–disc interactions, replicating the cutting of corn stalks by a concave disc in sandy loam soil. A soil bin experiment was conducted using a notched concave disc to cut corn stalks, measuring draft forces, vertical forces, and corn residue cutting effectiveness. Experimental data were used to calibrate and validate the model. After validation, the model was applied to analyse the micro-dynamic behaviours of corn stalks and soil under varying soil bulk densities and disc types. Three key parameters calibrated for the corn stalk model were 2.0×10^9 N m^{-1} for particle normal stiffness, 8.0×10^6 Pa for bond tensile strength, and 0.5 for particle friction coefficient. The model effectively predicted corn stalk cutting effectiveness, draft force, and vertical force, with an overall relative error of 16.4%. Micro-dynamic analysis showed that as soil bulk density decreased (within a range of 1.06 to 1.52 Mg m^{-3}), corn stalk sinkage and soil supporting force increased, while corn stalk intrusion force decreased. Compared to the notched disc, the plain disc exhibited greater corn stalk sinkage and soil supporting force but lower corn stalk intrusion force. This research provides a validated model for simulating soil–cornstalk–disc interactions, enhancing the understanding of disc performance in cutting crop residue.

Keywords: Cutting; DEM; Disc; Micro-dynamics; Corn stalk

4.2. Introduction

Crop residues were retained in agricultural fields where conservation practices were used for controlling soil erosion, improving soil quality, and increasing crop yields (Laborde et al., 2021; Zhang et al., 2015; Wang et al., 2018). However, excessive residue, particularly corn residue, is detrimental to seed germination, plant emergence and growth. To eliminate these adverse effects, concave discs are commonly used for seedbed preparations, as they are effective for cutting residue while maintaining some crop residue on the soil surface for preventing soil erosion (Chen and Li, 2016). Many previous studies had been conducted on disc cutting crop residue as affected by disc types, geometric shapes, dimensions, and operational parameters. For example, among several types of discs, toothed disc coulters performed better in cutting sugar cane crop residue (Bianchini and Magalhães, 2008), while no differences were found among notched, rippled, and plain discs in the effectiveness of cutting corn residue (Zeng et al., 2021) (Figure 4.1). A disc opener having a diameter of 450 mm provided better performance in cutting rice residue than the discs with larger or smaller diameters (Ahmad et al., 2015). Kumar et al. (2021) had investigated the disc operational speeds on residue cutting, showing that within the speed range of 0.56 to 1.11 m s^{-1}, the residue cutting performance did not change significantly. Discs cut rice straw more efficiently when working at a shallower depth ranging from 90 mm to 30 mm (Ahmad et al., 2017).

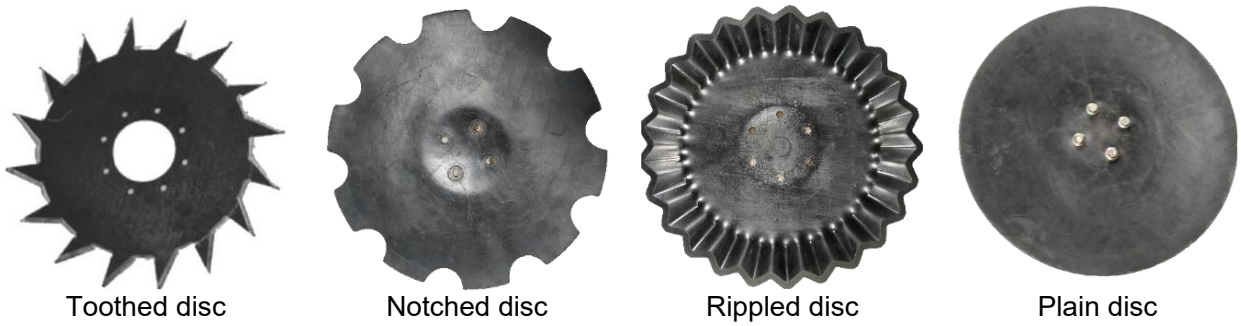

Figure 4.1. The illustration of different types of disc tillage tools, toothed disc referred to Bianchini and Magalhães (2008).

The above existing studies were limited to the residue cutting effectiveness of discs. There was lack of in-depth understanding on the causes resulted in the differences. Soil bulk density has influence on crop residue cutting effectiveness, as reported by Aikins et al. (2020) that a failure of cutting crop residue was sometimes attributed to the low soil strength. However, this inference has not been well documented yet, and most existing studies were on how soil bulk density affected soil cutting forces (Sánchez-Girón et al., 2005; Roul et al., 2009). Few studies were carried out on force analysis of corn stalk cutting using discs. Such force analysis was beneficial to the disc structural design and practical operation (Torotwa et al., 2021; Kumar et al., 2021).

Existing methods for the analysis of forces resulting from disc cutting were categorized as experimental, analytical, and numerical methods. Experimental methods detected the changes in cutting resistance caused by crop residue (Wang et al., 2018; Bianchini and Magalhães, 2008), but failed to identify the instantaneous cutting state of soil and crop residue. Classical mechanics was applied in analysing the instantaneous state of residue cutting by plain disc coulter (Torotwa et al., 2021), notched disc coulter (Kushwaha et al., 1986), and toothed rolling disc coulter (Magalhães et al., 2007). But tool geometries and work conditions were simplified in those analyses. Numerical method, particularly discrete element method (DEM), could examine mechanical attributes of crop

residue cutting without encountering the above limitations. The DEM has been used to simulate bending behaviours of wheat stalk (Schramm and Tekeste, 2022; Schramm et al., 2019) and corn stalk (Liu et al., 2023). However, the micro-dynamic cutting behaviours of corn stalk induced by concave discs in different bulk densities of soil have not been conducted yet.

This study aimed to: (1) develop a DEM model to simulate soil–cornstalk–disc interactions, (2) conduct experiments for model calibration and validation using measured data, and (3) investigate the micro-dynamic behaviours of soil and corn stalks under two different concave discs and varying soil bulk densities.

4.3. Methodology

4.3.1 Description of Disc and Corn Stalk

Two commercial discs: plain disc (Figure 4.2a) and notched disc (Figure 4.2b) were tested. The thickness and diameter of two discs were 6.5 mm and 508 mm respectively. The concave had a radius of 760 mm. The notches of the notched disc had a chord length of 79 mm and a depth of 29 mm in the radial direction. Ten cutting notches were evenly distributed along the circumference.

(a) (b)

Figure 4.2. Two discs studied: (a) plain disc and (b) notched disc.

Corn stovers were collected from a field after harvest. To have uniform experiment conditions, all corn stovers had their leaves, ears, and husks removed, and were cut into 200 mm long corn stalks. The diameters of the corn stalks varied from 20.3 to 24.0 mm, averaging to 22.8 mm. Ten corn stalks were oven-dried at 55 degrees Celsius for 72 hours, the weights before and after oven-dried were used to calculate the average moisture content, which was found to be 9.6% ± 2.1%.

4.3.2 Soil–Cornstalk–Disc Model

4.3.2.1 Model Development

A DEM software (PFC^{3D}) was used for developing the soil–cornstalk–disc interaction model (Figure 4.3). A large number of spherical particles (10 mm in uniform diameter) were used to replicate the agricultural soil particles. The Parallel Bond Model (PBM) (Potyondy and Cundall, 2004) was used for mimicking the adhesion between soil particles. The soil domain was 900 mm (width), 1200 (length), and 500 mm (depth). After reaching equilibrium, soil particles above 200 mm were removed to create a flat soil surface. In the end, 240,327 bonded particles remained in the soil domain.

A model corn stalk was created using 10,148 spheres with uniform diameter. These spheres were filled into a cylinder having a diameter of 22.8 mm and a height of 200 mm, forming a corn stalk with the same average dimensions as the corn stalk collected from the field. These particles were bonded together using PBM, becoming a cylindrical, breakable solid like a real corn stalk. Then, the cylinder wall was deleted. To simulate residue cutting using discs, ten of such corn stalks were created with a specific longitudinal spacing and placed in the model soil domain in a row that was 225 mm away from the side of soil domain (Figure 4.3). This would leave enough distance (675 mm wide) to avoid the sidewall effect.

The models of the notched disc and plain disc were built by SolidWorks (CAD software). Then, the CAD disc models were imported into PFC^{3D}. Desired working depth, travelling speed, disc angle, and tilt angle were set to run the model disc in the soil. In addition, the disc was assigned with a rotation speed for representing a free rolling disc (Nalavade et al., 2010). The rotation speed was calculated by the desired travelling speed of disc, with an assumption that the rotation radius of the disc corresponds to its geometric radius (Murray and Chen, 2018).

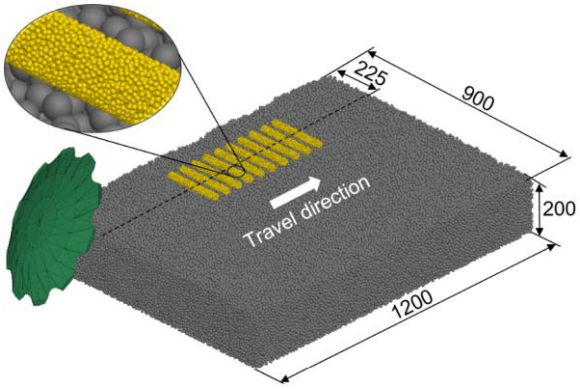

Figure 4.3. The soil–cornstalk–disc interaction model with soil particle assembly, corn stalks, and the notched disc. The dimensions are in mm.

4.3.2.2 Monitoring of Soil and Corn Stalk Micro-Dynamics

The disc interacted with the soil and corn stalks as it travelled through the soil (Figure 4.4). The resistances of disc, soil supporting force, corn stalk cutting effectiveness, corn stalk intrusion force, and corn stalk sinkage were quantified. The resistances of disc resulted from soil and corn stalks in horizontal and vertical directions, namely draft force and vertical force respectively, were monitored by built-in history functions in the software.

After the disc passed, corn stalks were either fully cut into two separate halves or remained intact. The number of corn stalks being fully cut was recorded. The corn stalk cutting effectiveness was determined as the percentage of fully cut corn stalks out of the original ten corn stalks.

It was observed that when the particle velocity of corn stalk was greater than 2 m s^{-1} (Figure 4.4a), the corn stalk was fully cut by the disc. The maximum depth that corn stalk embedded into soil was recorded as corn stalk sinkage (Figure 4.4b). The corn stalk sinkage was used to evaluate the risk of forming “compressed corn stalk”, a scenario of uncut on corn stalk as shown in the following experiment. A larger corn stalk sinkage creates an increasing of risk of “compressed corn stalk”.

At the moment the corn stalk was cut fully, the contact force of each soil particle and each corn stalk particle was monitored (Figure 4.4c). The maximum contact force of soil particles was defined as soil supporting force for examining the bearing effect of soil on corn stalk during the disc cutting. The maximum contact force of corn stalk particles was defined as corn stalk intrusion force for investigating the aggression of disc on cutting corn stalk.

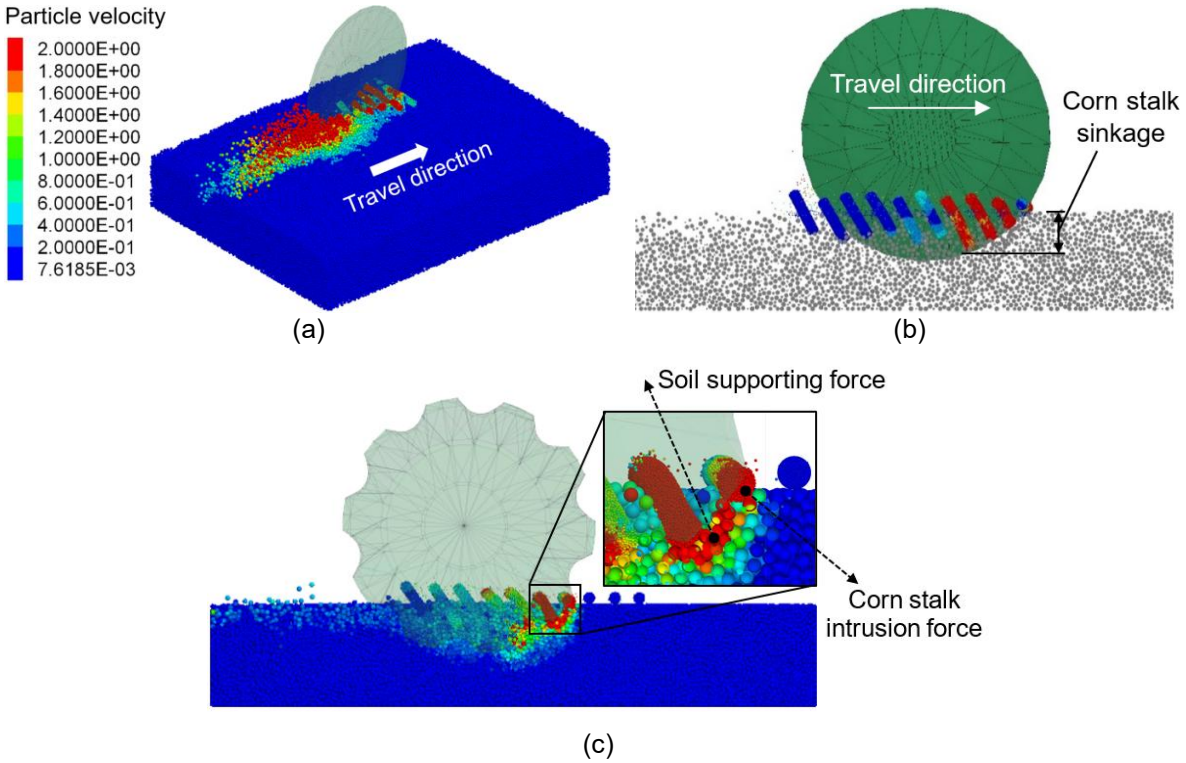

Figure 4.4. Model monitoring: (a) the resultant micro-dynamics (velocities, unit: m s^{-1}) of soil and corn stalk after the cutting by the plain disc; (b) the definition of corn stalk sinkage; and (c) the definition of soil supporting force and corn stalk intrusion force.

4.3.2.3 Calibrating Parameters for Model Corn Stalk

The model disc and boundary of soil domain were set the stiffness (1×10^8 N m^{-1}) and friction (0.5), while model parameters of soil (sandy loam soil) were referred to Mak and Chen (2015). The PBM contact models used for corn stalk were determined by several model parameters. The particle normal and shear stiffness, particle diameter, particle density, and particle local damping ratio were adopted from Adajar et al. (2021). The bond radius multiplier was determined as a common value of 0.5. Other parameters, including particle friction coefficient (μ), bond normal stiffness ($\overline{k_n}$), bond shear stiffness ($\overline{k_s}$), bond tensile strength (σ), and bond cohesion (c) were calibrated in this study. The $\overline{k_n}$ and σ were set to be equal to $\overline{k_s}$ and c respectively for simplicities.

Thus, only three parameters, $\overline{k_s}$, σ, and μ were calibrated. Table 4.1 shows the details of model parameters for soil and corn stalk.

Table 4.1. Summary of model parameters.

Model parameter	Symbol	Values and source	
		Soil (Mak and Chen, 2015)	Corn stalk
Particle normal stiffness, N m^{-1}	k_n	3,000	50,000 (Adajar et al., 2021)
Particle shear stiffness, N m^{-1}	k_s	3,000	50,000 (Adajar et al., 2021)
Friction coefficient	μ	0.36	To be calibrated
Particle density, kg m^{-3}	ρ	2650	450 (Adajar et al., 2021)
Particle diameter, mm	d_p	10	2 (Adajar et al., 2021)
Particle local damping ratio	θ	0.1	0.7 (Adajar et al., 2021)
Bond radius multiplier	λ	0.5	0.5 (Selected)
Bond normal stiffness, Pa m^{-1}	$\overline{k_n}$	4.95 × 10^7	To be calibrated
Bond shear stiffness, Pa m^{-1}	$\overline{k_s}$	4.95 × 10^7	= bond normal stiffness
Bond tensile strength, Pa	σ	38200	To be calibrated
Bond cohesion, Pa	c	13900	= bond cohesion

A corn stalk cutting model was developed for calibrating the parameters of model corn stalk, indicated in Table 4.1. The model simulated a notched blade moving downward, cutting a corn stalk as shown in Figure 4.5a. This setup was the same as the experimental setup in Igathinathane et al. (2010). Therefore, data from that study was used for calibrating corn stalk parameters. The model corn stalk for this simulation was 25 mm in length and 22.8 mm in diameter. It was formed with a total of 1,264 particles (2 mm in diameter) in the same way as the corn stalk in the soil–cornstalk–disc model. The SolidWorks software was used to create the CAD model of the notched blade, and the CAD model was imported into PFC^{3D}. For cutting simulation, the corn stalk was placed on a flat surface. The notched blade was assigned with a desired downward cutting speed.

The corn stalk cutting force (the resistance to the notched blade) in the vertical direction was monitored as the blade moved down to fully cut corn stalk. Figure 4.5b shows the changes in corn stalk cutting force as the blade moves downward.

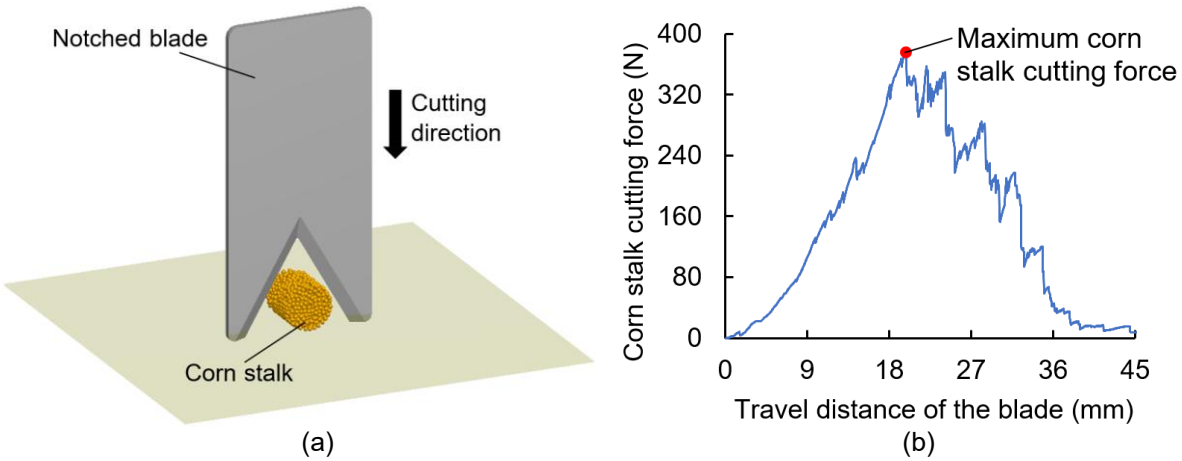

Figure 4.5. Simulations for model calibrations: (a) corn stalk cut by a blade and (b) an example of force-distance curve from the simulations.

During the calibration, five values of $\overline{k_n}$ for model inputs were 1.0×10^9, 1.5×10^9, 2.0×10^9, 2.5×10^9, and 3.0×10^9 N m^{-1}. Each value of $\overline{k_n}$ was paired with five values of σ of 7.0×10^6, 7.5×10^6, 8.0×10^6, 8.5×10^6, and 9.0×10^6 Pa, as well as five values of μ of 0.3, 0.4, 0.5, 0.6, and 0.7, resulted in a total of 125 simulation runs. The orthogonal experiment design (Table 4.2) was used for selecting the parameter sets required to be calibrated from 125 simulation runs. For each simulation, the maximum corn stalk cutting force as shown in Figure 4.5b was recorded. This simulated force was compared with the measured maximum corn stalk cutting force as reported by Igathinathane et al. (2010) to obtain the relative error (Mak and Chen, 2015).

Table 4.2*. Factors and levels of model simulation runs in the orthogonal experimental design for calibrating corn stalk parameters.

Code value	$\overline{k_n}$ (N m^{-1})	σ (Pa)	μ (Dimensionless)
-2	1.0×10^9	7.0×10^6	0.3
-1	1.5×10^9	7.5×10^6	0.4
0	2.0×10^9	8.0×10^6	0.5
1	2.5×10^9	8.5×10^6	0.6
2	3.0×10^9	9.0×10^6	0.7

* $\overline{k_n}$ = bond normal stiffness, σ = bond tensile strength, and μ = particle friction coefficient.

4.3.2.4 Model Validation

For validating model, measured data were collected from tests conducted on the notched disc in an indoor soil bin. The soil bin measured 10 metres in length, 0.9 metres in width, and 0.6 metres in depth, filled with sandy loam soil consisting of 70% sand, 16% silt, and 14% clay. Prior to each test, soil was prepared using the procedure of tilling-levelling-compacting, for obtaining relatively homogenous soil condition. The soil moisture content (d.b.) was 20.3% ± 0.2% and dry soil bulk density was 1.15 ± 0.03 Mg m^{-3}, determined using the soil core and oven-drying method (ASABE Standards, 2020).

The disc was mounted on the soil bin carriage at zero-degree angles (Figure 4.6a). A dynamometer between the disc shank and the soil bin carriage measured the resistances of disc. Along the length of the disc travelling path, 41 corn stalks were placed with 50 mm apart (Figure 4.6b). Then the disc travelled at 10 km h^{-1} and 100 mm working depth. Four tests were performed to minimize measurement error. As the disc moved through the soil, the dynamometer recorded the draft force and vertical force at a force signal frequency of 65 Hz. The corn stalks experienced

three different scenarios: fully cut, partially cut, and uncut (Figure 4.6c). Measured corn stalk cutting effectiveness was calculated as the ratio of cut corn stalks (both fully and partially cut) to the total number of the original corn stalks.

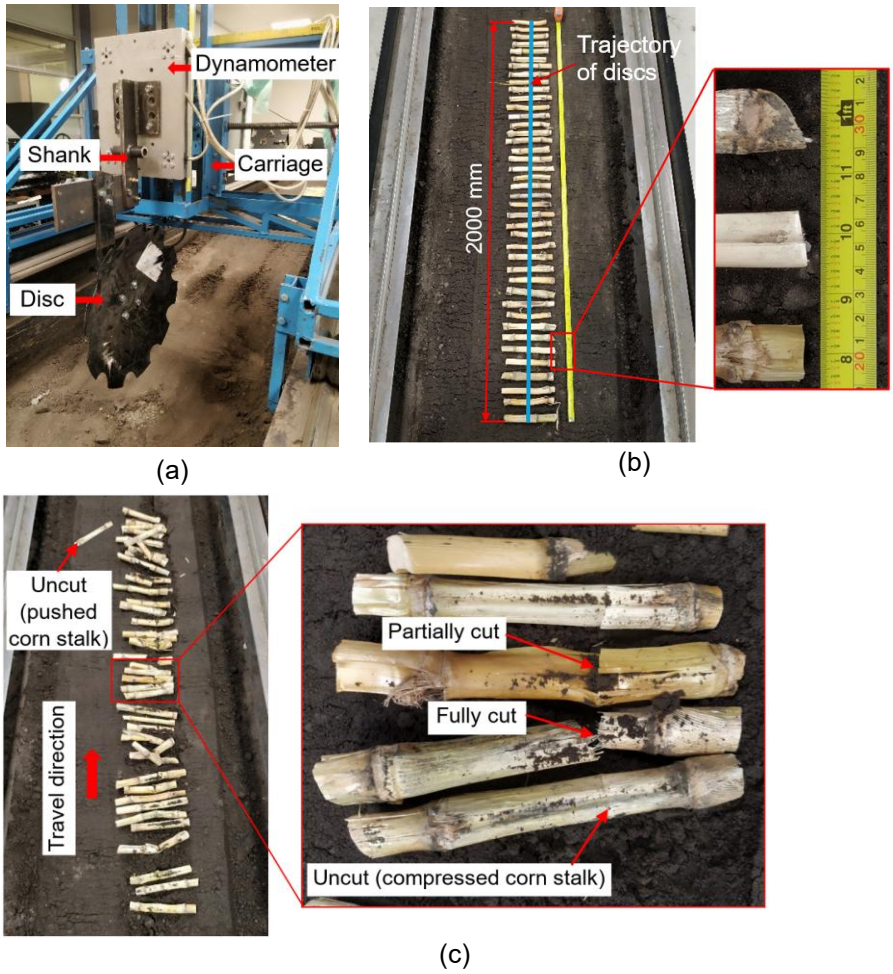

Figure 4.6. Experimental setup: (a) the soil bin testing facility showing the dynamometer, shank and notched disc; (b) corn stalks placed on soil surface before tillage; and (c) corn stalks after tillage, demonstrating three different cutting scenarios.

Simulations were performed using the soil–cornstalk–disc model to replicate the above tests. In the simulations, ten model corn stalks were evenly positioned with a spacing of 50 mm on the soil surface, and the disc travelled at the same operational parameters as in the tests. The resistances of

disc and corn stalk cutting effectiveness were used to validate the soil–cornstalk–disc model, by evaluating overall relative error between simulated data and measured data as following:

$$RE = \frac{1}{N}\sum_{i=1}^{N}\left(\frac{|M_i - S_i|}{M_i}\right) \times 100\% \qquad (4.1)$$

where RE = overall relative error, M = measured data, S = simulated data, N = number of variables, and i = i-th of the variables.

4.3.2.5 Model Application

Simulations were performed using the validated model for investigating the effects of disc types and soil bulk densities on micro-dynamic behaviours of soil and corn stalk. The types of disc were notched disc and plain disc. The levels of soil bulk density were Low-Density (1.06 Mg m^{-3}), Medium-Density (1.29 Mg m^{-3}), and High-Density (1.52 Mg m^{-3}), representing typical bulk densities of sandy loam soil (Dam et al., 2005; Acquah and Chen 2022). The levels of soil bulk density were created by adjusting the soil particle densities of 1880, 2290, and 2700 kg m^{-3}, corresponding to the soils of Low-Density, Medium-Density, and High-Density respectively (Bahrami et al., 2020). The disc angle and tilt angle were set as 10° and zero-degree respectively for matching the practical use (Kogut et al., 2016). The disc was run at a 20 km h^{-1} travelling speed and a 100 mm working depth. The time of each simulation was approximately 120 hours using a Dell Workstation with 192 GB RAM, a 2.10 GHz Intel (R), and Xeon (R) Silver 4110 CPU (2 processors). The default timestep (approximately 3e-7 s) that was automatically calculated was used throughout simulations.

4.4. Results and Discussion

4.4.1 Model Calibration Results

During the model calibration, corn stalk cutting was simulated using the same setup as the test by Igathinathane et al. (2010), except for the downward cutting speed. A higher downward cutting speed was used, as the downward cutting speed (0.00042 m s^{-1}) used by Igathinathane et al. (2010) was too low to run due to the limited computer capacity. To find an appropriate downward cutting speed to be used in simulations, a preliminary simulation was conducted to examine how downward cutting speeds affect the maximum corn stalk cutting force. Four downward cutting speeds (0.0042, 0.021, 0.042, and 0.42 m s^{-1}) were used and each speed was replicated four times in the simulations. Eventually, there was no significant difference on maximum corn stalk cutting force when the downward cutting speed of blade was 0.042 m s^{-1} and lower (Figure 4.7). Thus, the speed 0.042 m s^{-1}, a value that was appropriate for the computer capacity without sacrificing the model reliability, was used in model parameter calibrations.

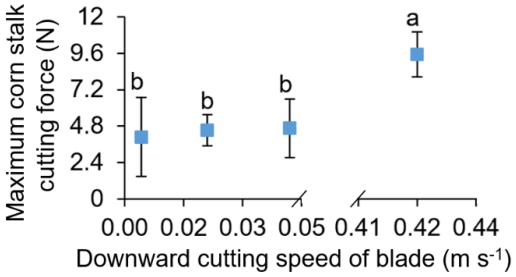

Figure 4.7. Maximum corn stalk cutting force at different downward cutting speeds of blade in model calibration; bond normal and shear stiffness = 2.0 × 10^7 N m^{-1}, bond tensile strength = 5.0 × 10^5 Pa, bond cohesion = 1.0 × 10^5 Pa, particle friction = 0.7; different letters (a or b) represent significantly different between according to Duncan's multiple range test (0.05 significance level).

Using the chosen downward cutting speed of blade, twenty simulations were run for different parameter sets of bond normal stiffness ($\overline{k_n}$), bond tensile strength (σ), and particle friction (μ). Simulated results of maximum corn stalk cutting force are shown in Table 4.3. These simulated forces were compared with the measured maximum corn stalk cutting force of 395.9 N (Igathinathane et al., 2010). It was found that the run number 11 had the least relative error that is 2.0% (Table 4.3). Therefore, the calibrated parameters were 2.0×10^9 N m^{-1}, 8.0×10^6 Pa, and 0.5 for $\overline{k_n}$, σ, and μ respectively. These three values were used in all subsequent simulations.

Table 4.3*. Simulation results for calibrations of corn stalk model parameters.

Run	$\overline{k_n}$ (N m^{-1})	σ (Pa)	μ (Dimensionless)	Maximum corn stalk cutting force (N)	Relative error (%)
1	1.5 × 10^9	7.5 × 10^6	0.6	464.23	14.7
2	1.0 × 10^9	8.0 × 10^6	0.5	523.29	24.3
3	2.0 × 10^9	7.0 × 10^6	0.3	359.13	10.2
4	3.0 × 10^9	7.5 × 10^6	0.7	255.38	55.0
5	2.0 × 10^9	9.0 × 10^6	0.5	465.59	15.0
6	2.0 × 10^9	9.0 × 10^6	0.7	555.39	28.7
7	1.5 × 10^9	7.5 × 10^6	0.4	569.19	30.4
8	2.0 × 10^9	8.0 × 10^6	0.7	537.47	26.3
9	3.0 × 10^9	7.0 × 10^6	0.4	292.22	35.5
10	1.0 × 10^9	7.0 × 10^6	0.3	539.19	26.6
11	**2.0 × 10^9**	**8.0 × 10^6**	**0.5**	**403.99**	**2.0**
12	1.0 × 10^9	7.0 × 10^6	0.7	469.95	15.8
13	1.0 × 10^9	9.0 × 10^6	0.3	751.76	47.3
14	1.5 × 10^9	8.5 × 10^6	0.4	629.85	37.1
15	3.0 × 10^9	9.0 × 10^6	0.6	375.85	5.3
16	2.0 × 10^9	7.0 × 10^6	0.5	376.14	5.3
17	3.0 × 10^9	8.5 × 10^6	0.3	346.40	14.3
18	1.0 × 10^9	9.0 × 10^6	0.7	528.59	25.1
19	2.0 × 10^9	8.0 × 10^6	0.3	427.09	7.3
20	1.0 × 10^9	8.0 × 10^6	0.5	523.49	24.4

*$\overline{k_n}$ = bond normal stiffness, σ = bond tensile strength, μ = particle friction coefficient.

4.4.2 Model Behaviours and Validation Results

Model behaviours were examined using the results of velocity distribution of corn stalk particles. As the disc travelled in the soil and passing the corn stalks, three distinct regions were characterized based on the particle flow behaviours. Several corn stalks were cut simultaneously by the front edge of disc, named cutting region (Figure 4.8a). The disc concave shape resulted in a calming region where corn stalks were cut into two halves. Particle velocity of corn stalk in this region was lower than that in the cutting region, indicating the little disturbance on corn stalks in the calming region. As the disc continuously travelled forward, two halves of corn stalk approached into a side throwing region. In this region, one half of corn stalk on the concave side of disc was thrown aside, while the other half on the convex side left on original position.

Corn stalks in the cutting region had two scenarios: edged cutting and notched cutting, as shown in Figure 4.8b. In the scenario of the edged cutting, corn stalk was cut by the outer edge of disc. The particle at cutting point had larger velocity than its two ends, indicating that the edged cutting occurred immediately when the disc edge contacted with the corn stalk. In the scenario of the notched cutting, corn stalk particles that contacted with soil had lower velocities than the others. Corn stalk particles were decelerated by the friction caused by relative movement of soil and corn stalk, as the corn stalks were compressed into soil.

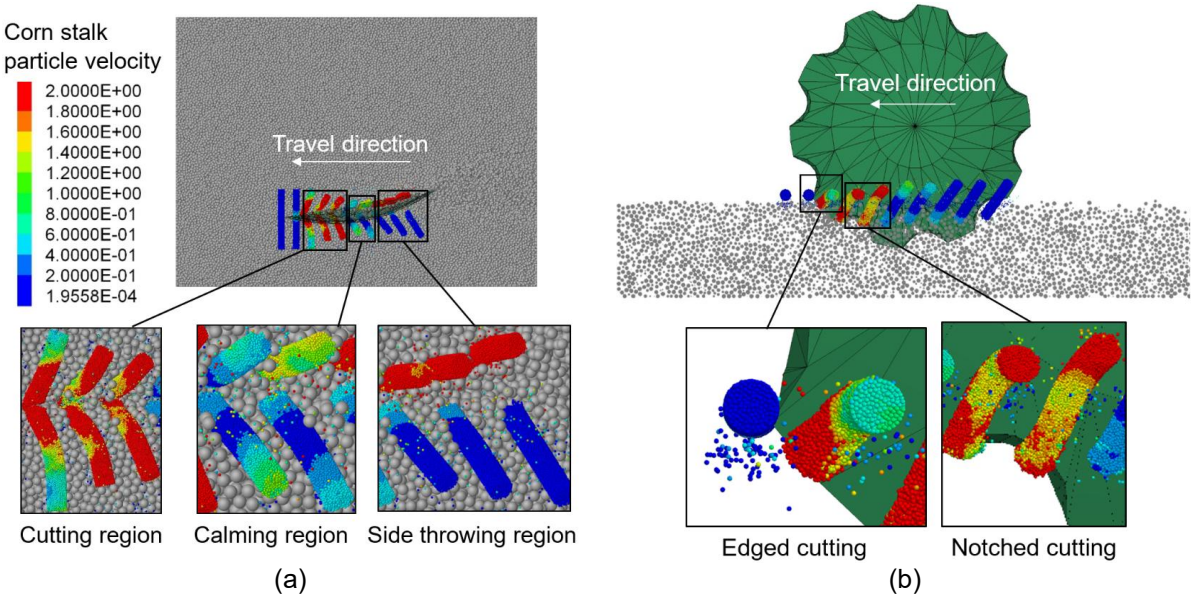

Figure 4.8. Particle velocity (unit: m s^{-1}) flow distribution of corn stalks: (a) top view and (b) side view, as the notched disc travelled at zero-degree tilt angle, 10° disc angle, 100 mm working depth, and 20 km h^{-1} traveling speed in the soil of High-Density (1.52 Mg m^{-3}).

The soil–cornstalk–disc model was evaluated by comparing results from the soil bin tests and simulations (Table 4.4). Test results showed that the notched disc had 76.2% of corn stalk cutting effectiveness. In the simulation, 100% of model corn stalks were fully cut, due to the homogeneous properties of corn stalks and soil, resulting in a high relative error. The model had low relative errors for predicting the draft force and vertical force. The overall relative error was 16.4%, suggesting that the accuracy of the soil–cornstalk–disc model was acceptable.

Table 4.4. The results of model validation using the overall relative error (*RE*) between the measured data and simulated data as the notched disc travelled at zero-degree angles, 100 mm working depth, and 20 km h^{-1} travelling speed.

Indicator	Measurement	Simulation	Relative error (%)
Corn stalk cutting effectiveness (%)	76.2	100.0	31.2
Draft force (N)	301.9	272.4	9.8
Vertical force (N)	323.8	297.3	8.2
Overall relative error, *RE* (%)			16.4

4.4.3 Applications of the Soil–Cornstalk–Disc Model for Different Disc Types and Soil Bulk Densities

4.4.3.1 Simulated Corn Stalk Micro-Dynamics

The transient states of behaviours of corn stalk in soils can be directly observed from the velocity fields of corn stalks. As the notched disc approached, the corn stalks on the soil of High-Density were cut by both edges and notches simultaneously (Figure 4.9a). A similar phenomenon was also observed in the soil of Medium-Density (Figure 4.9b). As the soil changed to Low-Density, the corn stalks were no longer cut directly by the disc edges, instead all corn stalks to be cut were gathered by the disc notches (Figure 4.9c). Therefore, the corn stalk cutting process of notched disc can be summarized as “touching-compressing-cutting” in the soil of High-Density and Medium-Density, while as “touching-gathering-compressing-cutting” in the soil of Low-Density. The “gathering” behaviour of notched disc in the soil of Low-Density had complex effect on corn stalk cutting effectiveness. The positive effect was that the corn stalk at the disc notch was less likely to be pushed ahead, resulting from the small angle of the absolute velocity acting on the

corn stalk (Kushwaha et al., 1986). However, the negative effect was, the cutting resistance increased as several corn stalks were gathered into the notch. From the circumstance of all corn stalks being cut in the simulation, the "gathering" behaviour had greater positive effect than the negative effect on corn stalk cutting under current operational parameters (i.e., zero-degree tilt angle, 10° disc angle, 100 mm working depth, 20 km h^{-1} travelling speed).

For the plain disc, all corn stalks were touched, compressed, and cut by the disc edge of plain disc (i.e. "touching-compressing-cutting"). There were several minor differences on the corn stalks that were fully cut among three soil bulk densities. Intuitively, the corn stalks in the soil of High-Density (Figure 4.9d) statically stayed in a shallower soil than that in the soils of Medium-Density (Figure 4.9e) and Low-Density (Figure 4.9f). The possible reason was that, in the soils of Medium-Density and Low-Density, the soil provided low soil supporting to corn stalks at the same soil depth (Zhong et al., 2023). Overall, the corn stalk that was fully cut in the soils of Medium-Density and Low-Density had larger particle velocity than that in the soil of High-Density, indicating a more severe disturbance on corn stalks.

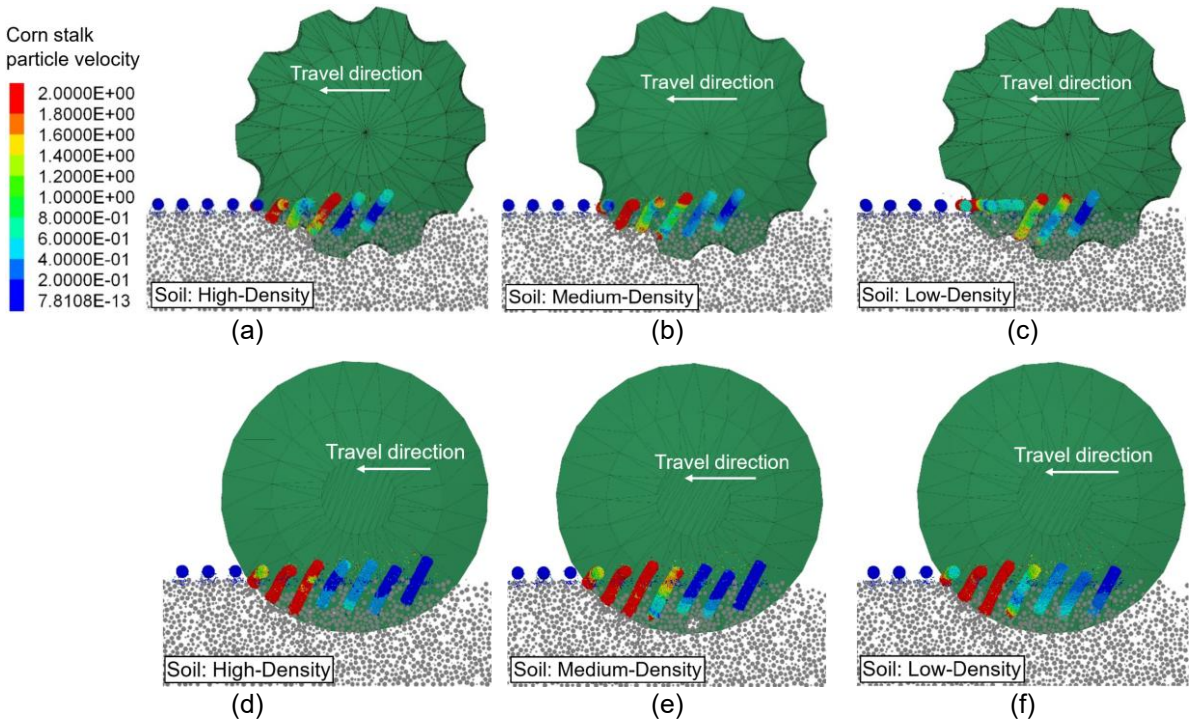

Figure 4.9. Cutting behaviours of corn stalks observed by particle velocity (unit: m s^{-1}) flow distribution when using notched disc in the soils: (a) High-Density; (b) Medium-Density; (c) Low-Density; as well as when using plain disc in the soils: (d) High-Density; (e) Medium-Density; and (f) Low-Density, as the disc travelled at a zero-degree tilt angle, 10° disc angle, 100 mm working depth, and 20 km h^{-1} travelling speed. Soil bulk density: High-Density = 1.52 Mg m^{-3}, Medium-Density = 1.29 Mg m^{-3}, and Low-Density = 1.06 Mg m^{-3}.

The corn stalk sinkage in the soil of Low-Density was 60.8 mm, a maximum value among three soil bulk densities (Figure 4.10). The minimum corn stalk sinkage occurred in the soil of High-Density, a slightly smaller 2.6% than the maximum value. Therefore, the soil bulk density had minor effect on the corn stalk sinkage. It was speculated that the high speed (20 km h^{-1}) of disc lowered the required corn stalk cutting force (Soleimani et al., 2023), thereby weakening the influence of soil bulk density on corn stalk sinkage. However, a tendency was still observed that corn stalk sinkage increased as the soil bulk density decreased from 1.52 to 1.06 Mg m^{-3}. The corn stalks in the soil of Low-Density were compressed deeper into the soil. It was therefore inferred that the scenario of uncut corn stalk (compressed corn stalk) was prone to be resulted in the soil of

Low-Density. This inference agreed the results reported by Aikins et al. (2020) that failure of cutting corn residue would be more severe in wetted or loosen soil.

The corn stalk sinkage caused by the plain disc was larger than that the notched disc, a gap of 22.2% (Figure 4.10). The reason was attributed to the superior ability of penetration of notched disc, reducing the phase of "compressing" on corn stalks. From the difference of corn stalk sinkage, an inference was stated that notched disc fully cut more corn stalks, thus creating less uncut corn stalks (compressed corn stalk) in practice. This agreed to the comparison of corn stalk cutting effectiveness in the study of Zeng et al. (2021). When the disc travelled at zero-degree tilt angle, 10° disc angle, 100 mm working depth, and 20 km h^{-1} travelling speed, the variation of corn stalk sinkage resulted from the difference on disc type was greater than from the difference on the soil bulk density, implying a greater influence of disc type on corn stalk cutting effectiveness.

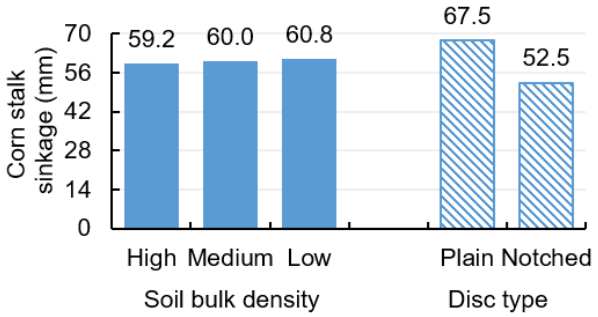

Figure 4.10. Corn stalk sinkage at different discs and soil bulk densities (Soil: High-Density = 1.52 Mg m^{-3}, Medium-Density = 1.29 Mg m^{-3}, and Low-Density = 1.06 Mg m^{-3}), as the discs travelled at a zero-degree tilt angle, 10° disc angle, 100 mm working depth, and 20 km h^{-1} travelling speed.

The corn stalk intrusion forces at different disc types and soil bulk densities are shown in Figure 4.11. The corn stalk intrusion force quantifies the resistance a disc blade must overcome to penetrate a corn stalk. High intrusion forces suggest that sharper disc edges are needed to reduce energy loss and ensure effective cutting, especially under high-coverage of crop residue conditions.

The corn stalks in the soil of High-Density experienced maximum corn stalk intrusion force (43.3 N), followed by 26.5 N in the soil of Medium-Density and 20.6 N in the soil of Low-Density. The corn stalk intrusion force decreased as the soil bulk density decreased. The difference on corn stalk intrusion force was attributed to the "buffer" effect of discrete soil particles. A lower soil bulk density buffered a greater corn stalk intrusion force. The notched disc resulted in the corn stalk intrusion force of 42.6 N, 58.5% larger than the plain disc. This circumstance further confirmed that the structure of notch enhanced the penetration on corn stalk.

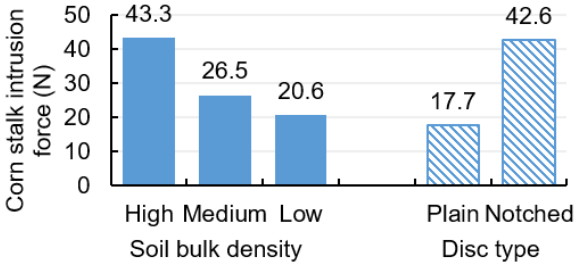

Figure 4.11. Corn stalk intrusion force at different disc types and soil bulk densities (Soil: High-Density = 1.52 Mg m^{-3}, Medium-Density = 1.29 Mg m^{-3}, and Low-Density = 1.06 Mg m^{-3}), as the discs travelled at a zero-degree tilt angle, 10° disc angle, 100 mm working depth, and 20 km h^{-1} travelling speed.

4.4.3.2 Simulated Soil Micro-Dynamics

The transient states of behaviours of soils can be directly observed from the contact force fields of soil particles. The soil particles had contact forces up to 0.7 N. These "high force" particles (red particles in Figure 4.12) were highlighted to observe soil disturbance characteristics. As the notched disc travelled, the "high force" particles in the soil of High-Density were evenly distributed along the edge of the disc (Figure 4.12a), while those in the soil of Medium-Density were clearly concentrated under the corn stalks (Figure 4.12b). Under the corn stalk, more soil particles participated in supporting corn stalks in the soil of Medium-Density than in the soil of Low-Density. More critical feature occurred in the soil of Low-Density, where few "high force"

particles were distributed along the disc edge, as corn stalks were gathered to the notch (Figure 4.12c). This phenomenon further illustrated the influence of soil as corn stalk was cut by disc.

In the simulations, the number of “high force” affected by the plain disc was greater than that of the notched disc. In the soils of High-Density (Figure 4.12d) and Medium-Density (Figure 4.12e), the “high force” particles were concentrated under the corn stalks. However, the “high force” particles were evenly distributed along the cutting edge in the soil of Low-Density (Figure 4.12f). The number of “high force” particles increased observationally as the soil bulk density decreased. This further confirms the differences in the supporting effect of soils with different bulk densities, thus quantitively analysing later.

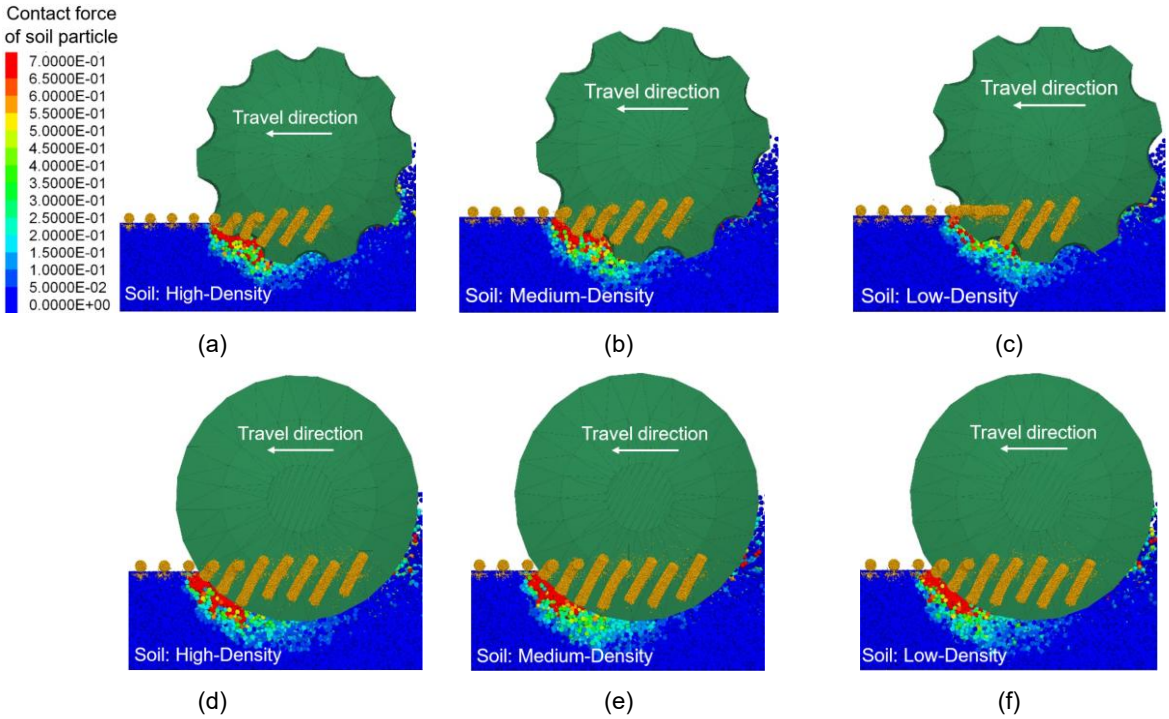

Figure 4.12. Soil micro-dynamic behaviours observed by soil particle contact force (unit: N) flow distribution when using notched disc in the soils: (a) High-Density; (b) Medium-Density; (c) Low-Density; as well as when using plain disc in the soils: (d) High-Density; (e) Medium-Density; and (f) Low-Density, as the disc travelled at a zero-degree tilt angle, 10° disc angle, 100 mm working depth, and 20 km h^{-1} travelling speed. Soil bulk density: High-Density = 1.52 Mg m^{-3}, Medium-Density = 1.29 Mg m^{-3}, and Low-Density = 1.06 Mg m^{-3}.

Soil provides support to enable more efficient corn stalk cutting, which is affected by the residue quantity and soil property. To quantitatively examine this soil supporting effect, soil supporting force was defined and recorded (Figure 4.13). On average, the soil supporting force was 285.8 N when the notched disc was travelling, which was 33.8% less than that of the plain disc. Therefore, it was predicted that the greater the soil supporting force required, the more difficult the corn stalks were cut fully.

The soil of High-Density experienced the minimum soil supporting force of 246.9 N under the simulation of notched disc. The soil of Medium-Density had the maximum soil supporting force,

29.5% higher than the minimum value. There was no linear trend on soil supporting force as the soil bulk density changed, because of the complexity of corn stalk cutting behaviours caused by the structure of notch. For plain disc, the soil supporting force had a gradual increasing trend from 141.2 N to 598.9 N, a difference of 76.4%, as the soil bulk density decreased from 1.52 Mg m^{-3} to 1.06 Mg m^{-3}. The corn stalks on the soil of low bulk density were obviously not conducive to be cut by the plain disc.

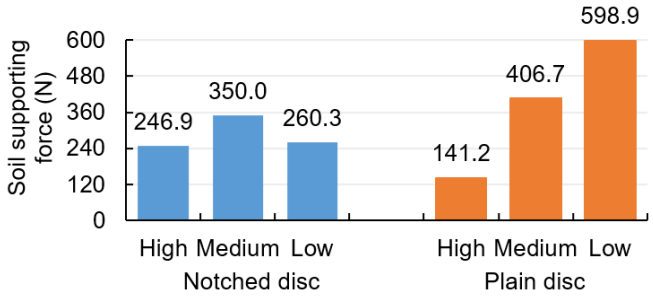

Figure 4.13. Soil supporting force at different disc types and soil bulk densities (Soil: High-Density = 1.52 Mg m^{-3}, Medium-Density = 1.29 Mg m^{-3}, and Low-Density = 1.06 Mg m^{-3}), as the discs travelled at a zero-degree tilt angle, 10° disc angle, 100 mm working depth, and 20 km h^{-1} travelling speed.

4.5. Conclusions

A soil–cornstalk–disc interaction model was constructed using the DEM. By matching experimental results to simulation results, the model parameters were calibrated to 2.0×10^9 N m^{-1} for particle normal stiffness, 8.0×10^6 N m^{-1} for bond tensile strength, and 0.5 for particle friction. The model produced an overall relative error of 16.4% for predicting corn stalk cutting effectiveness, draft, force and vertical force of a concave disc. When the notched disc was used, corn stalks were cut by both disc notches and disc edges in the soils of High-Density and Medium-Density, while merely cut by disc notches in the soil of Low-Density. As the soil bulk density decreased, the simulated corn stalk sinkage increased slightly, while the corn stalk intrusion force

decreased. The soil supporting force increased continuously as the soil bulk density increased when using the plain disc, but no obvious trend was found when using notched disc. As the corn stalks were cut by notched disc, the soil supporting force was required 33.8% less than by the plain disc. The plain disc had larger corn stalk sinkage but smaller corn stalk intrusion force than the notched disc. The corn stalk sinkage and corn stalk intrusion force were more significantly affected by disc type than soil bulk density. This research advances the understanding of tillage equipment for crop residue management by providing insights into residue and soil micro-dynamics. While the model effectively simulates these interactions under controlled conditions, further investigation is required to validate its applicability across different soil types.

4.6. Acknowledgements

This study was financially supported by Hainan Province Foreign Experts Program, China (G20250218002Y), CSC, China (202007565032), and NSERC of Canada (RGPIN-2019-05861).

4.7. References

Abu-Hamdeh, N. H., and Reeder, R. C., 2003. A nonlinear 3D finite element analysis of the soil forces acting on a disk plow. Soil and Tillage Research, 74(2), 115–124. https://doi.org/10.1016/S0167-1987(03)00152-1

Acquah, K., and Chen, Y., 2022. Soil compaction from wheel traffic under three tillage systems. Agriculture (Switzerland), 12(2), e0219. https://doi.org/10.3390/agriculture12020219

Adajar, J. B., Alfaro, M., Chen, Y., and Zeng, Z., 2021. Calibration of discrete element parameters of crop residues and their interfaces with soil. Computers and Electronics in Agriculture, 188, e106349. https://doi.org/10.1016/j.compag.2021.106349

Ahmad, F., Ding Weimin, Ding Qishou, Rehim, A., and Jabran, K., 2017. Comparative performance of various disc-type furrow openers in no-till paddy field conditions. Sustainability, 9(7), e1143. https://doi.org/10.3390/su9071143

Ahmad, F., Ding Weimin, Ding Qishuo, Hussain, M., and Jabran, K., 2015. Forces and straw cutting performance of double disc furrow opener in no-till paddy Soil. PloS One, 10(3), e0119648. https://doi.org/10.1371/journal.pone.0119648

Aikins, K. A., Barr, J. B., Ucgul, M., Jensen, T. A., Antille, D. L., and Desbiolles, J. M. A., 2020. No-tillage furrow opener performance: A review of tool geometry, settings and interactions with soil and crop residue. Soil Research (Collingwood, Vic.), 58(7), 603–621. https://doi.org/10.1071/SR19153

ASABE Standards, 2020. ASABE Standard S633: Testing protocol for landscape irrigation soil moisture-based control technologies. American Society of Agricultural and Biological Engineers, St. Joseph, MI.

Bae, B. M., Kim, Y. S., Kim, W. S., Kim, Y. J., Lee, S. D., and Kim, T. J., 2023. The development of a draft force prediction model for agricultural tractors based on the discrete element method in loam and clay loam. Agriculture (Switzerland), 13(12), e2205. https://doi.org/10.3390/agriculture13122205

Bahrami, M., Naderi-Boldaji, M., Ghanbarian, D., Ucgul, M., and Keller, T., 2020. DEM simulation of plate sinkage in soil: Calibration and experimental validation. Soil and Tillage Research, 203, e104700. https://doi.org/10.1016/j.still.2020.104700

Bianchini, A., and Magalhães, P. S. G., 2008. Evaluation of coulters for cutting sugar cane residue in a soil bin. Biosystems Engineering, 100(3), 370–375. https://doi.org/10.1016/j.biosystemseng.2008.04.012

Dam, R. F., Mehdi, B. B., Burgess, M. S. E., Madramootoo, C. A., Mehuys, G. R., and Callum, I. R., 2005. Soil bulk density and crop yield under eleven consecutive years of corn with different tillage and residue practices in a sandy loam soil in central Canada. Soil and Tillage Research, 84(1), 41–53. https://doi.org/10.1016/j.still.2004.08.006

Igathinathane, C., Womac, A. R., and Sokhansanj, S., 2010. Corn stalk orientation effect on mechanical cutting. Biosystems Engineering, 107(2), 97–106. https://doi.org/10.1016/j.biosystemseng.2010.07.005

Kong, L., 2014. Maize residues, soil quality, and wheat growth in China. A review. Agronomy for Sustainable Development, 34(2), 405–416. https://doi.org/10.1007/s13593-013-0182-5

Krushwaha, R. L., Vaishnav, A. S., and Zoerb, G. C., 1986. Soil bin evaluation of disc coulters under no-till crop residue conditions. Transactions of the ASAE, 29(1), 40–44. https://doi.org/10.13031/2013.30098

Kumar, N., Sawant, C. P., Sharma, R. K., Chhokar, R. S., Tiwari, P. S., Singh, D., Roul, A. K., Tripathi, S. C., Gill, S. C., and Singh, G. P., 2021. Combined effect of disc coulters and operational speeds on soil disturbance and crop residue cutting under no-tillage system in soil bin. Journal of Scientific & Industrial Research (New Delhi, India : 1963), 80(9), 739–749. https://doi.org/10.56042/jsir.v80i09.40333

Li, S., Diao, P., Miao, H., Zhao, Y., Li, X., and Zhao, H., 2024. Modeling the fracture process of wheat straw using a discrete element approach. Powder Technology, 439, e119726. https://doi.org/10.1016/j.powtec.2024.119726

Liu, L., Wang, X., Zhang, X., Zhong, X., Wei, Z., Geng, Y., Cheng, X., Zhao, K., and Bai, M., 2023. Determination and verification of parameters for the discrete element modelling of single disc covering of flexible straw with soil. Biosystems Engineering, 233, 151–167. https://doi.org/10.1016/j.biosystemseng.2023.08.001

Magalhães, P. S. G., Bianchini, A., and Braunbeck, O. A., 2007. Simulated and experimental analyses of a toothed rolling coulter for cutting crop residues. Biosystems Engineering, 96(2), 193–200. https://doi.org/10.1016/j.biosystemseng.2006.10.014

Mak, J., and Chen, Y., 2015. Simulation of draft forces of a sweep in a loamy sand soil using the discrete element method. Canadian Biosystems Engineering, 56(1), 2.1-2.7. https://doi.org/10.7451/CBE.2014.56.2.1

Malhi, S. S., and Lemke, R., 2007. Tillage, crop residue and N fertilizer effects on crop yield, nutrient uptake, soil quality and nitrous oxide gas emissions in a second 4-yr rotation cycle. Soil and Tillage Research, 96(1), 269–283. https://doi.org/10.1016/j.still.2007.06.011

McClellan, R. C., McCool, D. K., and Rickman, R. W., 2012. Grain yield and biomass relationship for crops in the Inland Pacific Northwest United States. Journal of Soil and Water Conservation, 67(1), 42–50. https://doi.org/10.2489/jswc.67.1.42

Mouazen, A. M., and Ramon, H., 2002. A numerical–statistical hybrid modelling scheme for evaluation of draught requirements of a subsoiler cutting a sandy loam soil, as affected by

moisture content, bulk density and depth. Soil and Tillage Research, 63(3), 155–165. https://doi.org/10.1016/S0167-1987(01)00243-4

Murray, J. R., Tullberg, J. N., and Basnet, B. B., 2006. Planters and their components: types, attributes, functional requirements, classification and description. Australian Centre for International Agricultural Research.

Parihar, D. S., Dogra, B., Narang, M. K., Javed, M., and Singh, D., 2024. Integrated seeding attachment for combine harvesters: a sustainable approach for conservation agriculture. Environment, Development and Sustainability, 26(11), 27805–27825. https://doi.org/10.1007/s10668-023-03787-9

Potyondy, D. O., and Cundall, P. A., 2004. A bonded-particle model for rock. International Journal of Rock Mechanics and Mining Sciences (Oxford, England: 1997), 41(8), 1329–1364. https://doi.org/10.1016/j.ijrmms.2004.09.011

Serrano, J. M., Peça, J. O., Pinheiro, A., Carvalho, M., Nunes, M., Ribeiro, L., and Santos, F., 2003. The effect of gang angle of offset disc harrows on soil tilth, work rate and fuel consumption. Biosystems Engineering, 84(2), 171–176. https://doi.org/10.1016/S1537-5110(02)00261-1

Shi, Y., Jiang, Y., Wang, X., Thuy, N. T. D., and Yu, H., 2023. A mechanical model of single wheat straw with failure characteristics based on discrete element method. Biosystems Engineering, 230, 1–15. https://doi.org/10.1016/j.biosystemseng.2023.03.017

Upadhyay, G., and Raheman, H., 2018. Performance of combined offset disc harrow (front active and rear passive set configuration) in soil bin. Journal of Terramechanics, 78, 27–37. https://doi.org/10.1016/j.jterra.2018.04.002

Wang, W., Lv, X., and Yi, Z., 2022. Parameter optimization of reciprocating cutter for Chinese little greens based on finite element simulation and experiment. Agriculture (Switzerland), 12(12), e2131. https://doi.org/10.3390/agriculture12122131

Zeng, Z., Thoms, D., Chen, Y., and Ma, X., 2021. Comparison of soil and corn residue cutting performance of different discs used for vertical tillage. Scientific Reports, 11(1), e2537. https://doi.org/10.1038/s41598-021-82270-9

Zhang, T., Zhao, M., Liu, F., Tian, H., Wulan, T., Yue, Y., and Li, D., 2020. A discrete element method model of corn stalk and its mechanical characteristic parameters. Bioresources, 15(3), 9337–9350. https://doi.org/10.15376/BIORES.15.4.9337-9350

Chapter 5: DEM Modelling of Crop Residue and Soil Dynamics as Affected by the Tillage Direction of a Disc Harrow *

*Published in *Biosystems Engineering* (in press)

5.1. Abstract

A comprehensive understanding of crop residue and soil dynamics under tillage is critical for improving the operational efficiency of tillage implements. A tandem disc harrow and its interaction with wheat residue in a sandy loam soil was modelled using the discrete element method. The model was able to simulate two tillage directions: perpendicular and parallel to standing wheat stubble rows (named as Perp-Direction and Para-Direction respectively). The model was validated using field measurement data. Experimental results revealed that Perp-Direction produced significantly lower residue cover compared to Para-Direction. Both tillage directions exhibited similar stubble forward displacements, averaging 354 mm. The model predicted these variables with an overall relative error of 19.7%. Simulation results also showed that stubble trajectories and soil cutting forces varied among individual discs due to the tandem arrangement of the harrow. These variables were further influenced by operational parameters: disc angle, harrow travelling speed and working depth. Lowering these parameters led to decreased soil surface roughness for both tillage directions. Conversely, increasing these operational parameters required higher total draft forces and disturbed a larger soil area. However, the soil cutting efficiency, a performance index incorporating both total draft force and soil disturbance area, was reduced under these conditions. These findings offer valuable insights for optimizing tillage direction and operational parameters of tandem disc harrows to enhance field performance.

Keywords: Disc harrow; DEM; wheat stubble; Dynamics; Soil

5.2. Introduction

The amount of crop residue remained on the soil surface is critical for mitigating soil degradation and increasing crop yields (Prosperi et al., 2011). In conservation tillage, the disc harrow is a key implement to maintain some residue on the soil surface while tilling the soil for preparation of good seedbeds. A disc harrow features multiple discs arranged according to specified parameters, such as disc spacing, disc angle, and the offset distance between adjacent discs. These parameters influence the performance, such as the soil resistance of disc harrow (Kogut et al., 2016). Disc gang angle affected fuel consumption, while had not significant impact on soil tilth (Serrano et al., 2003). The spacing of discs affected the soil disturbance area (Zeng et al., 2019). However, existing studies on disc harrows have primarily focused on tillage forces and soil disturbance, and their impact on the dynamics of crop residue was overlooked. A comprehensive understanding of the interactions between soil, crop residue, and disc harrow is essential for enhancing the performance in crop residue management.

Comparing with flat laying crop residue, standing crop stubble is more effective in reducing soil erosion and water evaporation (Bilbro and Fryrear, 1994). Wheat stubbles are arranged in dense and well-defined rows across the field, which has been shown to affect the seeding quality and plant growth (Strydhorst et al., 2019; Verrell et al., 2017). A straw clearing mulching device was typically set to travel parallelly to the wheat stubble rows (Hou et al., 2022). The reason was attributed to minimize disruption of the soil, prevent the residue clogging, and preserve residue coverage. The seeder openers were performed perpendicular to the oat stubble rows (Doan et al., 2005), which improves soil-to-seed contact for proper germination. It has been assumed that the

tillage direction relative to wheat standing stubble rows influences the tillage performance of disc harrow; however, this assumption has not yet been confirmed.

As a disc harrow travelled through a field, operational parameters significantly affected tillage performance (Damanauskas et al., 2019; Damanauskas and Janulevičius, 2022). For example, Kogut et al. (2016) stated that as the gang angle of disc harrow increased from 12 to 21°, the soil resistance increased in the horizontal direction but decreased in the vertical direction. The disc harrow worked in a greater depth had higher soil cutting area ratio and soil loosening efficiency (Zeng et al., 2019). However, the effects of operational parameters on the dynamics of residue have not been well documented yet, leaving a gap in effectively use of disc harrow for residue management.

Modelling approaches have been used in predicting dynamic behaviours of soil and crop residue in tillage. For example, a mathematical regression model was developed for predicting the soil resistance of an offset disc harrow, achieving relatively accurate prediction (Upadhyay and Raheman, 2019). A theoretical model was developed based on the classical soil mechanics for predicting draft force of disc harrow (Ahmadi, 2018). Discrete element models (DEM) provide deeper insights into the dynamic attributes of crop residue, beyond soil forces. For example, the residue displacements, moving trajectories, and incorporation were predicted in a DEM model (Zeng and Chen, 2019; Liu et al., 2023; Zeng et al., 2020). Zhong et al. (2023) examined the effects of soil moisture content on the residue-cutting ability in DEM model. However, there was a lack of DEM modelling of an entire disc harrow that involves dynamic interactions between individual discs on the harrow, a real-life situation.

This study therefore had the following objectives: (1) developing a DEM model to simulate a disc harrow operated in two tillage directions: parallel and perpendicular to the standing wheat

stubble rows, (2) validating the model by comparing experimental data with simulated data, and (3) simulating the dynamic behaviours of soil and wheat residue under different operational parameters of the harrow.

5.3. Methodology

5.3.1 Field Experiment

The purpose of the experiment was to support model development and validation by providing measurement data. Rather than large-scale data collection, the experiment was specifically designed to capture key parameters and variables sufficient for parameter selection and assessing the accuracy of model predictions.

5.3.1.1 Experimental Field and Equipment Setup

A field experiment was performed in the Municipality of Piney, Manitoba, Canada, on a sandy loam soil (composition: 2.9% clay, 23.6% silt, and 73.5% sand). The field had wheat residue. Tillage was performed using a tandem disc harrow with eight notched front discs and eight plain rear discs (Figure 5.1a). The concave sides of front discs and rear discs were in opposite directions. The disc spacing (S_h) was 190 mm and the total working width (W_h) of the harrow was 1520 mm. The disc gang angle (β) was 20° and the disc diameter was 460 mm (Figure 5.1b).

5.3.1.2 Experimental Design

A completely randomized design was used in this experiment. The treatments were disc harrow tillage directions: perpendicular and parallel to the standing wheat stubble rows, named as Perp-Direction and Para-Direction, respectively (Figure 5.1c). Prior to the tillage, most of the lying flat residue were removed to minimize the effects of lying flat residue. Each treatment was replicated four times, giving eight test runs. The plot for each test run was 1.5 m wide and 50 m long,

accommodating for one pass of the harrow. The disc harrow was operated at fixed travelling speed (4 km h^{-1}) and working depth (100 mm) for both treatments.

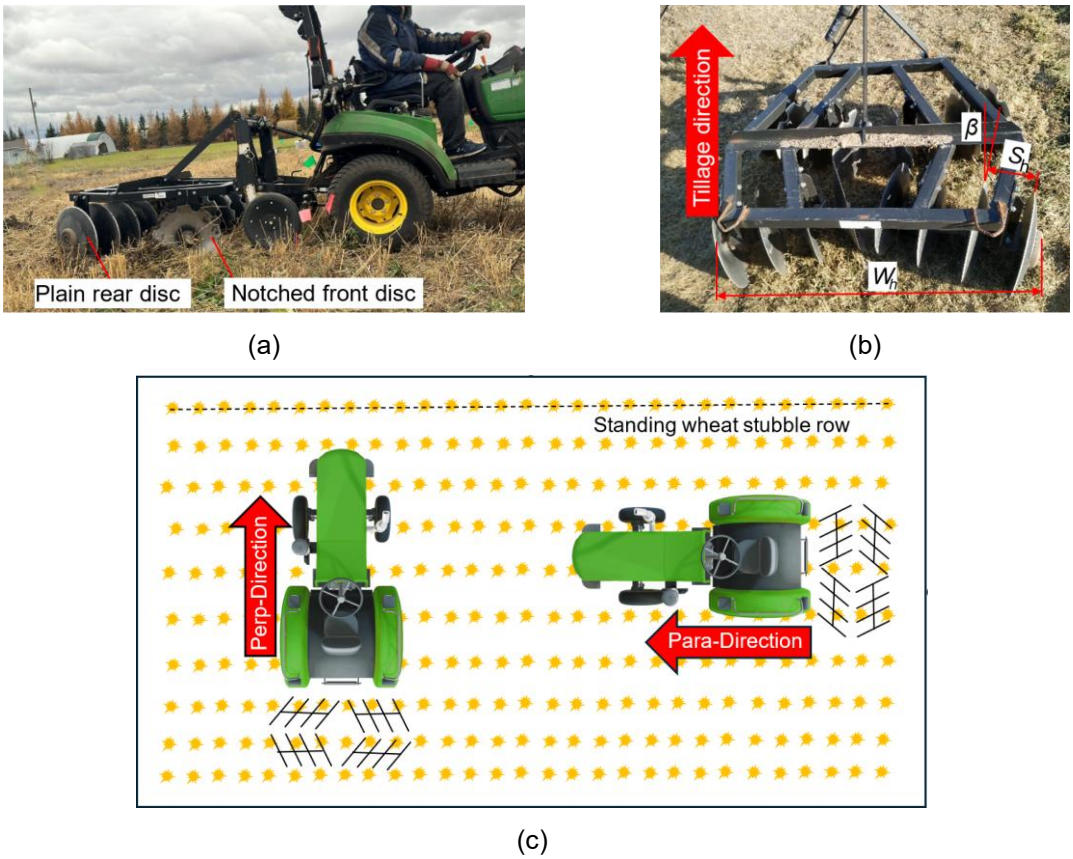

Figure 5.1. Field experiment setup: (a) the tandem disc harrow; (b) parameters of disc harrow: total working width (W_h), disc spacing of harrow (S_h), and disc gang angle (β); and (c) illustration of tillage directions: disc harrow travelling perpendicular or parallel to the standing wheat stubble rows, i.e. Perp-Direction or Para-Direction treatments respectively.

5.3.2 Measurements

5.3.2.1 Initial Soil Properties and Characteristics of Standing Wheat Stubble

Before tillage, soil samples were collected randomly at five locations of the field using a core sampler (51.5 mm diameter and 98.6 mm high). The oven-dried method was used to obtain the soil moisture content (gravimetric) and soil bulk density (dry basis) (ASABE Standards, 2020).

The characteristics of standing wheat stubble were measured in the area defined by a 600 × 600 mm quadrat (Figure 5.2a). Within this measured area, standing stubble row spacing, wheat stubble height, and wheat stubble diameter were measured. Then, the standing wheat stubbles were cut at the soil surface, collected and oven dried (55 ℃ for 72 hours). The dry mass of the sanding stubble per hectare was determined. These measurements were repeated at five random locations of the field before tillage.

5.3.2.2 Soil Surface Residue Cover

Soil surface residue cover was measured using image analysis before and after tillage. Image of soil surface area within the quadrat (600 × 600 mm) was captured by a camera (Figure 5.2a). For image analysis, the area outside the quadrat was cropped off (Figure 5.2b). Then, the image was binarized into black-and-white image (Figure 5.2c) using a thresholding method in MATLAB. The ratio of white pixels (residue) to total pixels of the image was defined as the residue cover (Chen et al., 2004).

5.3.2.3 Forward Displacement of Standing Wheat Stubble

Tracer method was used to monitor the forward displacement of standing wheat stubble. Paper straws (200 mm long) were used as tracers, and they were labelled and inserted into soil (Figure 5.2d). Fifteen tracers were aligned in a row with a tracer spacing of 95 mm. The tracers' row was oriented perpendicular to the traveling direction of disc harrow in all plots, with the middle tracer being positioned along the centre of the disc harrow path. The tracer position was quantified using the lateral distance. The middle tracer had a lateral distance of zero, and the other tracers had lateral distances of 95, 190, 285, 380, 475, 570, and 665 mm.

Prior to tillage, two ropes (Rope A and Rope B as shown in Figure 5.2e) were positioned perpendicularly, creating a coordinate system. Rope A was aligned with the row of standing wheat stubble tracers, while Rope B was placed along the centre of the harrow path. The tracer coordinates were recorded both before and after tillage, and changes in these tracer coordinates were calculated to determine the forward displacements.

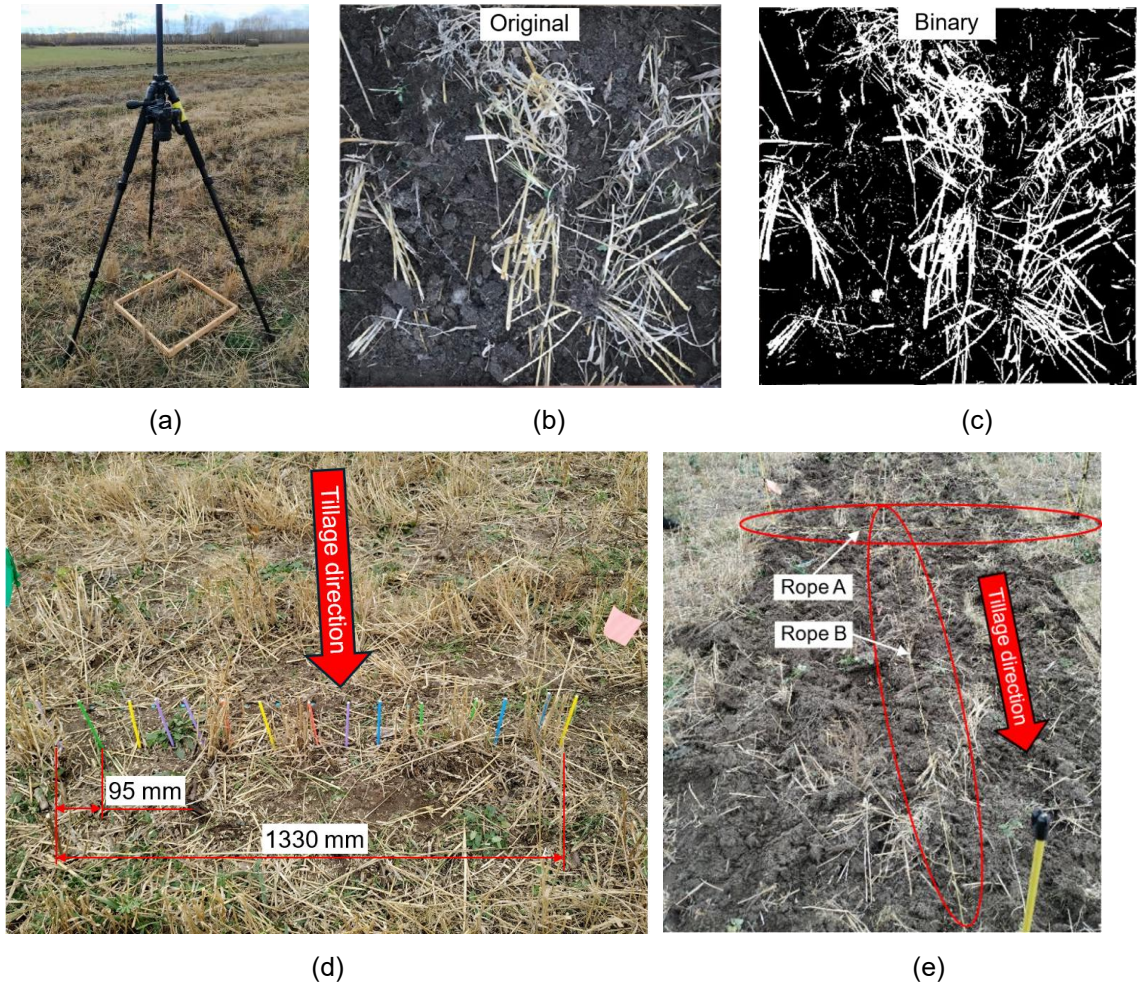

Figure 5.2. Field measurements: (a) Image taking using a camera and a 600 × 600 mm quadrat for residue cover analysis; (b) an example of images after tillage; (c) the binary image for determining the residue cover; (d) paper straw tracers for displacement measurements of standing wheat stubble; and (e) two perpendicular ropes as references for recording the coordinates of the tracers after tillage.

5.3.2.4 Data Analysis

R-Studio was used to perform the analysis of variance (ANOVA) on the measured results. The means of displacements of different tracers were compared with Duncan's multiple range test (0.05 significance). Additionally, the means of displacement and residue cover between the two tillage directions (Perp-Direction and Para-Direction) were compared with t-test (0.05 significance).

5.3.3 Tillage Model for Disc Harrow

5.3.3.1 Model Development

A commercial discrete element software, PFC^{3D} (Particle Flow Code in Three Dimensions) was used to model the tillage operation of the disc harrow. In the model, soil was represented by spherical particles, and the contact between particles were described by the Parallel Bond Model (PBM) of PFC^{3D} (Potyondy and Cundall, 2004). The PBM mimicked the cohesion of agricultural soil (Sadek and Chen, 2015). A large soil domain (2000 mm wide and 1500 mm long) was used to accommodate the pass of the disc harrow and movement of soil and crop residue. Soil particles with a 10 mm diameter were filled into the central 1000 mm of the soil domain along the harrow path, where the interactions between discs and soil/crop residue occurred. Larger particles (20 mm diameter) were filled into the two side sections (500 mm wide) (Figure 5.3a) to reduce the computing time (Zeng and Chen, 2019). Soil particles were stabilized to an equilibrium state under gravity and a local damping ratio (0.5). The soil surface was levelled by removing the soil particles exceeding 200 mm in height. The final soil domain had 367,171 soil particles.

To replicate the field condition, wheat residues were created on the soil surface. For the two tillage direction treatments: Perp-Direction and Para-Direction, wheat stubble rows were arranged to be perpendicular (five rows) to (Figure 5.3a) and parallel (four rows) to (Figure 5.3b) the

traveling direction of the disc harrow in the model. Both orientations included some lying flat residue on the soil surface.

The model wheat residue was formed using the Rblock feature in PFC^{3D}. Each residue piece was a rigid cylinder. The diameter of the model residue was 3.62 mm, the length was 210 mm, and the density was calculated as 148.7 kg m^{-3}, based on the measurements in the field experiment. To replicate the same masses of wheat residue as measured in the field, the model included a total of 345 standing wheat stubbles (blue residue in Figure 5.3) randomly standing in the stubble rows, and a total of 1,200 lying flat residues (orange residue in Figure 5.3) randomly placed within the stubble rows. Wheat residues were stabilized using a local damping ration of 0.75. Wheat residue contacted with soil and disc harrow through the linear contact model of PFC^{3D} (Zeng and Chen, 2019).

Due to the symmetric feature of the tandem disc harrow, the harrow was simplified to a half configuration, consisting of four front notched discs and four rear plain discs in the same layout as the real harrow. The modelled discs were created in SolidWorks and imported into the PFC^{3D} software. Desired working depth and travelling speed were assigned to each of the discs. The rotation speed of disc was calculated using the travelling speed and the diameter of the disc (Murray and Chen, 2018).

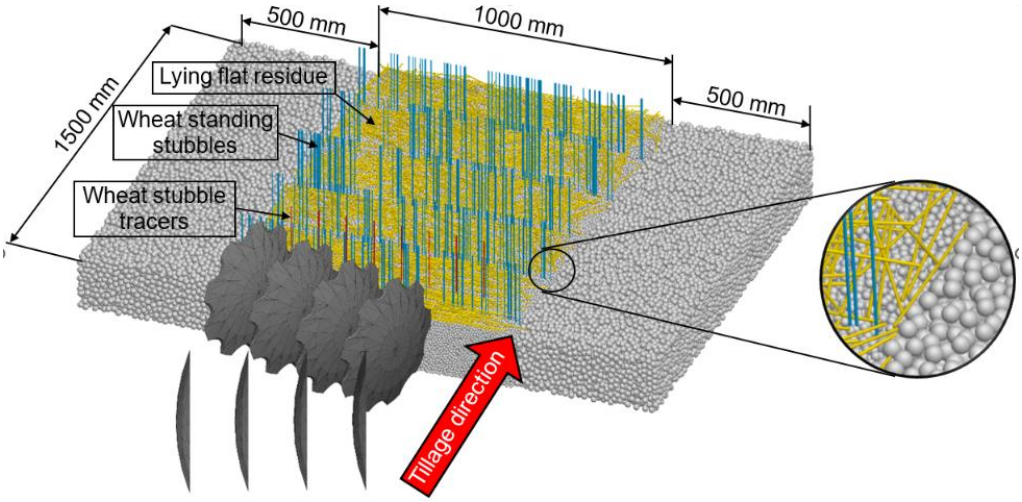

(a)

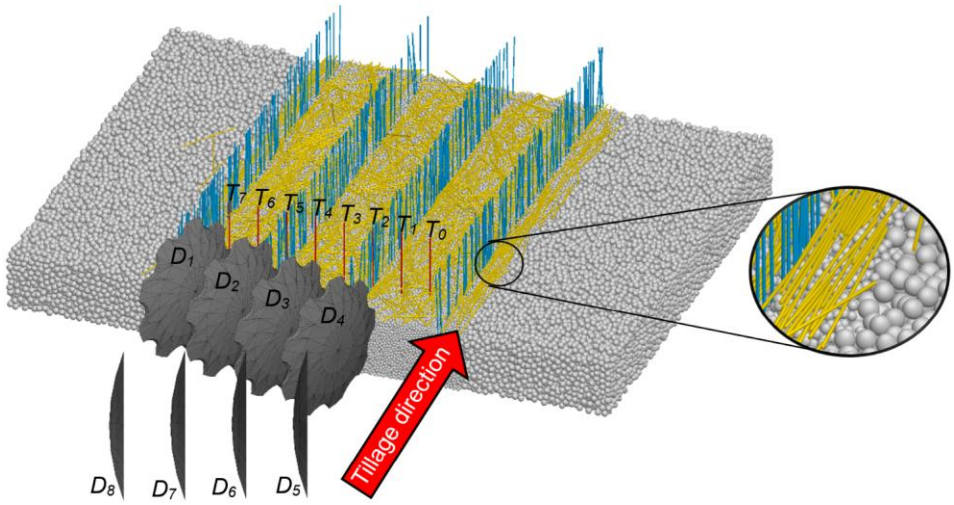

(b)

Figure 5.3. The disc harrow tillage models: (a) harrow travelling perpendicular to the standing wheat stubble rows (Perp-Direction); and (b) harrow travelling parallel to the standing wheat stubble rows (Para-Direction). Disc numbering (D_1, D_2, D_3, and D_4 were the front notched discs, D_5, D_6, D_7, and D_8 were the rear plain discs) and model tracers (T_0 to T_7) for monitoring purposes.

Model inputs included parameters for soil, disc harrow, wheat residue, and contacts between them. These model parameters were adopted from Zeng and Chen (2019), who developed a straw-sweep-soil interaction model using the same soil type and a cereal straw. The parameters are summarised in Table 5.1.

Table 5.1. Summary of model parameters; source (Zeng and Chen, 2019).

Property	Symbol	Value
Wall normal stiffness, N m^{-1}	$k_{n\text{-}wall}$	1e8
Wall shear stiffness, N m^{-1}	$k_{s\text{-}wall}$	1e8
Wall friction coefficient	$\mu_{\text{-}wall}$	0.5
Soil normal stiffness, N m^{-1}	$k_{n\text{-}soil}$	8.73e3
Soil shear stiffness, N m^{-1}	$k_{s\text{-}soil}$	8.73e3
Soil friction coefficient	$\mu_{\text{-}soil}$	0.36
Soil particle density, kg m^{-3}	$\rho_{\text{-}soil}$	2650
Soil bond radius multiplier	$\lambda_{\text{-}soil}$	0.5
Soil bond normal stiffness, Pa m^{-1}	$\overline{k_n}_{\text{-}soil}$	4.95e7
Soil bond shear stiffness, Pa m^{-1}	$\overline{k_s}_{\text{-}soil}$	4.95e7
Soil bond tensile strength, Pa	$\sigma_{\text{-}soil}$	3.82e4
Soil bond cohesion, Pa	$c_{\text{-}soil}$	1.39e4
Wheat residue normal stiffness, N m^{-1}	$k_{n\text{-}residue}$	332
Wheat residue shear stiffness, N m^{-1}	$k_{s\text{-}residue}$	332

5.3.3.2 Model Validation

For model validation, surface residue cover and forward displacement of standing wheat stubble were simulated using the model and then were compared with the field measurements. The agreement was assessed using the overall relative error.

During the simulation, disc harrow travelled at the same speed (4 km h^{-1}) and depth (100 mm) as in the field experiment. After tillage, the resultant residue cover was quantified using the same image analysis method as in the field experiment. Forward displacement of standing wheat stubble was also determined using the tracer method. Model tracers were positioned 10 mm apart on the soil surface, namely T_0, T_1, T_2, T_3, T_4, T_5, T_6, and T_7, perpendicularly aligned to the tillage direction

(red residue in Figure 5.3b). The T_0 and T_7 were located at the harrowed edges. The trajectories of standing wheat stubble tracers were monitored in the simulation, and the forward displacement was determined at the steady states of the tracers.

5.3.3.3 Model Applications

The model was used to examine effects of different operational parameters on some dynamic attributes soil and residue. The operational parameters included disc gang angles (β) (10°, 15°, and 20°), travelling speeds (V) (5, 9, 13 km h^{-1}), and working depths (D) (50, 75, and 100 mm). For this application, only one operational parameter was changed at a time, and other parameters remained constant. The constant values of β, V, and D were 20°, 13 km h^{-1}, and 100 mm respectively.

The resultant dynamic attributes monitored include soil cutting forces and soil disturbance characteristics, as described below. The time of each simulation was approximately 25 hours (varying with different travelling speeds) using a Dell Workstation with 192 GB RAM, a 2.10 GHz Intel (R), and Xeon (R) Silver 4110 CPU (2 processors). The default timestep (approximately 5e-6 s) that was automatically calculated was used throughout simulations.

The soil cutting forces on each individual disc, which is difficult to measure in practice, were predicted using the model. To track the performance of individual discs, discs were numbered from D_1 to D_8 in the sequence in which they engaged with the soil, as shown in Figure 5.3b. The soil cutting forces tracked were draft force (F_D), lateral force (F_L), and vertical force (F_V). Using these forces, the force imbalance ratio (I) was determined to measure the force variation among the discs, which is an important indicator of the disc stability. A larger I indicate greater interferences between discs in a disc implement. The I was calculated by:

$$I = \frac{1}{8}\left(\sum_{i=1}^{8}\frac{1}{3}\left(\frac{\max|(F_D)_i| - \min|(F_D)_i|}{\max|(F_D)_i|} + \frac{\max|(F_L)_i| - \min|(F_L)_i|}{\max|(F_L)_i|} + \frac{\max|(F_V)_i| - \min|(F_V)_i|}{\max|(F_V)_i|}\right)\right) \quad (5.1)$$

where I = force imbalance ratio, F_D = draft force of a disc (N), F_L = lateral force of a disc (N), F_V = vertical force of a disc (N), i = ith number of disc.

Soil disturbance characteristics were quantified using soil surface roughness, furrow bottom roughness, soil disturbance area (A_h), and soil cutting efficiency (η). After tillage, the soil surface profile and furrow bottom profile were extracted within the total working width of disc harrow (W_h), and the fluctuations (standard deviations) of the profiles were defined as soil surface roughness or furrow bottom roughness (Figure 5.4). The soil disturbance area (A_h) defined in Figure 5.4 was determined using image analysis.

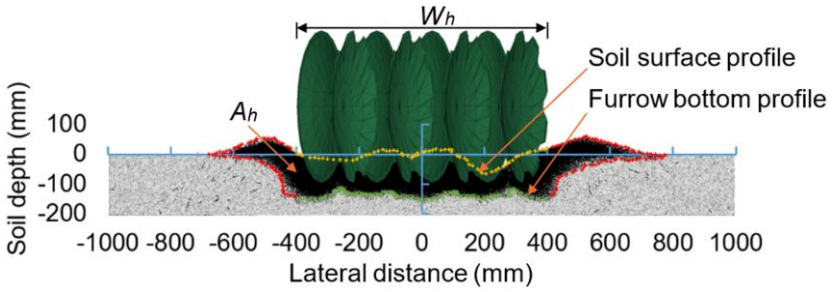

Figure 5.4. Model screenshot showing the soil cross-section after tillage, illustrating soil disturbance characteristics; A_T = soil disturbance area, W_h = total working width of the harrow.

The total draft of harrow (F_t) was calculated as the sum of F_D of all eight discs. This variable is an important performance indicator, as it determines the power requirement of the harrow and in turn the drawbar power required from the tractor. Another performance indicator is the soil disturbance area (A_h), reflecting amount of work done by the harrow. Considering both F_t and A_h, a soil cutting efficiency (η) (McKyes, 1985) was used as an overall performance indicator of harrow, and it was defined as the following:

$$\eta = \frac{A_h \times d_h}{F_t \times d_h} \quad (5.2)$$

where η = soil cutting efficiency ($mm^3\ J^{-1}$), A = soil disturbance area (mm^2), F_t = total draft of harrow (N), d_h = travel distance of harrow (mm). The ratio of disturbed soil volume per hectare to the η was converted into energy requirement per hectare. This approach was commonly adopted in tillage energy analyses (Godwin, 2007)

5.4. Results and Discussion

5.4.1 Experiment Results

5.4.1.1 Initial Soil and Residue Condition

Table 5.2 presents the measured results of initial soil and residue conditions. The average soil moisture content and soil bulk density of the field were typical for this soil type (Dam et al., 2005). Before tillage, the field had an average standing wheat stubble of 735.6 kg ha^{-1} (dry mass), slightly lower than the typical value (Kushwaha et al., 1986a; 1986b). The characteristics of standing wheat stubble are listed in Table 5.2, and they were used for developing the model.

Table 5.2. Initial soil conditions and characteristics of standing wheat stubble.

Measurement	Mean	Standard deviation
Soil moisture content, %	21.8	2.3
Soil dry bulk density, kg m^{-3}	1187.0	48.8
Standing wheat stubble dry mass, kg ha^{-1}	735.6	134.9
Single standing wheat stubble dry mass, g	0.32	0.08
Standing wheat stubble row spacing, mm	285	30
Standing wheat stubble height, mm	210	50
Standing wheat stubble diameter, mm	3.62	0.17

5.4.1.2 Measured Forward Displacement of Standing Wheat Stubble

Overall, the forward displacement of standing wheat stubble was quite large (Figure 5.5). The greatest stubble displacement did not occur at the centre of the harrow path, due to the tandem arrangement of disc gangs. When the harrow travelled in perpendicular to the stubble rows (Perp-Direction) (Figure 5.5a), the greatest stubble forward displacement was observed at the lateral distance of 190 mm from the centre of the harrow path, where stubble was moved as much as 484 mm. For the further lateral distances, the stubble forward displacements were reducing by 50% at the 570 mm or 665 mm lateral distances. When the harrow travelled in parallel to the stubble rows (Para-Direction) (Figure 5.5b), the greatest stubble forward displacement was observed at the lateral distance of 95 mm from the centre of the harrow path, where stubble was moved forward over 550 mm. Stubble forward displacements were quite variable in either treatment. No statistical differences were observed along the lateral distances from the centre of the harrow path. The reasons for this trend might be attributed to the complex effects of overlapping passes of two disc

gangs and its interaction with stubble rows. This further demonstrates the necessity of studying an entire tillage implement, rather than individual tillage tools as existing studies focused on.

If forward displacements of standing wheat stubble were averaged over all the lateral distance, Para-Direction had an average of 371 mm, which was 8.1% larger than that that of Perp-Direction. There were no statistically significant differences in the average forward displacement between Perp-Direction and Para-Direction.

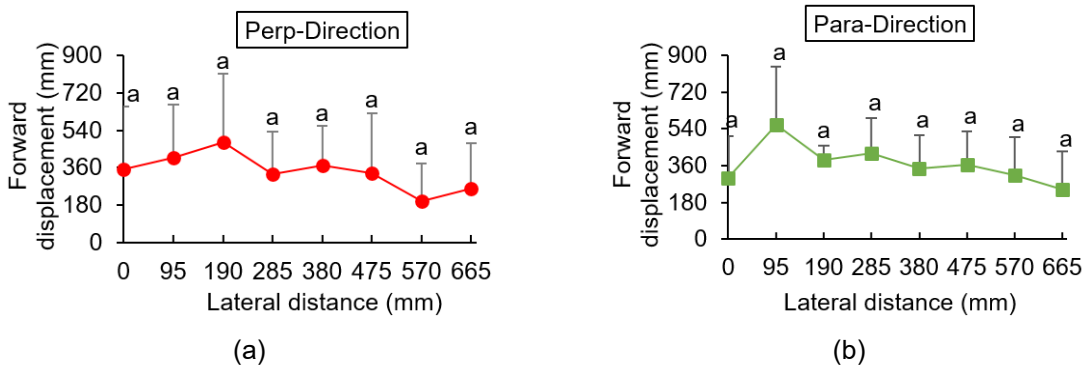

Figure 5.5. Measured forward displacement of standing wheat stubble over the lateral distance from the centre of the harrow path: (a) Perp-Direction and (b) Para-Direction (two tillage directions: harrows traveling perpendicular and parallel to the standing wheat stubble rows respectively). Means followed by same letters were insignificantly different according to Duncan's multiple range test (significance 0.05); error bars are standard deviations.

5.4.1.3 Measured Surface Residue Cover

The field initially had a surface residue cover of 45.7%. After tillage, the residue cover decreased by 38.1% under Para-Direction (Figure 5.6a) and 48.8% under Perp-Direction (Figure 5.6b). Statistical analysis showed that the residue cover under Para-Direction was significantly larger than that under Perp-Direction. This confirmed that tillage direction influences the reduction in residue cover. Under Para-Direction, the discs tended to push the standing wheat stubble to the sides along the row lines, rather than thoroughly mixed standing wheat stubble into the soil.

However, when the disc harrow travelled perpendicularly across the standing wheat stubble rows, the discs interacted more aggressively with the standing stubble, resulting in better mixing with the soil. Choosing an appropriate tillage direction depends on the desired level of residue incorporation.

5.4.2 Model Validation

The model prediction accuracy was validated by comparing simulations and measurements in the average forward displacement of residues and average residue cover. The simulated average forward displacements of standing wheat stubble were 282 mm and 281 mm for Perp-Direction and Para-Direction respectively, which underpredicted the displacements compared with the measurements (Figure 5.6a). The simulated residue cover under Perp-Direction and Para-Direction were 27.4% and 34.0% respectively, which overpredicted residue covers compared with the measurements (Figure 5.6b). The corresponding relative errors were 17.1% for Perp-Direction and 20.1% for Para-Direction. The overall relative error for the two variables was 19.7%, which showed that the model had an acceptable prediction accuracy.

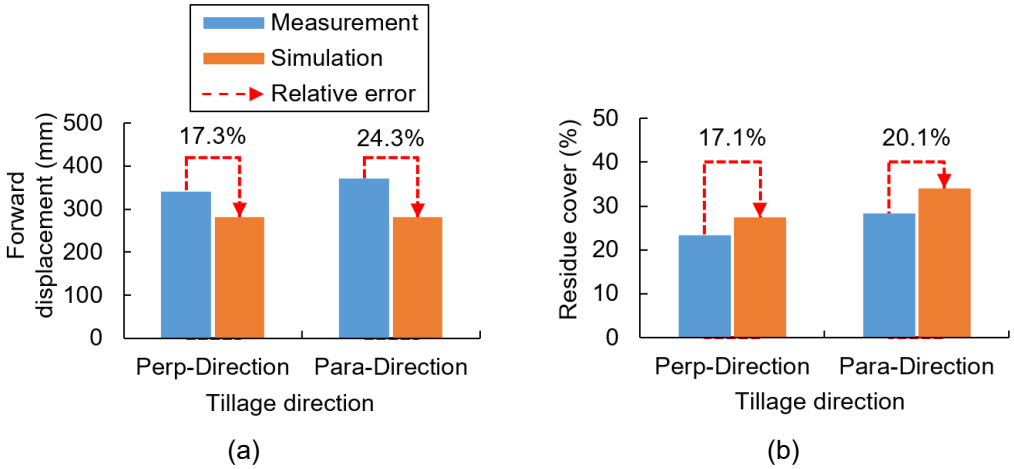

Figure 5.6. Comparisons between experimental and simulation results and relative error between them: (a) forward displacement of standing wheat stubble and (b) surface residue cover. Perp-Direction and Para-Direction are two tillage directions: the harrow traveling perpendicular and parallel to the standing wheat stubble rows respectively.

5.4.3 Model Applications

5.4.3.1 Simulated Dynamic Behaviours of Soil and Residue

Amount of soil disturbed by a disc can be visualized by the particle velocity contour (Figure 5.7a). Disc D_1 was the first that interacted with soil and residue among all other discs, resulting in the least amount of disturbed soil. The soil disturbed by discs D_2, D_3, and D_4 were extended to the adjacent discs, meaning an appropriate disc spacing that did not leave undisturbed soil between discs. The rear discs displaced the soil in opposite lateral directions. The soil regions disturbed by disc D_7 and D_8 reached to the adjacent discs. However, the disc D_6 was unexpectedly smaller. As the front disc D_4 and rear disc D_5 displaced the soil in the opposite directions, a trench was formed between discs D_4 and D_5. It is interesting to see that disc D_6 pushed less soil than discs D_7 and D_8.

The residue displacement contour is shown in Figure 5.7b. As the harrow travelled, the four front discs laterally throwed the wheat residue, thus creating four residue flow streams. The residue

flow stream created by each of discs D_2, D_3, and D_4 was split into two smaller residue flow streams by discs D_8, D_7, and D_6 respectively, as illustrated in Figure 5.7b. This scenario showed the close "cooperation" between the front row discs and rear row discs for even distributions of residue in the field. A residue flow stream was also formed at each side of the harrow along the edges (i.e. by discs D_1 and D_5), but these two flow streams did not undergo a splitting.

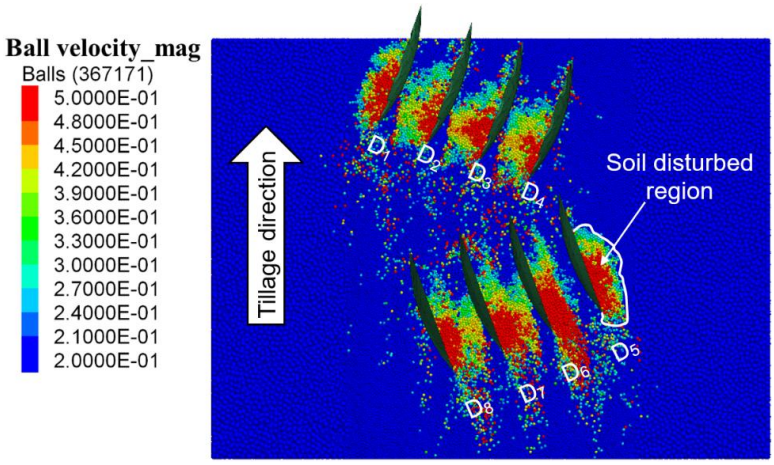

(a)

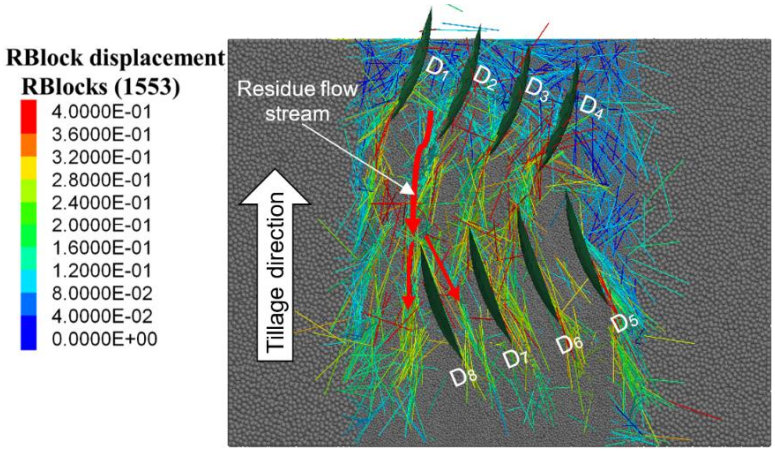

(b)

Figure 5.7. Particle contours: (a) velocity (unit: m s^{-1}) of soil particles and (b) displacement (unit: m) of wheat residues resulting from the harrow. D_1, D_2, D_3, and D_4 are the front notched discs, and D_5, D_6, D_7, and D_8 are the rear plain discs. Disc harrow: travelling perpendicular to the wheat stubble rows (Perp-Direction), travelling speed = 4 km h^{-1}, working depth = 100 mm, and disc gang angle = 20°.

5.4.3.2 Simulated Trajectories of Standing Wheat Stubble

The trajectories in three directions were monitored for each of the stubble tracers (labelled as T_0 to T_7 shown in Figure 5.3b) at different lateral distances from the centre of the harrow path. The forward trajectories (red lines in Figure 5.8) demonstrated that standing wheat stubble consistently moved away from its initial position as the disc harrow advanced forward, regardless of its lateral distance from the centre of the harrow path, with the tracers at the harrowed edges (T_0 and T_7) being moved the least forward distance (Figure 5.8a and 5.8h). Laterally, wheat stubbles at harrowed edges (T_0 and T_7) were displaced beyond the working width of the harrow (green lines in Figure 5.8a and 5.8h), while the rest of stubbles (T_1 to T_6) were displaced left or right (green lines in Figure 5.8b-g). The vertical trajectories showed that some stubbles were continuously pushed down to the deeper soil (T_0, T_2, T_3, and T_6) (blue lines in Figure 5.8a, 5.8c, 5.8d, 5.8g), some were brought up above the soil surface level (T_4 and T_5) (Figure 5.8e and 5.8f), and some moved up and then down the surface level (T_1 and T_7) (Figure 5.8a and 5.8h). The results of vertical trajectories suggested that significantly amount of wheat residue were pushed downward and buried into soil.

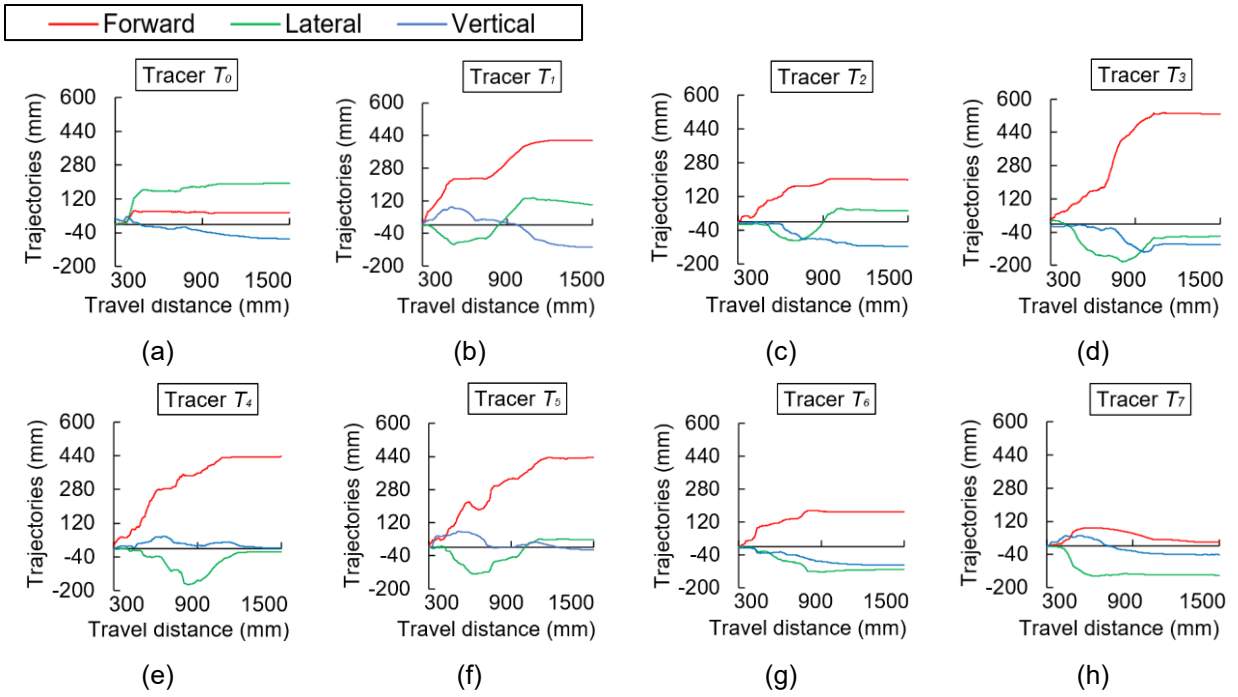

Figure 5.8. The trajectories (in forward, lateral, and vertical directions) of standing wheat stubble over the harrow travel distance: (a) Tracer T_0; (b) T_1; (c) T_2; (d) T_3; (e) T_4; (f) T_5; (g) T_6; and (h) T_7. Disc harrow: travelling perpendicular to the wheat stubble rows (Perp-Direction), travelling speed = 4 km h^{-1}, working depth = 100 mm, and disc gang angle = 20°.

5.4.3.3 Simulated Soil Cutting Forces of Individual Discs

Soil cutting forces in three directions simulated for eight individual discs (D_1 to D_8) are shown in Figure 5.9. Over the travel distance, the increases in the forces at the beginning and the decrease at the end represent the discs entering and leaving the soil respectively. Thus, the following discussion focuses on the constant forces in the middle section of the travel distance. Results showed that the soil cutting forces were not evenly distributed among individual discs, depending on types (notched or plain) of disc and the position of the disc on the harrow within the same type of disc.

Disc D_1 was the leading disc of harrow, and it interacted with the largest amount of undisturbed soil, resulting in the highest draft force (F_D) (blue line in Figure 5.9a) and lateral force (F_L) (orange line in Figure 5.9a). Discs D_2, D_3, and D_4 had similar F_D and F_L (Figure 5.9b-d). Therefore, the interference between these three discs led to a reduction in the F_D and F_L of each individual disc.

As expected, the values of F_L for the rear discs were in opposite directions of those for the front disc, which allowed the lateral forces to be cancelled, favouring the stability of the harrow. Rear discs D_5, D_6, D_7, and D_8 had slightly lower F_D and F_L (Figure 5.9e-h), compared with the front discs, as the formers worked on the loosened soil disturbed by the latter discs. This explains why a mirrored half harrow was indeed necessary for balancing the lateral force of a tandem disc harrow. However, not all lateral forces of individual discs were cancelled out completely in this particular harrow. The total lateral force of the harrow was 40.7 N, rather than 0 N, due to the different in disc types between front and rear discs. The other reason was that the front discs interacted with untilled soil while the rear discs interacted with soil that had already been tilled by the front discs. Vertical forces (F_V) (purple line) of discs were low, near zero or slightly above zero. Only disc D_5 had a negative F_V (-27.1 N) (Figure 5.9e), indicating a downward vertical force.

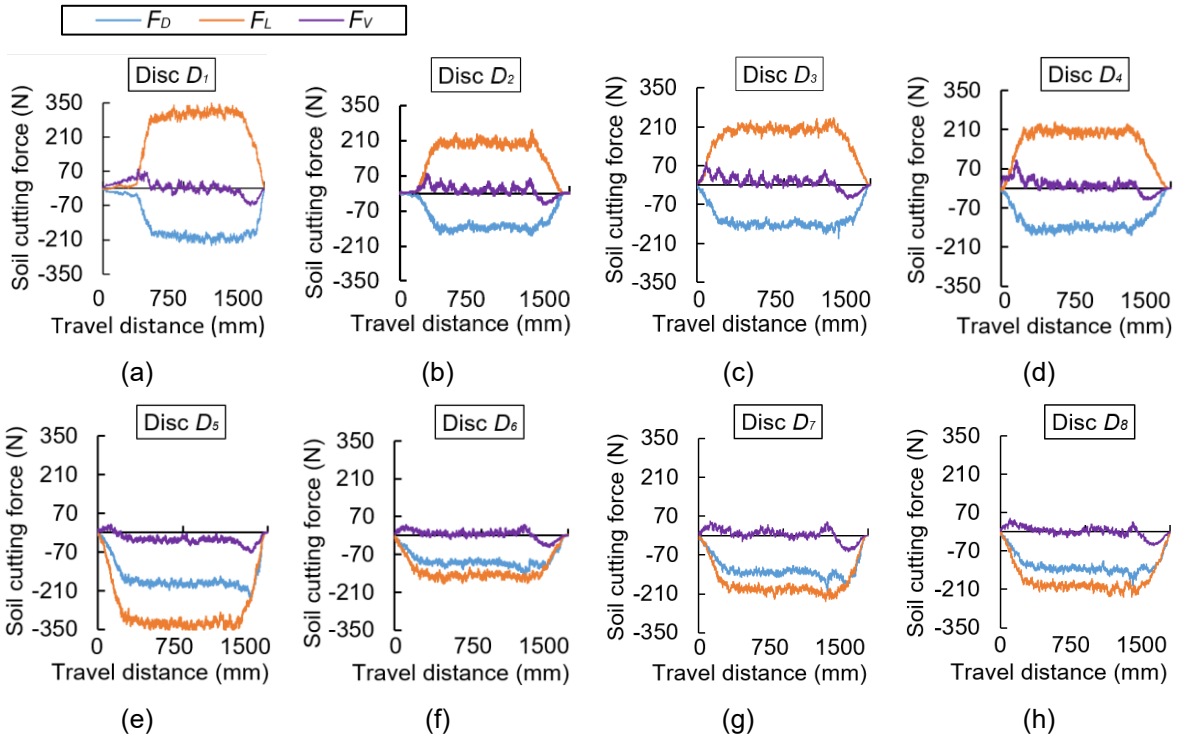

Figure 5.9. Soil cutting forces, including draft force (F_D), lateral force (F_L), and vertical force (F_V) of individual discs over the harrow travel distance: (a), (b), (c), and (d) the 1st, 2nd, 3rd, and 4th front notched discs (D_1, D_2, D_3, and D_4) respectively; (e), (f), (g), and (h) the 5th, 6th, 7th, and 8th rear plain discs (D_5, D_6, D_7, and D_8) respectively. Disc harrow: travelling perpendicular to the wheat stubble rows (Perp-Direction), travelling speed = 4 km h^{-1}, working depth = 100 mm, and disc gang angle = 20°.

Force imbalance ratios (I) determined using Eq. (5.1) from the soil cutting forces of individual discs showed that variations of the I was different in terms effects of the operating parameters. Varying β would cause complex changes in soil cutting forces due to the complex nature of the interaction between the disc concave and gang angle. Thus, effects of β had different trends between Para-Direction and Perp-Direction (Figure 5.10a). The 15° of β had lower I for Perp-Direction, while the 10° of β had lower I for Para-Direction. The trends of effects of V were more predictable between Perp-Direction and Para-Direction. A lower I was found at a higher V (Figure 5.10b), indicating that an increased V helps balance the soil cutting forces. The lowest I was obtained when the harrow worked at 75 mm depth for both tillage directions (Figure 5.10c).

Varying in *D* primarily influences the contact area between the disc harrow and soil/wheat residue, resulting in consistent trends of *I* between the two tillage directions. Overall, the harrow was more balanced or stable when working at 15° disc gang angle, 13 km/h travelling speed, and 75 mm working depth.

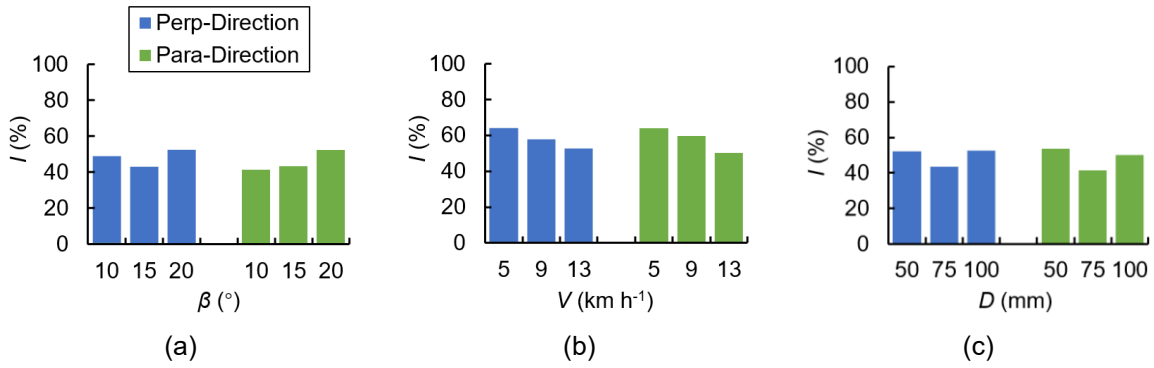

Figure 5.10. Simulated force imbalance ratios (*I*) under different operational parameters of harrow: (a) disc gang angles (*β*), with fixed travelling speed of 13 km h^{-1} and working depth of 100 mm; (b) travelling speeds (*V*), with fixed disc gang angle of 20° and working depth of 100 mm; and (c) working depths (*D*), with fixed disc gang angle of 20° and travelling speed of 13 km h^{-1}. Perp-Direction and Para-Direction are two tillage directions: the harrow traveling perpendicular and parallel to the standing wheat stubble rows respectively.

5.4.3.4 Simulated Soil Roughness

Soil surface roughness was similar between Perp-Direction and Para-Direction. In both tillage directions, soil surface roughness consistently increased with an increasing of *β* (Figure 5.11a). The greatest change in soil surface roughness resulted from variations in the *β*, showing an 57.2% increase. The soil surface roughness increased from 10.3 to 25.4 mm as the *β* increased from 10° to 20° on average over the two tillage directions. The *V* had the less impact on the soil surface roughness, and lower *V* cause lower soil surface roughness (Figure 5.11b). An increasing trend was also found for the effects of *D* (Figure 5.11c). In practice, soil surface roughness is maintained at either a high value for reducing soil erosion (Zhou et al., 2023), or a low value for a smooth

seedbed (Chen et al., 2023). Therefore, the harrow operational parameters should be adjusted for suiting the specific tillage practice.

Compared to the soil surface roughness, the furrow bottom roughness was much lower in all cases. Also, furrow bottom roughness showed less variation with the operational parameters (β, V, and D). There were no obvious differences in furrow bottom roughness between Para-Direction and Perp-Direction. Furrow bottom roughness was the highest for the β of 15° for both tillage directions (Figure 5.11d). The effects of V (Figure 5.11e) and D (Figure 5.11f) had no particular trends. Lower bottom roughness is more desirable for plant growth. Thus, the recommended operational parameters are β = 10°, V = 9 km h^{-1}, and D = 75 mm for Perp-Direction and β = 20°, V = 13 km h^{-1}, and D = 100 mm for Para-Direction.

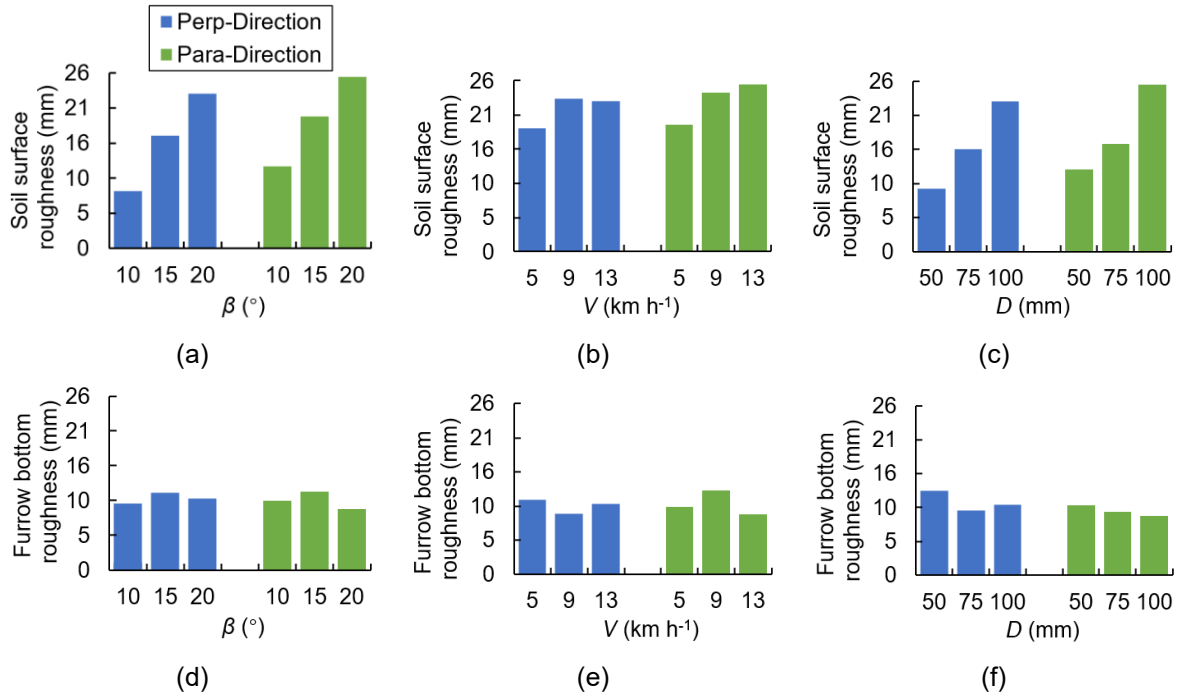

Figure 5.11. Simulated soil roughness resulting from the harrow: (a), (b), and (c) soil surface roughness for different disc gang angles (β) with fixed travelling speed of 13 km h^{-1} and working depth of 100 mm, travelling speeds (V) with fixed disc gang angle of 20° and working depth of 100 mm, and working depths (D) with fixed disc gang angle of 20° and travelling speed of 13 km h^{-1} respectively; and (d), (e), and (f) furrow bottom roughness. Perp-Direction and Para-Direction are two tillage directions: the harrow traveling perpendicular and parallel to the standing wheat stubble rows respectively.

5.4.3.5 Simulated Soil Cutting Efficiency of the Harrow

Soil cutting efficiency (η) of harrow depends on the total draft (F_t), and total soil disturbance area (A_h) as defined in Eq. (5.2). Variables F_t and A_h were simulated using the model. The results of F_t demonstrated overall consistency between the two tillage directions. The F_t increased linearly for both Perp-Direction and Para-Direction with an increasing of disc gang angle (β) (Figure 5.12a). Similar increasing trends were observed for the effects of the travelling speed (V) and working depth (D) (Figure 5.12b and 5.12c). The increasing trends under varying β, V, and D were consistent with the findings of a previous study on a single concave disc (Sadek et al., 2021).

Regardless of the tillage directions, the soil disturbance area (A_h) consistently increased with increasing of the disc gang angles (β), travelling speeds (V), and working depths (D). The disc harrow experienced an average of 18.9% higher A_h at a β of 20° compared to that at 10° (Figure 5.12d), possibly because of the larger working width associated with a larger β (Zeng and Chen, 2018). The A_h at the V of 13 km h^{-1} was 18.7% larger for Perp-Direction and 20.7% larger for Para-Direction, than those at the V of 5 km h^{-1} (Figure 5.12e). Effects of D on A_h was more pronounced. The A_h was increased by 47.9% for Para-Direction and 43.3% for Perp-Direction when the D changed from 50 to 100 mm (Figure 5.12f)

As discussed about, the F_t increased with the increase in β, V, and D. So did the A_h. But the soil cutting efficiency (η) decreased (Figure 5.12g-i), due to the lower increase rate of the A_h compared with that of F_t. Effects of V on η were more pronounced than those of β and D. Para-Direction had slightly higher values of η than Perp-Direction. On average, the harrow resulted in a 44.2% larger η at a β of 10° compared to 20° (Figure 5.12g), while the η at a V of 5 km h^{-1} was more than twice as large as at a V of 13 km h^{-1} (Figure 5.12h). The η decreased from 60.6 to 37.3 mm^3 J^{-1} in Perp-Direction and from 62.2 to 40.1 mm^3 J^{-1} in Para-Direction, with an increasing of D (Figure 5.12i).

Zeng et al. (2019) reported a larger magnitude of efficiency than this study and an increasing trend as the D increased, which was contrary to this study. The differences between the two studies were due to the differences in the tilt angle of disc that affect the total draft and soil disturbance area of the disc. In other tillage contexts, such as subsoiling practices, it is desired to have greater soil disturbance area (Wang et al., 2023), which improves soil cutting efficiency for being cost-effective. Whereas in conservation tillage, minimum soil disturbance is desired, which sacrifices soil cutting efficiency (Hayes and Itri, 1985) for protecting the soil.

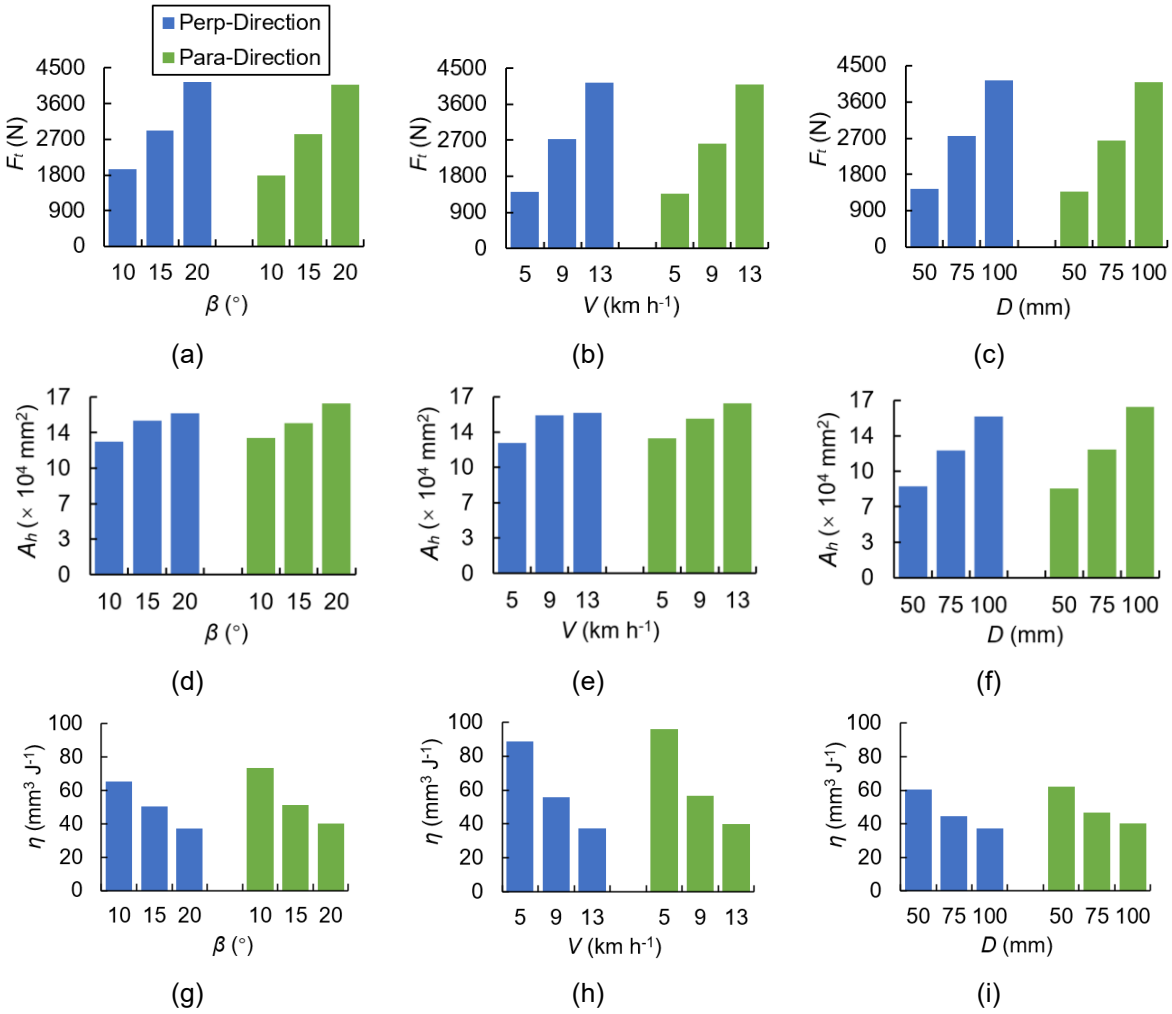

Figure 5.12. Simulated performance indicators of the harrow: (a), (b), and (c) total draft of harrow (F_t) for different disc gang angles (β) with fixed travelling speed of 13 km h^{-1} and working depth of 100 mm, travelling speeds (V) with fixed disc gang angle of 20° and working depth of 100 mm, and working depths (D) with fixed disc gang angle of 20° and travelling speed of 13 km h^{-1} respectively; (d), (e), and (f) soil disturbance area (A_h); and (g), (h), and (i) soil cutting efficiency (η). Perp-Direction and Para-Direction are two tillage directions: the harrow traveling perpendicular and parallel to the standing wheat stubble rows respectively.

5.5. Conclusions

A tillage model of a tandem disc harrow was developed using the discrete element method (DEM) and validated with field measurement data. The model was employed to simulate the

dynamics of wheat stubble and soil under two tillage directions and a range of operational parameters: disc angle (10° to 20°), traveling speed (5 to 13 km h^{-1}), and working depth (50 to 100 mm).

The model accurately predicted the forward displacement of standing wheat stubble and the residue cover on the soil surface. Tillage direction significantly influenced the residue cover but had minimal effect on the forward displacement of stubble. These variables were more accurately predicted for the tillage direction perpendicular to the wheat stubble rows (Perp-Direction) than for the parallel direction (Para-Direction). Simulation results revealed variation in soil dynamics among individual discs on the harrow. The leading disc disturbed the least amount of soil but experienced the highest soil cutting forces (both draft and lateral). Discs positioned at the harrow's outer edges contributed the least to forward displacement of stubble. Balanced soil cutting forces across all discs were observed when the harrow operated at a 15° disc angle, a traveling speed of 13 km h^{-1}, and a working depth of 75 mm. Lowering these operational parameters helped reduce soil surface roughness regardless of tillage direction. Increasing the disc angle, speed, or working depth led to higher total draft forces and a larger soil disturbance area. However, the increase in disturbance area was not proportional to the increase in draft force, resulting in decreased soil cutting efficiency defined as the ratio of soil disturbance area to total draft force.

This study provides valuable insights into the interactions between wheat stubble, soil, and the tandem disc harrow, offering practical guidance for optimizing harrow operation to improve tillage performance. Nonetheless, the model has limitations, including the use of fixed dimensions for wheat residue and soil particles and a specific soil type (sandy loam soil). Caution should be taken when generalizing these results to other residue conditions or soil types.

5.6. Acknowledgements

This study was financially supported by Hainan Province Foreign Experts Program, China (G20250218002Y), CSC, China (202007565032), and NSERC of Canada (RGPIN-2019-05861).

5.7. References

Ahmadi, I., 2018. A draught force estimator for disc harrow using the laws of classical soil mechanics. Biosystems Engineering, 171, 52–62. https://doi.org/10.1016/j.biosystemseng.2018.04.008

ASABE Standards, 2020. ASABE Standard S633: Testing protocol for landscape irrigation soil moisture-based control technologies. American Society of Agricultural and Biological Engineers, St. Joseph, MI.

Bilbro, J. D., and Fryrear, D. W., 1994. Wind erosion losses as related to plant silhouette and soil cover. Agronomy Journal, 86(3), 550–553. https://doi.org/10.2134/agronj1994.00021962008600030017x

Chen, H., Gao, L., Li, M., Liao, Y., and Liao, Q., 2023. Effect of soil surface roughness on emergence rate and yield of mechanized direct-seeded rapeseed based on 3D laser scanning. International Journal of Agricultural and Biological Engineering, 16(3), 110–119. https://doi.org/10.25165/J.IJABE.20231603.7276

Chen, Y., Tessier, S., and Irvine, B., 2004. Drill and crop performances as affected by different drill configurations for no-till seeding. Soil and Tillage Research, 77(2), 147–155. https://doi.org/10.1016/j.still.2003.12.001

Dam, R. F., Mehdi, B. B., Burgess, M. S. E., Madramootoo, C. A., Mehuys, G. R., and Callum, I. R., 2005. Soil bulk density and crop yield under eleven consecutive years of corn with different tillage and residue practices in a sandy loam soil in central Canada. Soil and Tillage Research, 84(1), 41–53. https://doi.org/10.1016/j.still.2004.08.006

Damanauskas, V., and Janulevičius, A., 2022. Effect of tillage implement (spring tine cultivator, disc harrow), soil texture, forward speed, and tillage depth on fuel consumption and tillage quality. Journal of Agricultural Engineering (Pisa, Italy), 53(3), e1371. https://doi.org/10.4081/jae.2022.1371

Damanauskas, V., Velykis, A., and Satkus, A., 2019. Efficiency of disc harrow adjustment for stubble tillage quality and fuel consumption. Soil and Tillage Research, 194, e104311. https://doi.org/10.1016/j.still.2019.104311

Doan, V., Chen, Y., and Irvine, B., 2005. Effect of oat stubble height on the performance of no-till seeder openers. Canadian Biosystems Engineering, 47, 2.37-2.44.

Godwin, R. J., 2007. A review of the effect of implement geometry on soil failure and implement forces. Soil and Tillage Research, 97(2), 331–340. https://doi.org/10.1016/j.still.2006.06.010

Hayes, W. A., and D'Itri, F. M., 1985. Conservation tillage systems and equipment requirements. In A Systems Approach to Conservation Tillage, 1, 21–40. https://doi.org/10.1201/9781351070850-3

Hou, S., Zhu, Y., Ji, Z., Zhu, X., and Zhou, C., 2022. Design and test of elastic tooth type lateral straw clearing roller based on the straw clearing and mulching no-tillage precision planter. Sustainability (Switzerland), 14(12), e7238. https://doi.org/10.3390/su14127238

Kogut, Z., Sergiel, L., and Żurek, G., 2016. The effect of the disc setup angles and working depth on disc harrow working resistance. Biosystems Engineering, 151, 328–337. https://doi.org/10.1016/j.biosystemseng.2016.10.004

Kushwaha, R. L., Vaishnav, A. S., and Zoerb, G. C., 1986a. Performance of powered-disc coulters under no-till crop residue in the soil bin. Canadian Agricultural Engineering, 28, 85–90.

Kushwaha, R. L., Vaishnav, A. S., and Zoerb, G. C., 1986b. Soil bin evaluation of disc coulters under no-till crop residue conditions. Transactions of the ASAE, 29(1), 40–44. https://doi.org/10.13031/2013.30098

Liu, W., Su, Q., Fang, M., Zhang, J., Zhang, W., and Yu, Z., 2023. Parameters calibration of discrete element model for corn straw cutting based on Hertz-Mindlin with Bonding. Applied Sciences (Switzerland), 13(2), e1156. https://doi.org/10.3390/app13021156

McKyes, E., 1985. Soil cutting and tillage. Elsevier.

Murray, S. E., and Chen, Y., 2018. Soil bin tests and discrete element modeling of a disc opener. Canadian Biosystems Engineering, 60(1), 2.1–2.10. https://doi.org/10.7451/CBE.2018.60.2.1

Potyondy, D. O., and Cundall, P. A., 2004. A bonded-particle model for rock. International Journal of Rock Mechanics and Mining Sciences (Oxford, England: 1997), 41(8), 1329–1364. https://doi.org/10.1016/j.ijrmms.2004.09.011

Prosperi, P., Terres, J. M., Doublet, S., and Pointereau, P., 2011. Conservation agriculture effects and policy support to mitigate soil degradation in Midi-Pyrénées (France). Land Degradation and Development, 22(1), 70–83. https://doi.org/10.1002/ldr.1021

Sadek, M. A., and Chen, Y., 2015. Feasibility of using PFC3D to simulate soil flow resulting from a simple soil-engaging tool. Transactions of the ASABE, 58(4), 987–996. https://doi.org/10.13031/trans.58.10900

Sadek, M. A., Chen, Y., and Zeng, Z., 2021. Draft force prediction for a high-speed disc implement using discrete element modelling. Biosystems Engineering, 202, 133–141. https://doi.org/10.1016/j.biosystemseng.2020.12.009

Serrano, J. M., Peça, J. O., Pinheiro, A., Carvalho, M., Nunes, M., Ribeiro, L., and Santos, F., 2003. The effect of gang angle of offset disc harrows on soil tilth, work rate and fuel consumption. Biosystems Engineering, 84(2), 171–176. https://doi.org/10.1016/S1537-5110(02)00261-1

Strydhorst, S. M., Yang, R. C., Gill, K. S., and Bowness, R., 2019. Inter-row stubble seeding and plant growth regulators to improve field pea standability and production. Canadian Journal of Plant Science, 99(2), 184–198. https://doi.org/10.1139/cjps-2018-0237

Upadhyay, G., and Raheman, H., 2019. Specific draft estimation model for offset disc harrows. Soil and Tillage Research, 191, 75–84. https://doi.org/10.1016/j.still.2019.03.021

Verrell, A. G., Simpfendorfer, S., and Moore, K. J., 2017. Effect of row placement, stubble management and ground engaging tool on crown rot and grain yield in a no-till continuous wheat sequence. Soil and Tillage Research, 165, 16–22. https://doi.org/10.1016/j.still.2016.07.005

Wang, X., Zhou, H., Wang, S., Zhou, H., and Ji, J., 2023. Methods for reducing the tillage force of subsoiling tools: A review. Soil and Tillage Research, 229, e105676. https://doi.org/10.1016/j.still.2023.105676

Zeng, Z., and Chen, Y., 2018. Performance evaluation of fluted coulters and rippled discs for vertical tillage. Soil and Tillage Research, 183, 93–99. https://doi.org/10.1016/j.still.2018.06.003

Zeng, Z., and Chen, Y., 2019. Simulation of straw movement by discrete element modelling of straw-sweep-soil interaction. Biosystems Engineering, 180, 25–35. https://doi.org/10.1016/j.biosystemseng.2019.01.009

Zeng, Z., Chen, Y., and Qi, L., 2019. Soil cutting by a compact disc harrow having various disc arrangements. Transactions of the ASABE, 62(2), 429–437. https://doi.org/10.13031/trans.13106

Zeng, Z., Ma, X., Chen, Y., and Qi, L., 2020. Modelling residue incorporation of selected chisel ploughing tools using the discrete element method (DEM). Soil and Tillage Research, 197, e104505. https://doi.org/10.1016/j.still.2019.104505

Zhong, G., Li, H., He, J., Wang, Q., Lu, C., Wang, C., Tong, Z., Cui, D., and He, D., 2023. Design and test of single-disc opener for no-till planter based on support cutting. Agriculture (Switzerland), 13(8), e1635. https://doi.org/10.3390/agriculture13081635

Zhou, S., Ren, J., Chen, Q., and Zhang, Z., 2023. Dynamic change patterns of soil surface roughness and influencing factors under different tillage conditions in typical Mollisol Areas of Northeast China. Agronomy (Switzerland), 13(7), e1817. https://doi.org/10.3390/agronomy13071817

Chapter 6: DEM Simulation of Subsoiling for Soil Disturbance as Affected by Soil Layering and Working Speed *

*Published in *Smart Agricultural Technology* 7, e100385.

6.1. Abstract

Although the discrete element method (DEM) has been used to simulate soil-subsoiler interactions, the degree of soil heterogeneity along the depth profile has not been well documented. Models of a layered soil structure were developed using the DEM, and they were a heterogeneous soil model (HeS Model) with seven layers, a semi-heterogeneous soil model (SHeS Model) with three layers, and a homogeneous soil model (HoS Model) with one layer. The models simulated the soil dynamic behaviour resulting from a subsoiler travelling at speeds from 2 to 6 km h^{-1}. Simulations were compared with field measurements. Results showed that soil particles flow in front of the subsoiler formed three distinguished zones: “pushing”, “rising”, and “passive” zones, with the “pushing” zone having the highest particle velocities. Compared with the measurements, the overall relative errors of the simulated soil disturbance widths (W) within the range of working speed from 2 to 6 km h^{-1} were below 20% for all three models. Whereas the overall relative errors of the simulated soil surface flatness (F) were larger than 20% for all three models. These suggest that all three models are suitable for predicting W, but not for predicting F, if a 20% relative error was used as the judging criterion. The overall relative errors of the simulated elevated soil area (A) were 11.1%, 18.8%, and 25.7% for the HeS, SHeS, and HoS Models, respectively, which suggest that HeS Model had the highest accuracy in predicting A. This study provides critical information for determining the degree of soil heterogeneity in simulations of the dynamics of soil-subsoiler interaction.

Keywords: Subsoiler; Soil; Heterogeneity; Simulation; DEM

6.2. Introduction

Soil compaction and hardpan formation caused by frequent usage of agricultural machinery have negative influence on water infiltration, drainage, root penetration, and crop yield (Tracy et al., 2011; Nagy et al., 2018; Adnan et al., 2017). Thus, subsoiling has been used for decades to loosen compacted soil and hardpans in deep soil without aggressively disturbing the topsoil and surface residue for soil conservation purposes (Huang et al., 2017; Arvidsson and Hillerstrom, 2010). However, as compared with traditional tillage, subsoilers work at a greater depth. This means that subsoiling tools interact with a deeper soil profile consisting of a frequently tilled layer, a possible hardpan, an untilled layer, and other layers. The "critical depth" is a key term in soil tillage mechanics, referring to the maximum depth at which a tillage tool can operate effectively while creating uplift and fracture of the soil. The soil disturbance area does not significantly increase when the tillage tool operates below the "critical depth". In this scenario, the energy applied on soil is absorbed by the deep soil layer with plastic deformation.

Deep tillage is generally carried out below a "critical depth", while shallow tillage is not (McKyes, 1985). Thus, the outputs of deep tillage were distinctively different from that of shallow tillage, in terms of soil loosening and disturbance. There is absence of understanding on different soil failure patterns in heterogeneous soils under deep tillage. Therefore, this study aimed to fill these gaps through simulations of soil disturbance characteristics resulting from soil-subsoiler interaction in heterogeneous soil conditions.

Soil-subsoiler interaction research has been mainly carried out using three methods, i.e., experimental, analytical, and numerical modelling methods. The experimental methods are time-

consuming and costly with limited observations. The analytical methods rely on assumptions of soil failure patterns, and they are merely suitable for simple tool geometries. However, numerical modelling methods can overcome these drawbacks. In recent years, the discrete element method (DEM) has become a widely used numerical method for simulations of soil-subsoiler interactions. For instance, some researchers used the DEM in their bionic design of subsoilers, inspired by a variety of burrowing animals (Sun et al., 2018; Zhang et al., 2012; Wang et al., 2020). The DEM was also used to evaluate the effects of various geometric shapes of subsoiler on the resultant soil dynamic behaviours (Tong et al., 2020) and draft forces (Li et al., 2016). Huang et al. (2017) investigated the interactive effects of two subsoiling tools using the DEM and an indoor soil-bin experiment. However, most existing DEM models failed to completely reflect the complexity of soil heterogeneity along depth profile in subsoiling. Also, results from these studies focused on macro-behaviours of soil, not micro-behaviours at the soil particle level.

Soil heterogeneity refers to the spatial variability in the physical and mechanical properties of soil. This variability is affected by factors such as soil texture, moisture, and compaction (Zeng et al., 2017). The complicated soil heterogeneity along the depth profile can be characterized as a layered soil structure. Soil profile was traditionally described by a three-layer structure based on different soil bulk densities along the depth profile: top layer, hardpan, and subsoil layer (Chen and Tessier, 1997). The top layer is annually plowed to maintain a loose soil structure. The hardpan is formed by the downward force of tillage implements and the pressure of tractor wheels. The subsoil layer is an untilled layer, and its properties vary from field to field. There have been some researchers who developed DEM models to address the layered structure. For instance, three-layer models were developed in which different model parameters were assigned to represent different soil properties between the top layer, hardpan, and subsoil layer (Wang et al., 2019a; Tong et al.,

2020; Wang et al., 2021). There were also models with more layers, such as a four-layered structure (Huang et al., 2017; Huang et al., 2018) and a five-layered structure (Sun et al., 2018). The number of layers reflected the degree of the soil heterogeneity to be modelled. Models with more layers require more input parameters, thus increasing the complexity of the model. Therefore, Zeng et al. (2017) assumed that the heterogeneous soil model had a three-layer structure. However, it is necessary to further investigate whether the number of soil layers affect the accuracy of the model outputs under the same conditions. Research in this regard is lacking in literature.

Regardless of the number of soil layers in a model, each soil layer has its individual model parameters. These parameters should closely represent the soil properties to be modelled. Therefore, calibration of model parameters is important although it is challenging. Calibrations of model parameters were typically done using fundamental soil mechanical tests, such as triaxial test (Kozicki et al., 2014), angle of repose (Li et al., 2020), cone penetration test (Khosravi et al., 2020), and direct shear test (Bahrami et al., 2020; Tamas et al., 2016). A soil shear test directly performed in the field was used by Murray and Chen (2019) to calibrate a soil-opener DEM model. The advantage of the test is that it can be done in a field, which is able to better capture the heterogeneity of soil along the depth profile. Furthermore, calibration should be done separately for each layer of soil, considering the layered soil profile.

The objectives of the study were to (1) develop and calibrate a soil-subsoiler interaction model with a layered structure to mimic the soil heterogeneity along the depth profile, (2) use the model to investigate the micro-behaviours resulting from the subsoiling, and (3) compare models with varying degrees of soil heterogeneity in the resultant soil disturbance characteristics.

6.3. Methodology

6.3.1 Field Experiment

6.3.1.1 Experimental Site and Equipment Description

To serve the model development, calibration, and validation, a field experiment was conducted in June 2019 at a research farm in Portage la Prairie, Manitoba, Canada. The soil type was silty clay with 43% clay, 48% silt, and 9% sand content. The field was untilled before the experiment. A John Deere subsoiler (John Deere PS1001, Deere & Co., Moline, Illinois, USA) was used for the field experiment. The subsoiler had its own mounting frame, so that it could be mounted directly on the tractor through the three-point hitch (Figure 6.1a). The subsoiler consisted of a straight vertical shank and a sloped point with a cutting share (Figure 6.1b).

6.3.1.2 Experimental Design

The field experiment had a completely randomized design. The treatments were five working speeds of the subsoiler: 2, 3, 4, 5, and 6 km h^{-1}. The working depth of the subsoiler was 350 mm for all treatments. Each treatment was replicated five times. Thus, a total of 25 field plots were used in the experiment. The plot was 2 m wide and 10 m long to accommodate one pass of the subsoiler (Figure 6.1c). Buffer areas were set at two ends of plots for tractor acceleration and deceleration. Measurements were taken at the constant speed area between two buffer areas.

6.3.1.3 Measurements

Before subsoiling, soil properties were measured at four random locations in the field. At each location, the soil profile was divided into seven layers: *L1*, *L2*, *L3*, *L4*, *L5*, *L6*, and *L7*, corresponding to seven different soil depths: 0 – 50, 50 – 100, 100 – 150, 150 – 200, 200 – 250,

250 – 300, and 300 – 450 mm. Measurements were started on the top layer, and then this layer was removed carefully to expose the next soil layer for the measurements. This process continued until the seventh soil layer was completed. The measurement for each layer was described below.

For model calibrations, the data of soil shear torque was measured at each of the seven soil layers using a vane shear meter (Geovane, New Zealand). The meter consisted of a dial, a shaft, and four vanes (Figure 6.1d). A single vane has dimensions of 10 × 29 × 1.5 mm (width × height × thickness). The meter was pushed into the soil till the top edge was in level with the soil surface. Then, the meter was rotated by hand slowly till the soil failed. The rotation velocity was not specified in the ASTM standard (ASTM standard, D8121, 2019). An approximation of 0.5 rpm was used based on a literature study (Stefanow and Dudziński, 2021). The reading on the meter dial was recorded and used to calculate the soil shear torque (N·m), referring to the manual of the meter. As the soil background information, soil moisture content and soil bulk density were also measured at each soil layer. A cylindrical sampler with a diameter of 51.6 mm and a height of 50 mm was used to take soil cores. The soil cores were weighed before being dried in an oven at 105°C for 24 hours and re-weighed after drying to obtain the gravimetric soil moisture content (d.b.) and dry soil bulk density (ASABE Standards, 2015). The bulk densities of the soil were used for the model development, as described later.

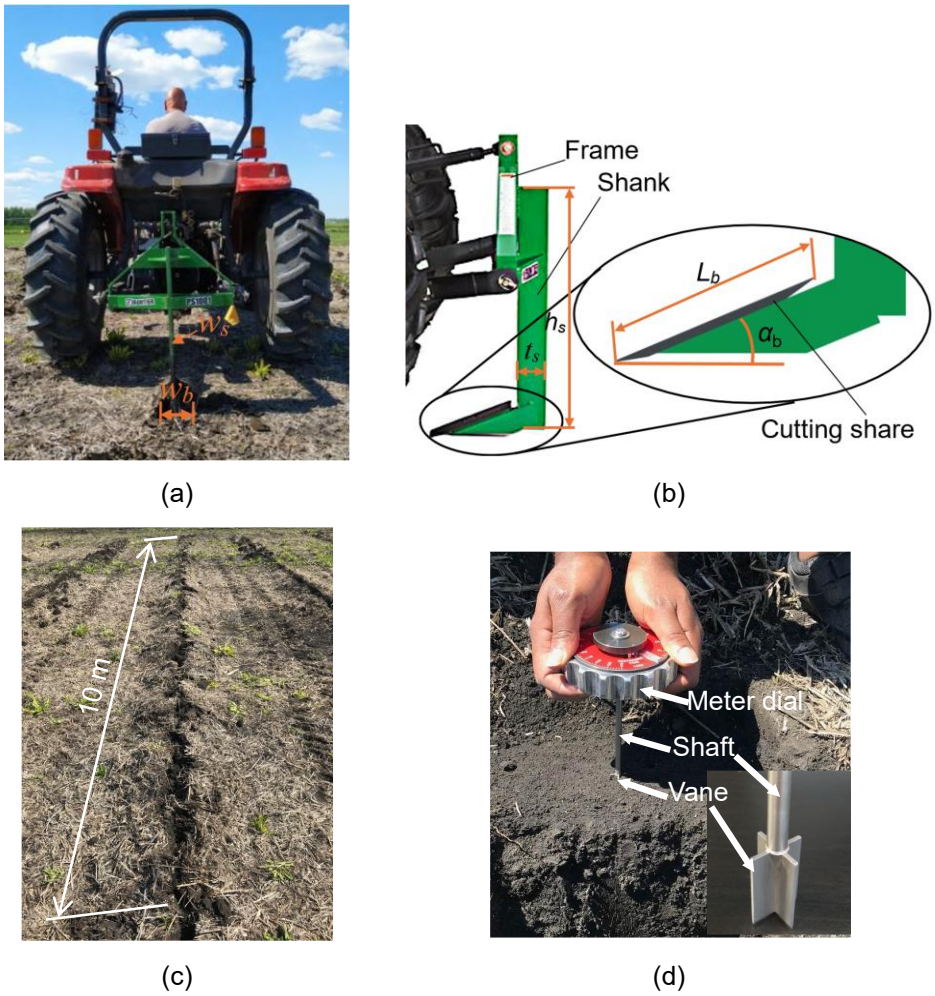

Figure 6.1. Field test: (a) subsoiler and tractor; (b) geometric shape of subsoiler (L_b = 306 mm, share blade length; α_b = 22.5°, share rake angle; w_b = 68 mm, share blade width; t_s = 101 mm, shank thickness; h_s = 520 mm, shank vertical height; w_s = 20 mm, shank width); (c) soil surface condition after subsoiling (subsoiler working speed: 3 km h^{-1}); and (d) vane shear meter for soil shear torque measurement.

For model validations, soil disturbance characteristics were measured after subsoiling. Immediately following the passage of the subsoiler, a panel was inserted into the disturbed soil above the original soil surface (Figure 6.2a). The panel was positioned to be perpendicular to the path of the subsoiler. Then, the panel was sprayed with black paint along the surface of the soil profile. The lower boundary of the paint outlined the elevated soil surface profile. It could be seen

clearly that the elevated soil surface profile formed a mound with rough top surface (Figure 6.2b). Such an irregular shape was the result of the non-homogeneous nature of soil.

To quantify the irregular shape of the disturbed soil, three shape characteristics, including the surface flatness, soil disturbance width and area, were considered to be suitable. The elevated soil surface profile was vertically divided into small trapeziums with equal width of 50 mm. The height of each trapezium was measured as h (Figure 6.2b). The standard deviation of h values was defined as soil surface flatness (F). The soil disturbance width (width of elevated soil surface profile) (W) was measured, as shown in Figure 6.2b. The elevated soil area (A) was the sum of the areas of all trapeziums calculated using the trapezium rule as following:

$$A = d_0 \times \left(\frac{h_0+h_n}{2} + \sum_{i=1}^{n-1} h_i\right) \quad (6.1)$$

where, A = elevated soil area (mm^2), d_0 = the width of the trapezium (mm) which was 50 mm in this case, h = the height of the trapezium (mm), i = the i-th division points; subscript 0 and n stand for the first and last division points.

(a)

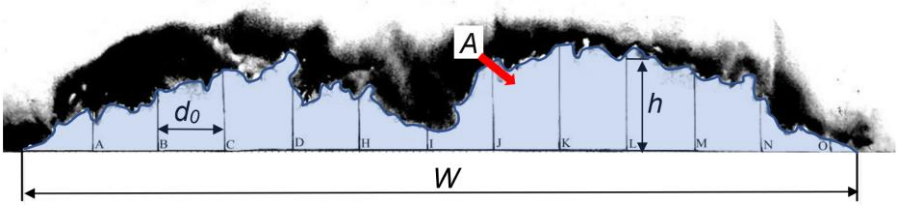

(b)

Figure 6.2. Measurements of soil surface disturbance after subsoiling: (a) a panel inserted into the loose soil and painted outline of soil profile and (b) diagram of data processing (A = elevated soil area; W = soil disturbance width; d_0 = width of trapezium; h = height of trapezium).

6.3.1.4 Data Analysis

The statistical software, R-studio (version 2022.07.1, build 554, RStudio Inc..), was used to perform analysis of variance (ANOVA). Effects of the experimental factor (subsoiler working speed) on soil disturbance characteristics (W, F, and A), as well as the variation of soil properties among soil layers were analysed. The means of these dependent variables were compared at various subsoiler working speeds and soil layers with Duncan's multiple range tests at the significance level of 0.05.

6.3.2 DEM Simulation

A soil-subsoiler interaction model was developed and calibrated to simulate the soil dynamic attributes resulting from the subsoiling. The model was constructed using commercial DEM

software, Particle Flow Code in Three Dimensions (PFC^{3D}) (Itasca Consulting Group Inc., Minneapolis, USA). The processes of model development are described below.

6.3.2.1 Model Soil Particles and Model Parameter Calibration

Soil was modelled as an assembly of spherical particles. The bulk density of the model soil was set to be the same as the soil in the field experiment. This was achieved by adjusting the particle density of spheres in the model according to the desired soil bulk density as follows (Campbell, 1985).

$$\rho_p = \frac{\rho_b \times V_d}{N_p \times V_p} \quad (6.2)$$

where, ρ_b = soil bulk density (kg m^{-3}), ρ_p = soil particle density (kg m^{-3}), V_d = volume of soil domain (m^3), V_p = volume of single particle (m^3), N_p = number of soil particle.

The cohesive behaviour of soil particles was mimicked by a PFC built-in contact model, linear parallel bond model (PBM) (Pontyond and Cundall, 2004). In PFC^{3D}, the particle and bond properties can be assigned by two different methods: (1) setting stiffness, including normal and shear stiffness and (2) setting deformability via effective modulus and normal-to-shear stiffness ratio. The relationships between deformability and stiffness are shown below.

$$\begin{cases} K_n = 2L_C E_p \\ K_s = \frac{K_n}{k_p} \end{cases} \quad (6.3)$$

$$\begin{cases} \overline{K_n} = \frac{E_{pb}}{L_C} \\ \overline{K_s} = \frac{\overline{K_n}}{k_{pb}} \end{cases} \quad (6.4)$$

where, K_n = particle normal stiffness (N m^{-1}), K_s = particle shear stiffness (N m^{-1}), $\overline{K_n}$ = bond normal stiffness (Pa m^{-1}), $\overline{K_s}$ = bond shear stiffness (Pa m^{-1}), E_p = modulus of elasticity of particle

(Pa), E_{pb} = modulus of elasticity of bond (Pa), k_p = normal-to-shear stiffness ratio of particle (dimensionless), k_{pb} = normal-to-shear stiffness ratio of bond (dimensionless), L_C = centre-to-centre distance of particles (m).

In this study, method (2) was used, as the effective modulus and normal-to-shear stiffness ratio are independent of particle size. Thus, the dynamic behaviours of soil particles were determined by eight parameters: modulus of elasticity of particle (E_p, Pa), normal-to-shear stiffness ratio of particle (k_p, dimensionless), particle friction coefficient (μ, dimensionless), modulus of elasticity of bond (E_{pb}, Pa), normal-to-shear stiffness ratio of bond (k_{pb}, dimensionless), bond tensile strength (σ, Pa), bond cohesion strength (τ, Pa), and bond radius multiplier (λ, dimensionless).

The model was calibrated using the field data of soil shear torque. A soil shearing model was built to simulate the field soil shear tests described above. The soil shearing model had 22,697 soil particles with a uniform diameter of 2.5 mm, filled into a cylindrical container that was 90 mm in diameter and 100 mm in height (Figure 6.3a). The model vane shear meter was simplified as four vanes with the same dimensions as the real vanes. Stiffness and friction of the container and vanes were 1×10^8 N m^{-1} and 0.5 respectively (Zeng et al., 2017). To simulate the field soil shearing tests, four vanes were inserted into the soil particles at a constant speed of 0.25 m s^{-1} (Murray and Chen, 2019) until the tops of the vanes were in level with the soil surface (Figure 6.3b). Then the vanes were rotated in soil at a uniform rotational velocity of 0.5 rpm (Stefanow and Dudziński, 2021) until the soil failed in shear. The soil shear torque was the maximum total torque experienced by the four vanes, recorded using a built-in history function in PFC^{3D}.

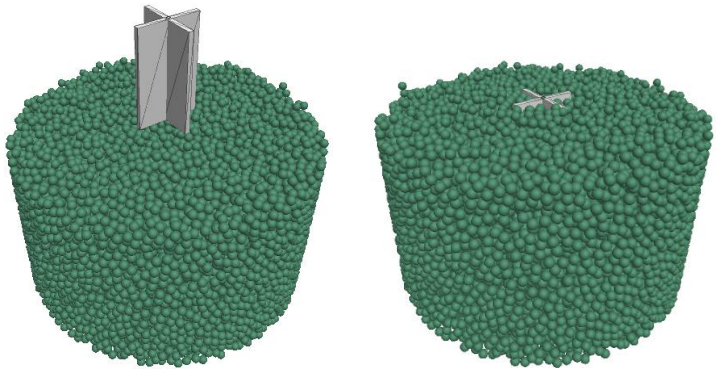

(a) (b)

Figure 6.3. Virtual soil shear test: (a) particles and vane shear meter before testing and (b) vanes inserted into particles.

Sensitivity analyses were performed to identify the influence of eight aforementioned model parameters on soil shear torque. The results illustrated that the soil bond tensile strength (σ) and bond cohesion strength (τ) were the most influential parameters on model outputs. The σ and τ were set to be same value, and the σ therefore was calibrated. The other model parameters, including DEM damping ratios and coefficient, were adopted from Murray and Chen (2019) who modelled a similar soil type. They are summarized in Table 6.1. In the calibration, a series of assumed σ values were used to obtain the proper simulated torque (T_S) that matched the torque measured (T_M) in the field. The σ was calibrated against the field torque measured at each of seven different soil layers: *L1*, *L2*, *L3*, *L4*, *L5*, *L6*, and *L7*.

Table 6.1. Soil model parameters (Murray and Chen, 2019).

Property	Unit	Value
Modulus of elasticity of particle, E_p	Pa	5.692×10^7
Normal-to-shear stiffness ratio of particle, k_p	Dimensionless	1.0
Particle friction coefficient, μ	Dimensionless	0.5
Normal critical damping ratio, β_n	Dimensionless	1.0
Shear critical damping ratio, β_s	Dimensionless	1.0
Local damping coefficient, θ	Dimensionless	0.5
Bond radius multiplier, λ	Dimensionless	0.5
Modulus of elasticity of bond, E_{pb}	Pa	2.5×10^7
Normal-to-shear stiffness ratio of bond, k_{pb}	Dimensionless	1.0
Bond tensile strength, σ	Pa	To be calibrated
Bond cohesion strength, τ	Pa	Equal to σ

6.3.2.2 Soil-Subsoiler Interaction Models

The soil-subsoiler interaction model included a model subsoiler and a soil domain (Figure 6.4). Crop residue was not included in the model, assuming a negligible effect of residue. The assumption was justified by the fact that soil disturbance occurred mainly in the deep soil and most residue remained on the surface after subsoiling. The model subsoiler was created in a 3D computer-aided design software (SolidWorks) and imported into PFC^{3D}. The stiffness and friction of subsoiler were 1×10^8 N m^{-1} and 0.5 respectively (Zeng et al., 2017). The subsoiler travelled at the same depth and speed as in the field experiment, so that the simulation results could be compared among the models and between the model and field results.

The soil domain had 296,219 soil particles in a soil bin of 600 mm in width, 1000 mm in length, and 600 mm in height. The soil depth in the soil bin was 450 mm. The diameter of soil

particles was 10 mm that was larger than the particles in the calibration model to reduce the computation time. As aforementioned, soil parameters were defined by the deformability that is independent of soil particle size. The soil was divided into layers. The number of soil layers could be varied in a model for the same soil condition. A model with more soil layers may be more accurate, but such a model would be more complex. Therefore, there must be some trade-off between the model complexity and its accuracy. To find out this, three models with different numbers of layers were developed for modelling the field soil. They were a 7-layer model, a 3-layer model, and a 1-layer model, namely heterogeneous soil model (HeS Model), semi-heterogeneous soil model (SHeS Model), and homogeneous soil model (HoS Model). The soil heterogeneity of the model was reflected by the variation of the value of soil parameter, σ among the soil layers. The layers of the HeS Model: *L1*, *L2*, *L3*, *L4*, *L5*, *L6*, and *L7* (Figure 6.4a) coincided with the layers used for the field measurements. The corresponding soil parameters were σ_1, σ_2, σ_3, σ_4, σ_5, σ_6, and σ_7. The values of σ_i (i stands for the i-th soil layer) were calibrated in the way described above. The layers of the SHeS Model were the depth ranges: 0 – 100, 100 – 250, and 250 – 450 mm (Figure 6.4b). This model can be used to represent a typical compacted field with a top layer, a hardpan, and a subsoil layer (Chen and Tessier, 1997). The HoS Model had a non-layered structure (Figure 6.4c). For the SHeS Model and HoS Model, the average value of the calibrated σ_i within the perspective soil depth was assigned to the corresponding layer, as labelled in Figure 6.4b and 6.4c. The time of each simulation was approximately 18 hours (varying with different working speed) using a Dell Workstation with 192 GB RAM, a 2.10 GHz Intel (R), and Xeon (R) Silver 4110 CPU (2 processors). The default timestep (approximately 3e-5 s) that was automatically calculated was used throughout simulations.

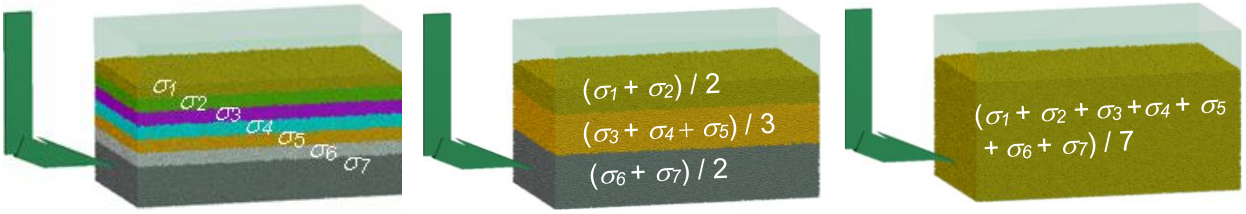

(a) (b) (c)

Figure 6.4. The soil-subsoiler interaction models with varying degrees of soil heterogeneity reflected by different soil bond tensile strength, σ_i (*i* stands for the *i*-th soil layer): (a) HeS Model with seven layers; (b) SHeS Model with three layers; and (c) HoS Model with one layer.

6.3.3 Monitoring of Soil Disturbance Characteristics

In DEM simulations, soil disturbance can be examined from soil cross-sections at any moment of subsoiling operation. In the longitudinal direction (parallel to the subsoiler travel direction) shown in Figure 6.5a, micro-behaviours of soil disturbance, including soil particle mixing and movement, were observed. Macro-behaviours of soil disturbance were examined in the lateral cross-section at different locations (d) relative to the shank of subsoiler. These locations (from d = 0 to d = 400 mm) are illustrated in Figure 6.5a. From the lateral soil cross-section located right in front of the subsoiler shank (i.e., d = 0 mm) shown in Figure 6.5b, characteristics of W, F, and A were quantitatively assessed. These characteristics were defined via the same way as in the field measurements. The coordinates of the disturbed soil profile were extracted in MATLAB. Simulated W, F, and A were obtained using the coordinates. These characteristics were compared with the field measurements. The agreement was assessed by relative error below:

$$RE = \frac{|M-S|}{M} \times 100\% \quad (6.5)$$

where, RE = relative error between measured and simulated data, M = measured data, and S = simulated data.

Using the cross-section as shown in Figure 6.5b, the irregular shape of disturbed soil below the original soil surface was further quantified by several distinct areas. The total disturbed soil area (A_T) was obtained, including two disturbed scenarios, elevated soil area (A) and disturbed soil area below original soil surface (A_D). The boundary between total disturbed soil area (A_T) and undisturbed soil area (A_U) was determined by those particles with velocity of 0.01m s^{-1}. This velocity threshold was chosen because the particle velocities in the elevated soil area were all larger than this value. The A_T at various positions (d) from 0 to 400 mm illustrated the variation of soil disturbance in the longitudinal direction. In addition, using A, A_D, and A_U at d = 0 mm, three other variables: soil bulkiness (q), soil disturbance coefficient (y), and soil swelling ratio (w) were defined (Sun et al., 2018; Huang et al., 2017; Huang et al., 2018). These performance parameters directly reflect the efficiency of compacted soil loosening and subsurface structure improvement. The q quantified the proportion of disturbed soil that has moved upward above the original soil surface after subsoiling, indicating the soil loosening and deformation behaviours. The y monitored the soil below original surface that has actually been disturbed. A higher y indicates a better soil loosening. The w quantitatively analysed loosened soil rising to the surface and soil surface roughness. The q, y, and w were calculated by the following formulas:

$$q = \frac{A}{A_D + A_U} \times 100\% \quad (6.6)$$

$$y = \frac{A_D}{A_D + A_U} \times 100\% \quad (6.7)$$

$$w = \frac{A}{A_D} \times 100\% \quad (6.8)$$

where, q = soil bulkiness (%), y = soil disturbance coefficient (%), w = soil swelling ratio (%), A = elevated soil area (mm^2), A_D = disturbed soil area below the original soil surface (mm^2), and A_U = undisturbed soil area (mm^2), as illustrated in Figure 6.5b.

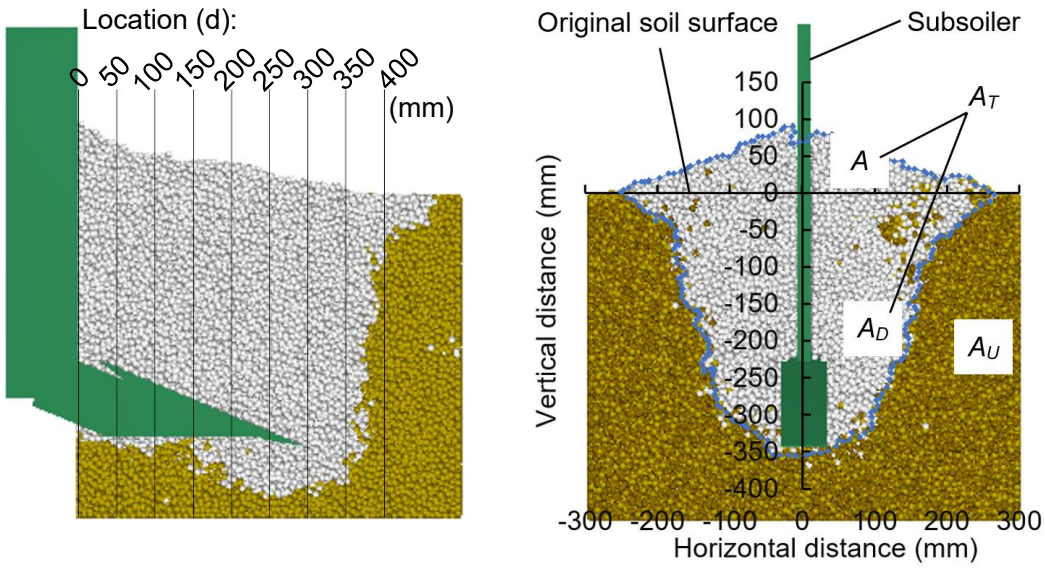

Figure 6.5. Examples of screenshots from simulations (subsoiler working speed = 2 km h^{-1}, the HeS Model): (a) longitudinal soil cross-section showing the locations (d) of different lateral soil cross-section; and (b) lateral soil cross-section (d = 0 mm), showing soil disturbance A = elevated soil area, A_D = disturbed soil area below original soil surface, A_T = total disturbed soil area, and A_U = undisturbed soil area.

6.4. Results and Discussion

6.4.1 Measured Soil Properties Before Subsoiling

Soil moisture content and soil bulk density for seven soil layers (*L1*, *L2*, *L3*, *L4*, *L5*, *L6*, and *L7*) are shown in Table 6.2. The soil moisture content was reported with three significant digits while the soil bulk density was with five significant digits, resulting from the various resolution of measurement instruments and methods. There was little variation in soil moisture content between layers in the field. Only the soil moisture content (39.0%) in *L5* was higher, while other layers had statistically similar soil moisture content. For dry soil bulk density, statistically significant differences were not detected among different soil layers. The average soil bulk density over the entire soil profile was 1041.5 kg m^{-3}. This average value was used to set the soil bulk density of

model particles in the simulations. However, the measured soil torques were significantly different among the soil layers (Table 6.3). This reflected the heterogeneousness of the soil depth profile.

Table 6.2*. The measured soil conditions for each soil layer.

Soil layer	Soil depth (mm)	Soil moisture content (%)	Soil bulk density (kg m^{-3})
L1	0 – 50	34.0 ± 1.0 ^{b}	976.7 ± 77.3 ^{a}
L2	50 – 100	34.7 ± 1.2 ^{b}	1037.5 ± 49.4 ^{a}
L3	100 – 150	35.3 ± 0.5 ^{b}	1037.0 ± 60.8 ^{a}
L4	150 – 200	36.9 ± 2.3 ^{ab}	1063.7 ± 58.8 ^{a}
L5	200 – 250	39.0 ± 3.1 ^{a}	1025.8 ± 61.3 ^{a}
L6	250 – 300	37.2 ± 1.2 ^{ab}	1059.5 ± 34.0 ^{a}
L7	300 – 450	34.6 ± 2.2 ^{b}	1090.4 ± 70.8 ^{a}

*Mean within a column followed by the same letters are not significantly different according to Duncan's multiple range test at the significance level of 0.05.

6.4.2 Calibrated Model Parameters

Soil shear torques measured and simulated are shown in Table 6.3. For the soil layer, *L1*, the soil shearing model was run with assumed values of σ_1 from 1.0×10^5 to 2.0×10^5 Pa with the increment of 0.05×10^5 Pa (a total of 21 assumed values). It was found that when the $\sigma_1 = 1.55 \times 10^5$, the simulated soil shear torque ($T_S = 0.76$ N·m) best matched the mean of the measured torque ($T_M = 0.77$ N·m). The *RE* was 1.5% in this case. Similarly, the matching was performed for all the other layers from *L2* to *L7* to obtain the calibrated values of σ_2 to σ_7. The resultant *RE* ranged from 0.0% to 6.6%, with an average of 3.7%. This indicated that the calibrated σ values were reasonably reliable, and they were used throughout the following simulations.

Table 6.3*. The calibration results for each soil layer.

Soil layer	Parameters	Calibrated value (Pa)	T_S (N·m)	T_M (N·m)	*RE* (%)
L1	σ_1	1.55×10^5	0.76	0.77 ± 0.32 ^{cd}	1.5
L2	σ_2	1.95×10^5	1.10	1.10 ± 0.13 ^{ab}	0.0
L3	σ_3	2.00×10^5	1.15	1.22 ± 0.16 ^{a}	6.1
L4	σ_4	1.75×10^5	0.92	0.96 ± 0.05 ^{bc}	4.3
L5	σ_5	1.80×10^5	0.82	0.86 ± 0.12 ^{cd}	5.1
L6	σ_6	1.55×10^5	0.76	0.71 ± 0.11 ^{d}	6.6
L7	σ_7	1.55×10^5	0.76	0.74 ± 0.15 ^{cd}	2.1

*Mean within a column followed by the same letters are not significantly different according to Duncan's multiple range test at the significance level of 0.05. T_S = simulated soil shear torque; T_M = measured soil shear torque; and *RE* = relative error between measured and simulated value.

6.4.3 Simulated Dynamic Behaviour of Soil

6.4.3.1 Soil Micro-Behaviours

Using the calibrated soil parameters, the soil-subsoiler models were run to examine the soil micro-behaviour. Interesting phenomena were observed in the longitudinal soil cross-section (parallel to the travel direction). As the subsoiler travelled in soil, it impacted soil particles in the front, causing the movement of soil particles (Figure 6.6). The soil particles in motion formed three distinct zones, based on the magnitude of particle velocity. A "pushing zone" existed at the interface between the subsoiler shank and soil, and also between the subsoiler cutting share and soil. In this zone, soil particles in contact with the subsoiler were pushed forward, and the velocities of these particles are the highest among all particles. In the outmost front, there is a "rising zone", where the moving soil particles seemed to make a "sharp turn" from the forward direction to an upward direction. This may be due to the slope effect of the subsoiler cutting share, as the zone

appeared to be located along the normal direction of the cutting share. At the lower soil profile, the “rising zone” spanned over the entire length of the cutting share, whereas became narrower in the upper soil profile. Interestingly, there was a “passive zone” between the “pushing zone” and “rising zone”. In the “passive zone”, soil particles had lower velocities than the other two zones, and moved forward and upward. The zone was of a triangle shape, with one boundary parallel to the subsoiler shank, one boundary along the normal direction of the cutting share of the subsoiler, and one boundary being the top surface of soil. It is believed that the occurrence of the “passive zone” is associated with the actions of both the shank and cutting share. The angle formed by the shank and cutting share might have contributed to the triangular shape of the “passive zone”. The micro-behaviour of soil discussed here would not possibly be observed in an experiment, which demonstrates the advantages of the DEM simulation. And the phenomena were merely found in HeS Model.

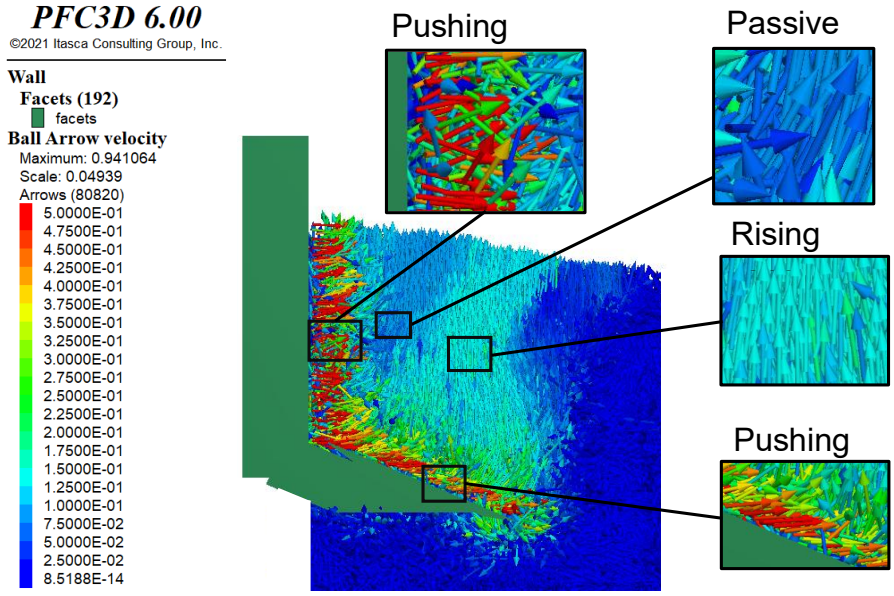

Figure 6.6. Velocity (unit: m s^{-1}) flow of soil particles during passage of subsoiler in HeS Model showing micro-behaviour of soil particles (subsoiler working speed = 2 km h^{-1}).

Mixing of soil particles between layers was also observed through simulations. For HeS Model (Figure 6.7a), the mixing of soil particles occurred in all seven layers. But it seemed that the mixing action took place only between the adjacent layers. Also, the mixing occurred only behind the subsoiler, possibly due to the soil back filling the furrow created by the subsoiler. There was little mixing between the layers in the front of the subsoiler, but the layers were curved due to the soil lifting function of the subsoiler. Similar soil mixing occurred for SHeS Model with three layers (Figure 6.7b). This model had thicker layers, which showed more clearly that the mixing action was basically limited at the layer boundaries, not the central zone of the layer. Particles mixing in layered soil structures was not about the changes in particle location only, but also the interactions between particles with different properties (e.g., bond tensile strength, σ in this case). As for HoS Model, the phenomena of particle mixing between different depth certainly existed, but it was not visualized due to the non-layered structure (Figure 6.7c). However, it would be expected that the mixing in this model had the least effect on the micro-behaviours due to the relatively more homogeneous soil particles.

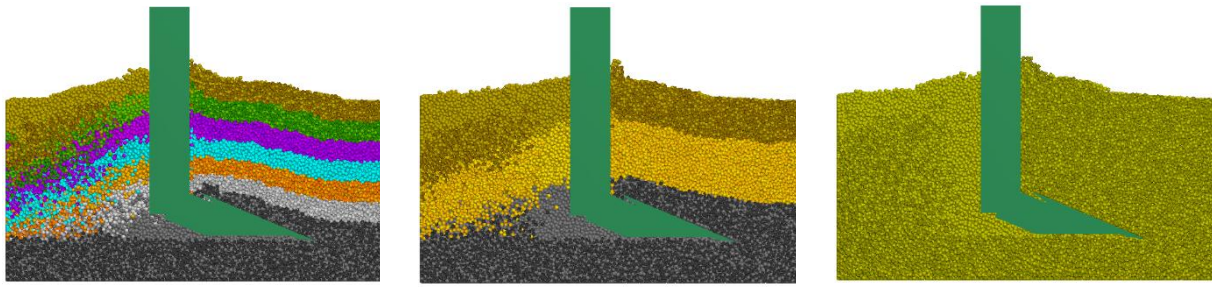

(a) (b) (c)

Figure 6.7. Soil particle mixing between layers (subsoiler working speed = 2 km h^{-1}): (a) HeS Model; (b) SHeS Model; and (c) HoS Model.

6.4.3.2 Soil Macro-Behaviours

Lateral cross-sections were examined to understand how much and how far the subsoiler was able to impact the soil in its front. This was done on the lateral cross-sections at different locations (d) relative to the subsoiler shank, as illustrated in Figure 6.5a. At each location, the total disturbed soil area (A_T), consisted of the elevated soil area (A) and the disturbed soil area below the original soil surface (A_D), were examined. Near the subsoiler shank, for example, d = 0, there was the largest A, and it was reducing further away from the subsoiler shank. At d = 400 mm, soil surface became flat, resulting in a zero A. This observation was consistent with the raised soil surface shown in Figure 6.8. The A_D also reduced from d = 0 to d = 400 mm, as visually seen in Figure 6.8a. The A_T was further quantified in Figure 6.8b. At d = 0 mm, the A_T was 132,500 mm^2. As the location moved away from the subsoiler shank, the general trend was gradually decreasing in A_T up to d = 350 mm. Then, there was a sudden drop in A_T at d = 400 mm. However, there were still some soil disturbances at d = 400 mm. The results indicated that the disturbance from the subsoiler to the soil was able to propagate for as far as 400 mm in front of the subsoiler. Also, the results supported the method used to assess soil disturbance characteristics at the subsoiler shank (d = 0 mm) to obtain maximum values.

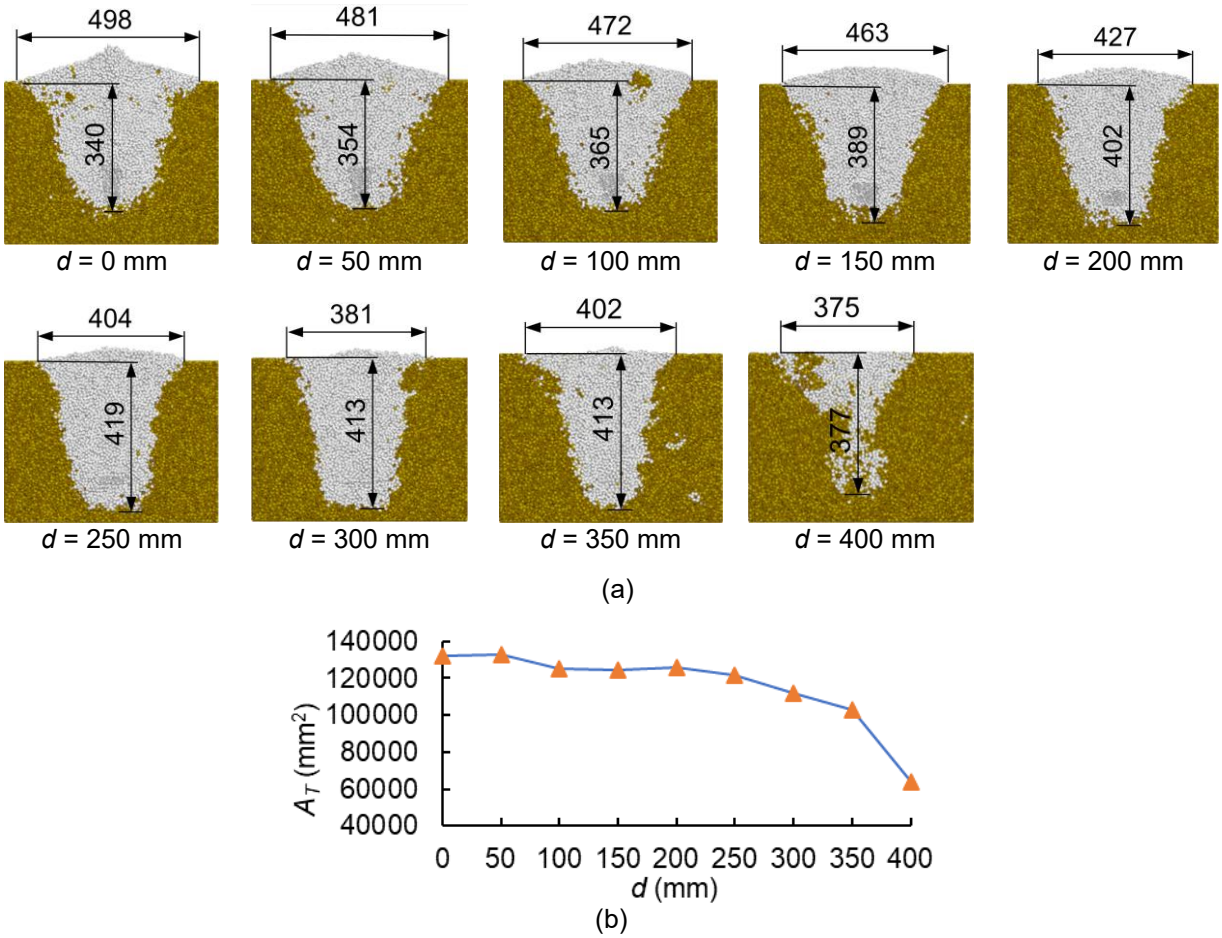

Figure 6.8. Soil disturbance in front of the subsoiler (subsoiler working speed = 2 km h^{-1}) at different locations (d) relative to the shank of the subsoiler: (a) lateral soil cross-section with dimensions (the dimensions are in mm) showing soil particles disturbed by the subsoiler; and (b) the variation of total disturbed soil area (A_T) at different locations (d).

6.4.4 Model Accuracy

The HeS Model, SHeS Model, and HoS Model were run to predict soil disturbance characteristics: A, F, and W. Simulated values were then compared with measured ones to examine how the model heterogeneity affected the accuracies of these model outputs. The comparisons were made at each of the working speeds: 2, 3, 4, 5, and 6 km h^{-1}. These regression lines (Figures 6.9, 6.10, and 6.11) were plotted along the simulated data points to provide a visual and quantitative

comparison between the experimental measurements and the simulations. The purpose was to assess the agreement and trend consistency between simulation and filed results. In general, the effects of working speed on the measurement variables had some irregularities. This was expected due to the highly variable conditions in the field. The simulation results showed better trends for the effects of working speed.

6.4.4.1 Comparisons Between HeS Model Results with the Measurements

Both simulations in HeS Model and field measurements are shown in Figure 6.9. Over the range of the working speeds, all measured soil disturbance characteristics, including soil surface flatness (*F*), elevated soil area (*A*), and soil disturbance width (*W*), significantly increased as the working speed increased from 2 to 6 km h^{-1}. Over this range of working speed, the measured *F*, *A*, and *W* increased by 14.9%, 29.9%, and 6.5% respectively. The differences in *W* among working speeds were relatively small. The increased soil disturbance agreed well with the existing studies in which tillage tool with a higher working speed was more aggressive in disturbing soil (Zeng and Chen, 2018; Zeng et al., 2020). The simulated *F* was 19.9 mm at the 2 km h^{-1}, and it increased to 31.9 mm at the 6 km h^{-1} (Figure 6.9a). This increasing trend was much more pronounced than the measured one. In both simulations and measurements, *A* did not appear to have a good linear tendency, because of one point at 3 km h^{-1} that was off the linear trend (Figure 6.9b). At this point, the simulated *A* was lower, while the measured *A* was higher. The reasons for these opposite values were unknown. For results of *W*, both the simulated and measured *W* slightly increased over the range of subsoiler working speed (Figure 6.9c). Among the three soil disturbance characteristics, the simulated results of *F* (Figure 6.9a) had a more pronounced increasing trend, but less consistent, than the simulated results of *A* (Figure 6.9b) and *W* (Figure 6.9c). This phenomenon occurred,

because the *A* and *W* were primarily governed by the geometry and kinematics of soil-subsoiler interactions, which were less sensitive to the changes in working speed.

In terms of relative error (*RE*), the simulated values of *A* were comparable with the measured values, except for the speed of 3 km h^{-1} where the relative error (*RE*) was much higher (46.7%) (Figure 6.9d). The discrepancy was possibly attributable to measurement errors due to the high variations of the field condition. The *RE* values of *A* for the other speeds were all lower than 5%. When compared to the measured values of *W*, the simulated values agreed well. The highest *RE* values was 15.0%. The simulated *F* had much large *RE* values, especially at 5 and 6 km h^{-1}. Results showed that the accuracies of the model depended on which soil disturbance characteristics was predicted. The accuracies of the model also varied with the subsoiler working speed. To assess the overall performance of the model for predicting each soil disturbance characteristics, the relative errors were averaged over all speeds to obtain the overall relative errors that were 43.7% for *F*, 11.1% for *A*, and 6.1% for *W*. Typically, a relative error of 20% or lower is acceptable for modeling and simulation (Huang et al., 2018). With this judging criterion, the HeS Model was suitable for predicting *A* and *W*, but not *F*.

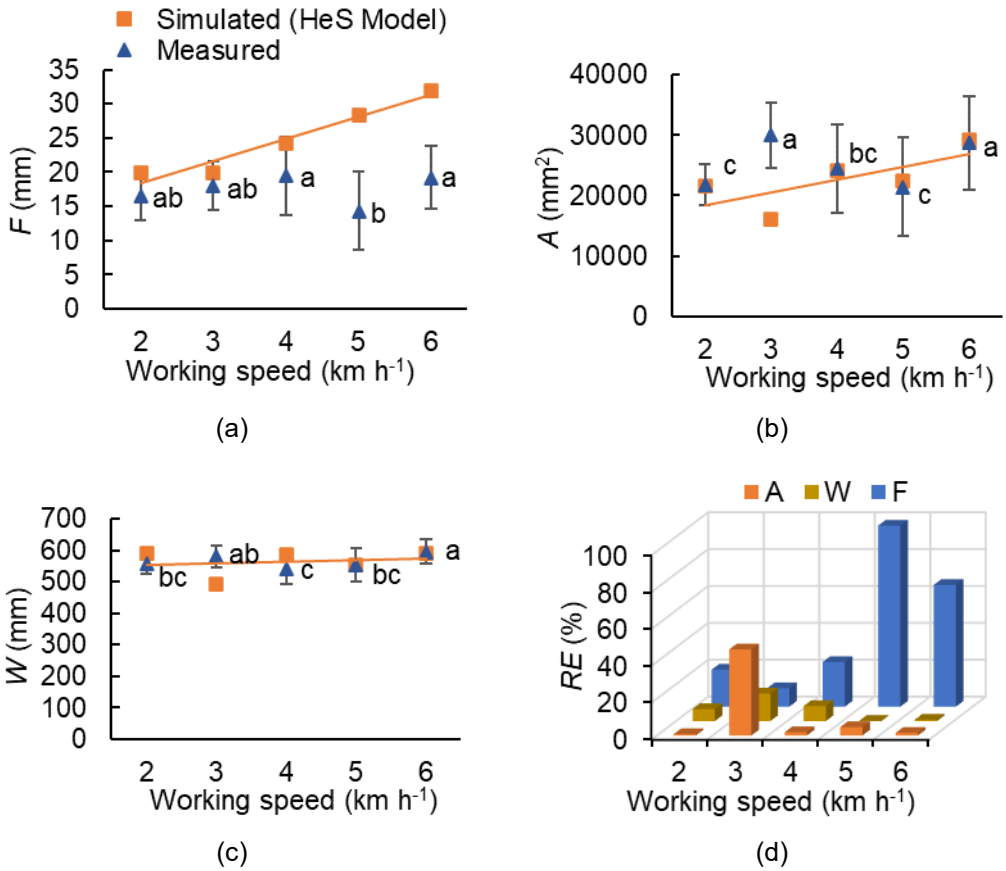

Figure 6.9. Comparisons between simulations results in the HeS Model and measurements for different subsoiler working speeds: (a) soil surface flatness (*F*); (b) elevated soil area (*A*); (c) soil disturbance width (*W*); and (d) the relative errors (*RE*); means followed by different letters are significantly different according to Duncan's multiple range test at the significance level of 0.05; error bars are standard deviations.

6.4.4.2 Comparisons Between SHeS Model with the Measurements

Simulation results from SHeS Model were compared with measurements in Figure 6.10. In terms of trends, the simulated *F* fitted a plateauing trend (Figure 6.10a). However, the simulated results of *F* had linear increasing trends for HeS Model (Figure 6.9a) and HoS Model (Figure 6.11a). The reason was as follows. The HoS Model lacked resistance variability, leading to consistently increasing of *F*. The HeS Model with detailed heterogeneity resulted in rougher

surface at higher working speeds due to cumulative disturbance among soil layers. However, SHeS Model presented a buffering middle soil layer that constrained excessive surface disruption.

The simulated *F* increased with the working speed from 2 to 5 km h^{-1}, and then decreased at the 6 km h^{-1} speed. All the measured *F* values were lower than the simulated values. Moreover, the simulated *F* changed more dramatically than simulated *A* (Figure 6.10b) and *W* (Figure 6.10c) as the working speed increased in the SHeS Model, consistent with the trend observed in the HeS Model. From 2 to 6 km h^{-1}, simulated *A* slightly increased with the working speed (Figure 6.10b). The measured *A* values scattered, and they were all greater than the simulated values, except for the speed of 5 km h^{-1}. A slightly increasing trend was observed for the simulated *W* that was smaller than the measured value at each of the five working speeds (Figure 6.10c).

Results showed that SHeS Model overpredicted *F* and underpredicted *A* and *W*. In terms of *RE*, the simulated *W* agreed well with measured values, except for the speed of 4 km h^{-1} (Figure 6.10d). The overall relative errors were 37.8% for *F*, 18.8% for *A*, and 14.2% for *W*. Again, using the 20% judging criterion for acceptable relative errors, SHeS Model was not suitable for predicting F, but produced acceptable results for predicting *A* and *W*. However, the overall predictions by SHeS Model were less accurate than HeS Model.

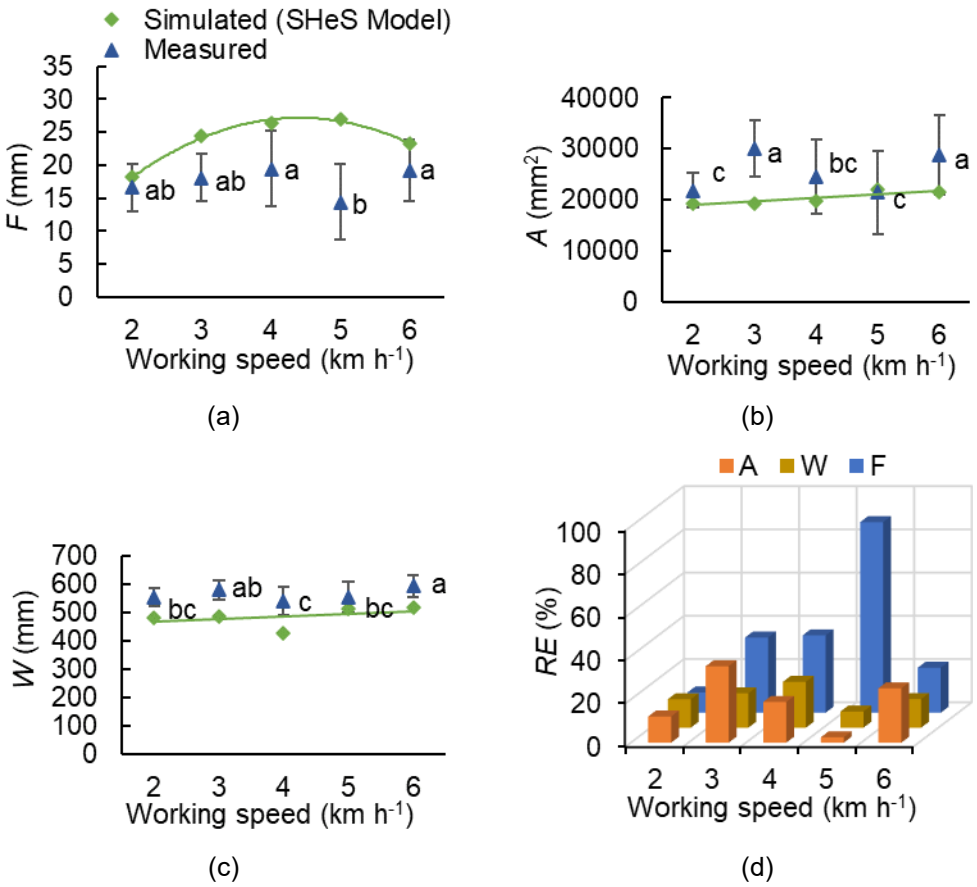

Figure 6.10. Comparisons between simulations results in the SHeS Model and measurements for different subsoiler working speeds: (a) soil surface flatness (*F*); (b) elevated soil area (*A*); (c) soil disturbance width (*W*); and (d) the relative errors (*RE*); means followed by different letters are significantly different according to Duncan's multiple range test at the significance level of 0.05; error bars are standard deviations.

6.4.4.3 Comparisons Between HoS Model with the Measurements

Figure 6.11 shows the comparisons of simulation from HoS Model and measurement. Based on Figure 6.11a, the simulated *F* appeared to be a predictable linear tendency, having an increasing trend with the increasing of working speed. The increasing trend of *F* was larger than the increasing trend of *A* and *W*, with the same reason as in HeS and SHeS Model. Also, the simulated values were comparable with the measurements at the lower range of working speed. The simulated *A* also had a linearly increasing trend. The model underpredicted *A* in four out of five working speeds

(Figure 6.11b). The increasing tendency with the speed was not the case for *W* which was kept constant over all the working speeds (Figure 6.11c). The simulated *W* was comparable to their corresponding the measurements at all cases.

In terms of *RE* (Figure 6.11d), HoS Model improved the accuracy for predicting *F* compared with HeS and SHeS Models. However, up to 51.2% *RE* was seen at the 5 km h^{-1} speed, which brought its overall relative efficiency to 20.6%. HoS Model failed to predict *A* accurately, based on its overall relative error (25.7%). The *W* ranged from 0.7% to 11.6%, giving an overall relative error of 5.5%. This low overall relative error demonstrated that the accuracy HoS Model in predicting *W* was as good as HeS model. However, HoS Model is not suitable for predicting *F* and *A*, based on the judging criterion of 20%. Based on the above discussions, the variation of the degree of soil heterogeneity had different effects on the accuracy of the model.

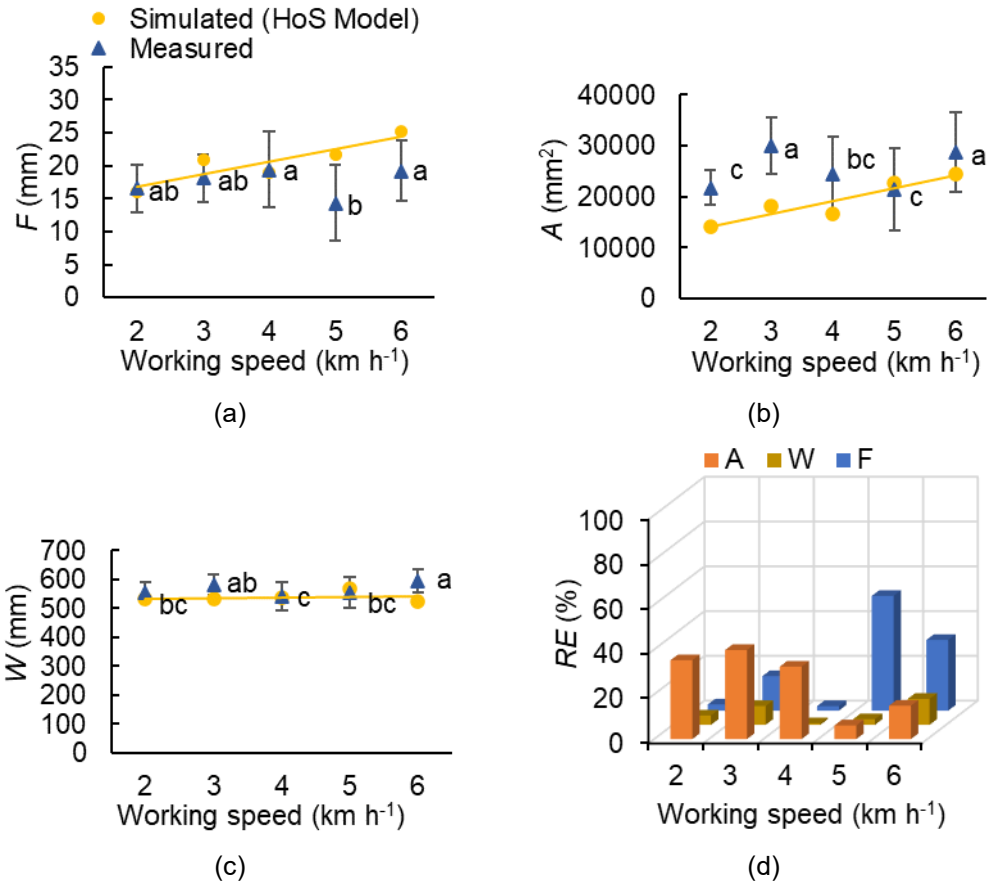

Figure 6.11. Comparisons between simulations results in the HoS Model and measurements for different subsoiler working speeds: (a) soil surface flatness (*F*); (b) elevated soil area (*A*); (c) soil disturbance width (*W*); and (d) the relative errors (*RE*); means followed by different letters are significantly different according to Duncan's multiple range test at the significance level of 0.05; error bars are standard deviations.

6.4.5 Effects of Soil Heterogeneity on Other Soil Disturbance Characteristics

The boundary of disturbed soil area in the lateral soil cross-section was visually compared between three models at various working speeds (Figure 6.12). The cross-sections were located right at the subsoiler shank, i.e., at d = 0 mm shown in Figure 6.5a. Examining the boundaries allowed to compare the shapes of the soil disturbance area among the models and working speeds. Results showed that in all cases, the elevated soil surface profile formed a mound (elevated soil)

with a furrow in the middle, which was consistent with the observations in the field shown in Figure 6.2. It seemed that the subsoiler travelling at 5 or 6 km h^{-1} resulted in a higher soil mound.

Below the original soil surface, the soil disturbance boundary formed a bell-shaped area. As it went down from the soil surface, the soil disturbance width was becoming narrower, up to 120 mm depth. After that, the width of soil disturbance was kept fairly constant, as shown by the fairly straight vertical boundaries. Below the 240 mm depth, the soil disturbance area had the shape of a round cap. In the simulations, the subsoiler was operated at a depth of 350 mm. The result showed that the resultant soil disturbance boundaries were beyond this depth, meaning that the influencing zone of the subsoiler extended deeper than the actual working depth.

When the boundaries were compared among the three models, little differences could be visually seen. Simulated disturbed soil area below the original soil surface appeared to be smaller for SHeS Model at the speed of 2 km h^{-1} (Figure 6.12a) and for HoS Model at 4 km h^{-1} (Figure 6.12c). However, these were not the cases at the other working speeds (Figure 6.12b, 6.12d, and 6.12e). There were no differences in the elevated soil surface profile between the three models, except for the speed of 6 km h^{-1}, where the HeS Model produced the greatest soil disturbance width (Figure 6.12e).

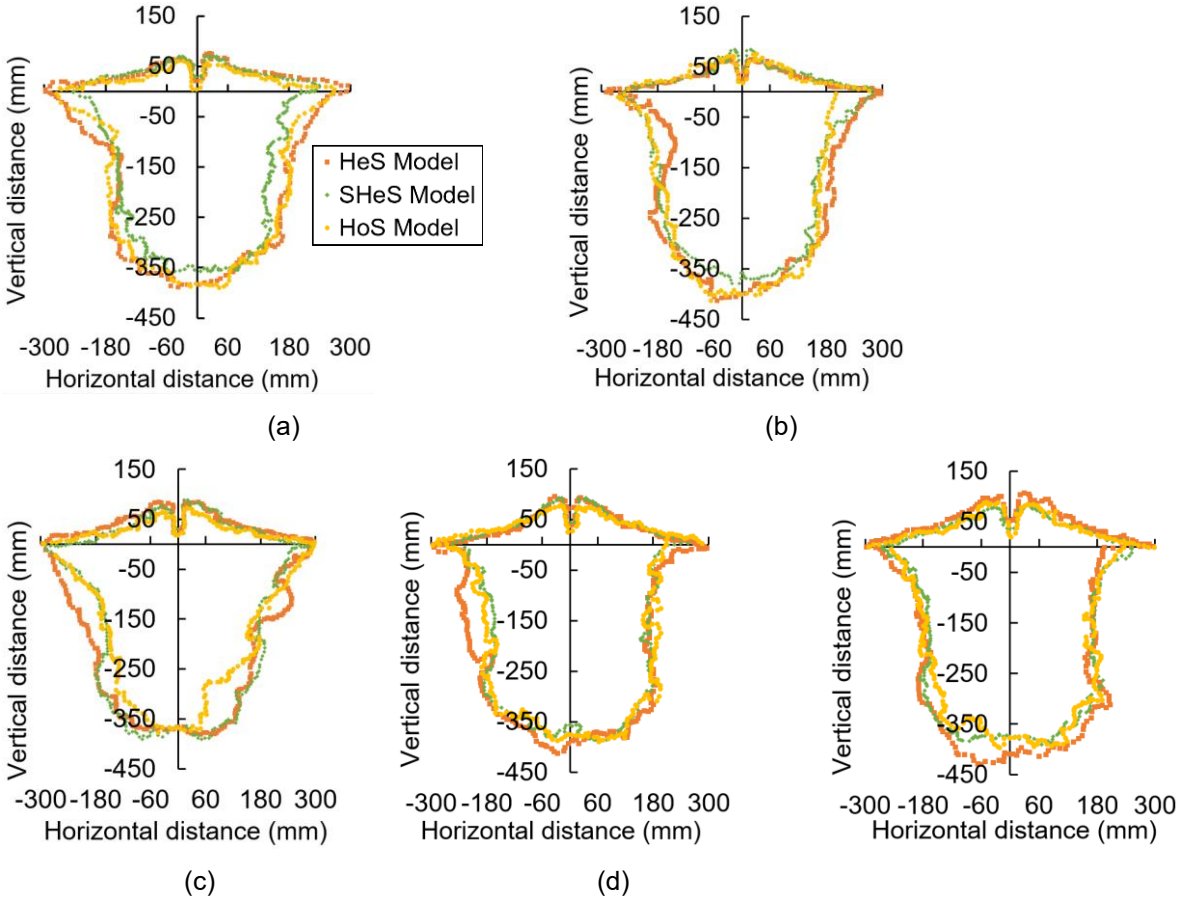

Figure 6.12. Soil disturbed profiles in soil models with different degree of soil heterogeneity at the working speeds: (a) 2 km h^{-1}; (b) 3 km h^{-1}; (c) 4 km h^{-1}; (d) 5 km h^{-1}; and (e) 6 km h^{-1}.

Soil bulkiness (q), soil disturbance coefficient (y), and soil swelling ratio (w) were determined based on the Eqs. (6.6), (6.7), and (6.8) for the three models at various working speeds. Higher working speed resulted in higher q for HeS and HoS models (Figure 6.13a). The predicted y had a gradual decreasing tendency in three models as the increasing of working speed (Figure 6.13b). Therefore, it was concluded that the greater kinetic energy that generated by the travelling of subsoiler lead to more intensive soil breakage, loosening, and displacement. Mixed results in the predicted w were obtained among the three models, which showed an increasing trend in the HeS and HoS Models, whereas a slightly decreasing trend in SHeS Model (Figure 6.13c). The reason might be attributed to the HeS Model and HoS Model which featured continuous gradation,

allowing more efficient upward displacement of loosened soil as the working speed increased. The soil swelling ratio decreased in the SHeS Model because the energy generated by the travelling of subsoiler was more likely to dissipate within lower layers, leading to subsurface deformation rather than upward swelling. Overall, there were small differences among the models in predicting these soil disturbance characteristics, suggesting little effect of the degrees of soil heterogeneity in this regard.

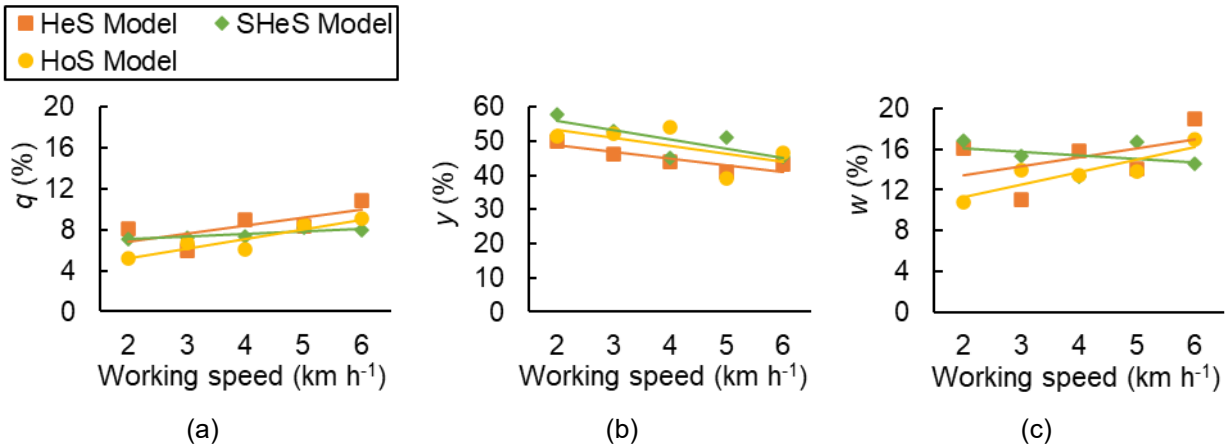

Figure 6.13. The values of soil disturbance characteristics at all speed ranges, in HeS Model, SHeS Model, and HoS Model: (a) soil bulkiness (*q*); (b) soil disturbance coefficient (*y*); and (c) soil swelling ratio (*w*).

6.5. Conclusions

Soil-subsoiler interaction models were developed and calibrated using the DEM. The soil model had different numbers of layers for heterogeneous soil (HeS Model), semi-heterogeneous soil (SHeS Model), and homogeneous soil (HoS Model). The layered soil structure allowed us to model different degrees of soil heterogeneities which represent the variations of field conditions in practice. Calibrations of the models showed that the bond tensile strength of soil was the most critical model parameter, and it varied among different soil layers. The simulations allowed examining micro-behaviours of soil particle dynamics, such as soil particle movement resulting

from the subsoiling. This provided insights into the dynamic interaction of soil-subsoiler dynamics at a particle level, which would not be possible using measurements. Compared with field experimental results, all the three models were suitable for predicting the soil disturbance width over the range of subsoiler working speeds, while none of these three models could predict the soil surface flatness with reasonably good accuracy. HeS Model was the most accurate model for predicting the elevated soil area, the most critical soil disturbance characteristics. However, this model was more complex than SHeS Model and HoS Model, in terms of the number of soil layers. The results have important implications for future development of soil-subsoiler interaction models using DEM. It should be noticed that the results were obtained for the particular subsoiler under the given soil conditions. Cautions should be taken when applying the results to other subsoilers and soil conditions. It is recommended that future DEM models include a hard pan layer and aim to predict soil cutting forces.

6.6. Acknowledgement

This work was financially supported by China Scholarship Council and Natural Sciences and Engineering Research Council of Canada (grant number: RGPIN-2019-05861).

6.7. References

Adnan, N. S., Mohsin, T., Babar, S., Guozheng Y., Shah, F., Saif, A., Muhammad, A. B., Shahbaz, A. T., Abdul, H., Biangkham, S., 2017. Soil Compaction effects on soil health and crop productivity: An overview. Environmental Science and Pollution Research International, 24, 10056–10067. https://doi.org/10.1007/s11356-017-8421-y

Arvidsson, J., Hillerstrom, O., 2010. Specific draught, soil fragmentation and straw incorporation for different tine and share types. Soil Tillage and Research, 110, 154–160. https://doi.org/10.1016/j.still.2010.07.003

ASABE Standards, 2015. American Society of Agricultural and Biological Engineers, ASABE Standard S526.4: Soil and Water Terminology. St. Joseph, MI..

ASTM standard, 2019. D8121/D8121M Standard test method for approximating the shear strength of cohesive soils by the handheld vane shear device. ASTM international, West Conshohocken, PA. https://doi.org/10.1520/D8121_D8121M-18

Bahrami, M., Naderi, B. M., Ghanbarian, D., Ucgul, M., Keller, T., 2020. Simulation of plate sinkage in soil using discrete element modelling: Calibration of model parameters and experimental validation. Soil Tillage and Research, 203, e104700. https://doi.org/10.1016/j.still.2020.104700

Campbell, G., S., 1985. Soil physics with basic transport models for soil-plant systems. Elsevier.

Chen, Y., Tessier, S., 1997. Techniques to diagnose plow and disk pans. Canadian Agricultural Engineering, 39, 143-148.

Hang, C., Gao, X., Yuan, M., Huang, Y., Zhu, R., 2018. Discrete element simulations and experiments of soil disturbance as affected by the tine spacing of subsoiler. Biosystems Engineering, 168, 73–82. https://doi.org/10.1016/j.biosystemseng.2017.03.008

Huang, C., Huang, Y., Zhu, R., 2017. Analysis of the movement behaviour of soil between subsoilers based on the discrete element method. Journal of Terramechanics, 74, 35–43. https://doi.org/10.1016/j.jterra.2017.10.002

Khosravi, A., Martinez, A., DeJong, J., 2020. Discrete element model (DEM) simulations of cone penetration test (CPT) measurements and soil classification. Canadian Geotechnical Journal, 57, 1369–1387. https://doi.org/10.1139/cgj-2019-0512

Kozicki, J., Tejchman, J., Mühlhaus, H. B., 2014. Discrete simulations of a triaxial compression test for sand by DEM. International Journal for Numerical and Analytical Methods in Geomechanics, 38, 1923–1952. https://doi.org/10.1002/nag.2285

Li, B., Rui, X., Fanyi, L., Jun, C., Wenting, H., Bing, H., 2016. Determination of the draft force for different subsoiler points using discrete element method. International Journal of Agricultural and Biological Engineering, 9, 81–87. https://doi.org/10.3965/j.ijabe.20160903.2210

Li, P., Ucgul, M., Lee, S. H., Saunders, C., 2020. A new approach for the automatic measurement of the angle of repose of granular materials with maximal least square using digital image processing. Computers and Electronics in Agriculture, 172, e105356. https://doi.org/10.1016/j.compag.2020.105356

McKyes. 1985. Soil cutting and tillage. Elsevier.

Murray, S., Chen, Y., 2019. Discrete element modeling of soil displacement resulting from hoe openers. Transactions of the ASABE, 62, 253–262. https://doi.org/10.13031/trans.12932

Nagy, V., Šurda, P., Lichner, L., Kovács, A. J., Milics, G., 2018. Impact of soil compaction on water content in sandy loam soil under sunflower. Vodohospodársky Časopis, 66, 416–420. https://doi.org/10.2478/johh-2018-0036

Potyondy, D. O., Cundall, P. A., 2004. A bonded-particle model for rock. International Journal of Rock Mechanics and Mining Sciences (Oxford, England: 1997), 41, 1329–1364. https://doi.org/10.1016/j.ijrmms.2004.09.011

Stefanow, D., Piotr, A. D., 2021. Soil shear strength determination methods – State of the art." Soil Tillage and Research, 208, e104881, https://doi:10.1016/j.still.2020.104881.

Sun, J., Wang, Y., Ma, Y., Tong, J., Zhang, Z., 2018. DEM simulation of bionic subsoilers (tillage depth >40 cm) with drag reduction and lower soil disturbance characteristics. Advances in Engineering Software, 119, 30–37. https://doi.org/10.1016/j.advengsoft.2018.02.001

Tamas, K., Kovacs, A., Jori, I. J., 2016. The evaluation of the parallel bond's properties in DEM modeling of soils. Periodica Polytechnica. Mechanical Engineering - Mašinostroenie, 60, 21–31. https://doi.org/10.3311/PPme.8427

Tong, J., Jiang, X., Wang, Y., Ma, Y., Li, J., Sun, J., 2020. Tillage force and disturbance characteristics of different geometric-shaped subsoilers via DEM. Advances in Manufacturing, 8, 392–404. https://doi.org/10.1007/s40436-020-00318-x

Tracy, S. R., Black, C. R., Roberts, J. A., Mooney, S. J., 2011. Soil compaction: a review of past and present techniques for investigating effects on root growth: Effect of soil compaction on root growth. Journal of the Science of Food and Agriculture, 91, 1528–1537. https://doi.org/10.1002/jsfa.4424

Wang, X., Bo, L., Rui, X., and H, Ma., 2020. Application of DEM on the design and performance analysis of bionic subsoiler. In Engineering Applications of Discrete Element Method, Springer Singapore, 139–158. https://doi.org/10.1007/978-981-15-7977-6_8

Wang, X., Gao, P., Yue, B., Shen, H., Fu, Z., Zheng, Z., Zhu, R., Huang, Y., 2019a. Optimization of installation parameters of subsoiler' wing using the discrete element method. Computers and Electronics in Agriculture, 162, 523–530. https://doi.org/10.1016/j.compag.2019.04.044

Wang, X., Li, P., He, J., Wei, W., Huang, Y., 2021. Discrete element simulations and experiments of soil-winged subsoiler interaction. International Journal of Agricultural and Biological Engineering, 14, 50–62. https://doi.org/10.25165/j.ijabe.20211401.5447

Zeng Z., Chen, Y., Zhang, X., 2017. Modelling the interaction of a deep tillage tool with heterogeneous soil. Computers and Electronics in Agriculture, 143, 130–138. https://doi.org/10.1016/j.compag.2017.10.005

Zeng, Z., Chen, Y., 2018. Performance evaluation of fluted coulters and rippled discs for vertical tillage. Soil Tillage and Research, 183, 93–99. https://doi.org/10.1016/j.still.2018.06.003

Zeng, Z., Ma, X., Chen, Y., Qi, L., 2020. Modelling residue incorporation of selected chisel ploughing tools using the discrete element method (DEM). Soil Tillage and Research, 197, e104505. https://doi.org/10.1016/j.still.2019.104505

Zhang, Y., Sun, Y., Hao, M., Zhang, L., Liu, X., 2012. Design and experimental investigation of a bionic subsoiler with a multiplex-modality shank. Applied Mechanics and Materials, 184-185, 125–129. https://doi.org/10.4028/www.scientific.net/AMM.184-185.125

Chapter 7: General Conclusions and Recommendation

7.1. General Conclusions

This research explored soil–residue–machine interactions using discrete element method (DEM) models, supported by laboratory and field experiments. A DEM model simulating corn residue and soil dynamics under disc tillage was successfully developed and validated, achieving prediction accuracies within 20% relative error for key indicators such as residue incorporation and draft force. The study identified the optimal disc operating angles for maximizing residue incorporation while minimizing draft force, advancing understanding of disc tillage dynamics. A separate DEM model for soil–cornstalk–disc interactions revealed how soil bulk density and disc type influence stalk cutting behaviour, soil supporting forces, and micro-dynamics. Results showed that disc type had a greater impact than soil density on corn stalk behaviour, and notched disc was more efficient for cutting corn stalks under varying soil conditions. In examining subsoiler operations, layered DEM soil models representing different degrees of soil heterogeneity were developed and calibrated. These models provided valuable insights into soil particle dynamics during subsoiling, particularly highlighting that a heterogeneous soil model yielded the most accurate predictions of elevated soil area, although at the cost of increased model complexity. However, none of the models accurately captured soil surface flatness, suggesting areas for future model refinement. In addition, a DEM model of a tandem disc harrow interacting with wheat stubble was developed to simulate the effects of tillage direction and operational parameters. The model demonstrated that tillage direction significantly affected residue cover but not stubble forward displacement. Optimized operational parameters helped balance soil disturbance and soil cutting efficiency, offering practical recommendations for improving harrow performance.

Among the four chapters of study, the validated DEM models developed across these studies have advanced the mechanistic understanding of soil and crop residue dynamics under tillage, offering powerful tools for optimizing equipment design and field operations in conservation agriculture. Disturbance behaviours of soil were found to be highly sensitive to tool geometry, as well as operational parameters (particularly disc angle, tilt angle, working depth, and working speed). Second, the role of crop residue was found to significantly alter the mechanical behaviours of the soil–tool interface, and to form residue flow paths under angled disc passes. Third, layered soil structures generated distinct soil disturbance zones during subsoiling, which emphasizes the importance of considering heterogeneity of soil model in deep tillage. These insights support the development of tillage practices for crop residue management.

However, caution is required when generalizing the findings beyond the specific residue types, soil conditions, and tool geometries studied. Future research should focus on refining model realism by incorporating more detailed representations of residue variability, soil compaction layers, breakable residue structures, and cutting forces, to further enhance predictive capabilities under diverse field conditions.

7.2. Recommendations

The DEM models of soil-residue-machine interactions offered valuable insights into the dynamic behaviours of soil and crop residues during tillage operations. However, the applicability of this study was constrained by the specific soil type (sandy loam soil), commercial tillage tools, and field conditions used in the experiments. Application of the research results on heavier clays or wetter conditions should be caution. The predictive capability of the DEM models may be limited by underlying assumptions, including the uniform size of spherical particles and selected

contact model. Future investigations should aim to refine model assumptions and attempt validation efforts to improve the robustness and generalizability of the results. Moreover, the computational efficiency of DEM models is currently constrained by simulation runtimes, solver settings, and potential GPU acceleration. However, as computational capacity continues to advance, DEM models are expected to be used more widely in the future.

Particularly for soil-cornstalk-disc interactions, caution should be exercised when extending the results to other crop residues, as differences in physical and mechanical properties of residue may significantly affect interaction dynamics. The corn stalk cutting orientation was controlled in both simulations and experiments, thereby requiring further investigation to understand corn stalk cutting effectiveness under random cutting orientations. For soil-subsoiler interaction model, the heterogeneous soil properties along the depth profile should be presented by more comprehensive parameters, rather than relying solely on variations in soil shear torque. In the research on disc harrow disturbance of wheat stubble, the stubble-soil connection was simplified, which presents a limitation in accurately predicting wheat stubble displacement.

Future research is needed to provide additional information to help designers and operators of tillage equipment for optimizing equipment settings. For instance, designers may want to know the percentage of burial at specific disc angles or/and working speeds under various field conditions. To evaluate energy requirements, designers may need to consider the relationship between disc geometry and operational parameters and draft force and total implement power demand. Designers should consider factors such as working width, effective tillage depth, and optimal working speed for obtaining the proper field capacity.